THE HONG KONG POLYTECHNIC UNIVERSITY
DEPARTMENT OF MECHANICAL ENGINEERING

COMPUTATIONAL AEROACOUSTICS USING LATTICE BOLTZMANN MODEL

by

LI Xue-min

A thesis submitted in partial fulfillment of the requirements for
the Degree of Doctor of Philosophy

JUNE 2006

CERTIFICATE OF ORIGINALITY

I hereby declare that this thesis is my own work and that, to the best of my knowledge and belief, it reproduces no material previously published or written, nor material that has been accepted for the award of the award of any other degree or diploma, except where due acknowledgement has been made in the text.

____________________ (Signed)

LI Xue-min (Name of student)

ABSTRACT

Computational Aeroacoustics (CAA) has been developed for noise predictions, sound-flow interactions and noise control methodologies for some years. There is a major difficulty in any CAA; that of resolving correctly the aerodynamic and acoustic scales which differ by three to four orders of magnitudes. A frequently used method is to separate the calculation of the aerodynamics and acoustics field and to carry out the simulation sequentially, thus giving rise to the well known two-step method. In this method, the unsteady flow field can be determined first using any conventional and established flow simulation schemes, such as direct numerical simulation (DNS) or large eddy simulation (LES). Once the aerodynamic field is known, the sound in the far field can be analyzed using the acoustic analogy or the vortex sound theory. In other words, the two-step method solves the Navier-Stokes equation, and a given wave equation with a specified sound speed. Therefore, if the noise source generation mechanism is not of primary interest, the two-step method is most appropriate.

If the noise source generation mechanism and the far field noise are to be determined, the acoustic disturbances in the whole field need to be deduced simultaneously with the aerodynamic field. This means that both the aerodynamic and acoustic fields have to be calculated simultaneously. This approach for CAA is either called the direct noise calculation (DNC) or the one-step method for CAA and is able to yield the aerodynamic and acoustic field as well as the sound propagation speed directly. In view of scale disparity (the aerodynamic disturbances are 10^3 to 10^4 times larger than acoustic fluctuations); the one-step method has to be highly accurate so that both aerodynamic and acoustic disturbances can be resolved

accurately. Present research on one-step method indicates that a low-dispersion and low-dissipation scheme with high-order filters and high-order non-reflecting boundary conditions is required. Such a code is very complicated because of the complex non-linear unsteady compressible Navier-Stokes equations that need to be solved. Parallel computation could not be fully made used of; therefore, computational time becomes an important issue in any one-step method for CAA.

This thesis proposes an alternative to conventional one-step methods and attempts to solve an improved Boltzmann equation (BE) rather than the non-linear Navier-Stokes equations. This method offers the following advantage over DNS or LES methods. Since the improved BE is linear, the computational code has a very simple structure. An effective numerical simulation of the improved BE is the lattice Boltzmann method (LBM), where the continuous velocity space is discretized and the particles are allowed to move with specific speeds. Conventional LBM has been developed mostly for incompressible and very low Mach number flows and is limited to mono-atomic gases. If the LBM were to be applicable to aeroacoustics simulation, it should recover the specific heat ratio and gas properties correctly for diatomic gases. Recent LBM simulations of compressible flows still invoke the mono-atomic gas model; hence the calculated specific heat ratio differs from 1.4 for diatomic gas and the Sutherland law and Fourier law of heat conduction are not recovered correctly. In other words, the calculated Reynolds and Prandtl numbers would be different from the specified values. Therefore, these methods could not be used to simulate aeroacoustic problems for air.

If the LBM is to be adopted for one-step aeroacoustic simulation of low Mach number incompressible flows, the first task is to recover the specific heat ratio and the Sutherland law correctly, thus giving rise to a correct Reynolds number. This is accomplished by modifying the BGK model for the collision term in the BE by deriving an effective collision time that takes into account the role played by translational and rotational energy of the atoms. The resultant equation is linear on the left hand side and can be solved using a 6th-order compact finite difference method to evaluate the streaming term and a second order Runge-Kutta time scheme to deal with the time dependent term on the left hand side of the improved BE. This method of solving the improved BE proves to be quite successful in resolving the aerodynamic and acoustic scales accurately. Furthermore, implementation of the non-reflecting boundary conditions on the computational boundary is relatively simple compared with the DNS scheme. A fourth- to sixth-order accurate scheme is required for the boundary in a DNS solution while a first-order accurate boundary scheme in the improved LBM is sufficient to give the same accuracy as the DNS solutions.

The improved LBM is tested against many classical problems of aeroacoustic propagation in stationary and moving medium. These include developing acoustic, vortical and entropy pulses, speed of sound recovery and sound scattering by a vortex. All improved LBM solutions are validated against DNS results and available theoretical predictions. The comparisons show that the one-step LBM scheme can be used to accurately resolve the attempted aeroacoustic problems.

The advantage of this one-step CAA method is that the code is only about 400 lines for all cases tested, where as if the Navier-Stokes equations are solved using DNS a code with 1400 lines are not unusual. Also, the simple structure of the LBM is most suitable for parallel computation, which means a significant reduction in computational time. The other advantage of this one-step CAA method is that a very simple form of boundary condition could be developed for CAA problems. The next step is to require the improved BE to recover the Prandtl number correctly. Once that is accomplished, the improved LBM could be extended to calculate compressible flows with shocks.

PUBLICATIONS ARISING FROM THE THESIS

Journals

Li X.M., Leung R.C.K. and So R.M.C., 2006, "One-Step Aeroacoustics Simulation Using Lattice Boltzmann Method," *AIAA Journal*, **44**, No. 1, 78-89.

Leung R.C.K., Li X.M. and So R.M.C., 2006, "Comparative Study of Non-Reflecting Boundary Condition for One-Step Numerical Simulation of Duct Aero-Acoustics," *AIAA Journal*, **44**, No. 3, 664-667.

Li X.M., So R.M.C. and Leung R.C.K., 2006, "Propagation Speed, Internal Energy and Direct Aeroacoustics Simulation Using LBM," *AIAA Journal*, **44**, No. 12, 2896-2903.

Leung R.C.K., So R.M.C., Wang M. H. and Li X.M., 2007, "In-Duct Orifice and Its Effect on Sound Absorption," *Journal of Sound and Vibration*, **299**, 990-1004.

Conferences

Li X.M. Leung R.C.K. and So R.M.C., 2004, "Non-Reflecting Boundary Condition for Direct Aeroacoustic Computation," *21st International Congress of Theoretical and Applied Mechanics*, Warsaw.

Li X.M. So R.M.C. and Leung R.C.K., 2005, "A Lattice Boltzmann Model for One-Step Aeroacoustics Simulation," *Second International Conference for Mesoscopic Methods in Engineering and Science*, Hong Kong.

Leung R.C.K., So R.M.C. and Li X.M., 2005, “Aeroacoustics of Two Open Cavities in Tandem Configuration,” *Twelfth International Congress on Sound and Vibration*, Lisbon.

Leung R.C.K, Wang M.H., Li X.M. and So R.M.C., 2005, “Sound Absorption by In-Duct Orifice,” *11th AIAA/CEAS Aeroacoustics Confernece (26th AIAA Aeroacoustics Conference)*, Montary, CA, USA.

Leung R.C.K, So R.M.C. Kam E.W.S. and Li X.M., 2006, “An Attempt to Calculate Acoustic Directivity Using LBM,” *12th AIAA/CEAS Aeroacoustics Conference (27th AIAA Aeroacoustics Conference)*, Cambridge, MA, USA.

ACKNOWLEDGEMENTS

I am glad to announce that I have completed my Ph.D. program here, and sincerely appreciate those who helped me in my academic life. First of all, I would like to thank my thesis supervisor, Professor Ronald M. C. So, for his academic advice. He encouraged me on my research and provided me with many academic opportunities to succeed in my career. Second, I wound like to thank Dr. Randolph Chi Kin Leung, who gave me very valuable advice at key points. Further more, I would like to thank Ms Elizabeth Wing Sze Kam for the helpful discussion on the particle collision theory and the program for computations.

I am grateful to the financial support of Hong Kong Polytechnic University and the Research Grants Council of Hong Kong under grant No. B-Q618.

Finally, I wish to thank my parents and my brother for their support and continuous encouragement.

CONTENTS

LIST OF TABLES

LIST OF FIGURES

1 Introduction

Aeroacoustics are concerned with sound generated by unsteady aerodynamic flows including turbulence and moving aerodynamic surfaces, rather than by externally applied forces or motions of classical acoustics. Noise problems due to high-speed jets, unsteady cavity flow or whistler-nozzle tone are aeroacoustics, while the acoustics due to vibrating drums or strings would fall into the category of classical acoustics. People are becoming more and more concern about their life qualities, noise complaints become more and more frequent especially in urban areas; some of the complaints are related to noise associated with airplanes at take-off and during the landing, jet flows and fan systems in factories, natural gas and water ducts in homes and commercial facilities. Sometimes the sound-structure interaction can cause self-sustained vibrations and thus threaten the safety of the systems/facilities and human lives. Self-sustained aeroacoustic pulsations were found (Bruggeman et al. 1991) in gas transport systems with closed side branches. Research on aeroacoustics can be used to explore the noise generation mechanism inside sound sources, to develop new noise abatement strategy, and also to benefit the safety of the structures with aeroacoustics.

In the study of aeroacoustics, both the unsteady aerodynamic flows and the noise radiation need to be predicted correctly if aeroacoustic problems are to be solved properly. It is different from classical acoustics problems where only the noise fields are highlighted. The need to calculate both the aerodynamic field and the acoustic field simultaneously constitutes one of the major difficulties in aeroacoustic research. The difficulty stems from the difference in scales encountered in the aerodynamic field and the acoustics field. Typically unsteady aerodynamics would produce significant near-field pressure disturbances due to the vortical, eddying motions of the unsteady flows. On the other hand, even for loud noises, such as those generated by early turbo-jets with a noise level of 114dB, the pressure fluctuations for the noise field is four orders of magnitude (10^{-4}) less than the ambient pressure (Hall 1987). Therefore, the radiated noise is far smaller than the near-field pressure fluctuations. Predicting these very small acoustic disturbances in the midst of relatively very large unsteady flows becomes a very challenging problem for researchers working in the area of aeroacoustics (Hirschberg and Schram 2002).

According to the classification by Colonius and Lele (2004), if the basic state of the flow is linear, aeroacoustic problems can be classified as linear and nonlinear on the basis of the physical processes involved in the problems. Linear problems mean that the acoustic fluctuations tend to be small so that there are minimal distortions and the amplitude decreases when the disturbances transmit through the domain examined. Typical linear acoustic problems include the classical boundary value problems of linear acoustics, sound propagation with reflecting walls, barriers, absorbing material, duct acoustics and scattering of sound in a prescribed non-uniform medium (Colonius and Lele 2004).

Noise generation in flowing medium is derived mainly from pressure fluctuations which occur in unsteady flows in order to balance momentum fluctuations. These pressure fluctuations will propagate outward from the sources and will be recognized as sound (Goldstein 1976). However, not all pressure disturbances are sinusoidally shaped waves and periodic (Pierce 1989). Most aeroacoustic noise sources are nonlinear in nature. Some examples are noise radiated from boundary layers (transition, turbulence, separation and mixing), noise from turbulent jet flows, noise from discontinuities inside tubes, fan noise and blading noise. The nonlinear noise sources will give rise to nonlinear wave propagations, nonlinear steepening and decay, focusing, nonlinear viscous effects, etc. In an environment with real fluid, viscous effect readily dissipates high-frequency components of a steepened wave, consequently, all that remain are the harmonic components of the disturbance field. Therefore, the sound field in the near field of a turbulent jet is nonlinear because the disturbances do not behave harmonically; however, the far-field noise is linear because of viscous dissipation. Consequently, the classical acoustic theory can be used to analyze the noise in the far field (Wells and Renaut 1997).

For aeroacoustic problems, the noise sources and the near-field acoustic disturbances are essentially nonlinear; therefore, classical acoustic theory cannot be used to analyze this class of problems. Furthermore, theoretical solutions can seldom be found for this class of nonlinear aeroacoustic problems and experimental techniques could rarely be used to identify the very small fluctuations inside large-scale aerodynamic flows (Hassall and Zaveri 1979). As a result, if understanding of these nonlinear aeroacoustic problems were to be obtained, computational methods are frequently employed (Colonius and Lele 2004). Computational aeroacoustics (CAA) becomes an important tool for researchers and has been developed for noise prediction, for the evaluation of sound-flow interactions and for noise control methodologies for some years (Wells and Renaut 2004). Since both the acoustic fluctuations and the aerodynamic flows need to be evaluated correctly for CAA problems, one of the major difficulties encountered is the simultaneous solution of the aerodynamic and acoustic fields (Hirschberg and Schram 2002). In most unsteady flows, the aerodynamic flow field has mean flow quantities and fluctuations that are 10^3 to 10^4 times larger than their acoustic counterparts. In other words, if the mean flow field is normalized to order 1, the acoustic disturbance field will be of order 10^{-4} to 10^{-3} (Goldstean 1976). Therefore, any solution technique used should be able to resolve scales that are 3 to 4 orders of magnitude apart. Most conventional computational fluid dynamics (CFD) methods can resolve the unsteady flow field correctly (Chung 2002); however, they could not compute the acoustic field with an acceptable accuracy. To overcome this difficulty in CAA, two kinds of methods, namely the hybrid method and the direct noise calculation method, are frequently used. Previous and recent work on these two methods is briefly reviewed below.

1.1 Hybrid Method for Noise Prediction

The hybrid method is essentially a two-step method whereby the aerodynamic solution is obtained first and the solution is used to determine the noise in the far field (Colonius & Lele 1993). This means that details of noise source generation and propagation are lost. In the first step, the unsteady aerodynamic field can be determined using any conventional and established flow simulation schemes, such as finite difference scheme, direct numerical simulation (DNS) scheme, or large eddy simulation (LES) scheme. Once the aerodynamic field is known, the sound in the far field can be analyzed using the acoustic analogy (Lighthill 1952) or the vortex sound theory (Powell 1964; Howe 2002). In other words, the two-step method solves the Navier-Stokes equation and a given wave equation with a specified sound speed. Therefore, if the noise source generation mechanism is not of primary interest, the two-step method is most appropriate. Details in the solution of the aerodynamic field are available in the literature and will be described in subsequent chapters. Therefore, it will not be repeated here. A brief review of the solution of the wave equation and the associated noise is described below.

Lighthill (1952) gave the acoustic analogy to predict jet noise using this hybrid method. In brief, Lighthill (1952) devised an arrangement of the continuity and momentum equations where all terms not appearing in the linear wave operator are grouped into a double divergence of a source-like term now known as the Lighthill stress tensor. The resultant equation becomes,

$$\frac{\partial^2 \rho'}{\partial t^2} - c_0^2 \frac{\partial^2 \rho'}{\partial x_i \partial x_i} = \frac{\partial^2 T_{ij}}{\partial x_i \partial x_j} \quad , \tag{1.1}$$

where $T_{ij} = \rho u_i u_j + p_{ij} - c_0^2 \rho \delta_{ij}$ is the stress tensor, c_0 is the speed of the sound in the stagnant uniform fluid surrounding the listener. The density perturbation would therefore follow a wave operator on the left-hand side of Eq. (1.1) while all nonlinear effects are accounted for by the stress tensor T_{ij}. The right hand side of this equation can be identified as a source of sound. Lighthill's analogy therefore defined the mechanism of the sound sources inside this tensor. Sound radiation can be calculated after all the sources are properly evaluated.

Because of the appearance of the wave operator in Lighthill's equation, the solution for certain boundary conditions can be obtained by taking advantage of the properties of linear equations, in particular, Green's theorem. The integral formulation can then be written as (Hirschberg and Schram 2002),

$$\rho'(\mathbf{x},t) = \int_{-\infty}^{t}\int_{V} G_0(t,\mathbf{x} \mid \tau,\mathbf{y}) \frac{\partial^2 \rho v_i v_j}{\partial y_i \partial y_j} d\mathbf{y} d\tau \quad , \tag{1.2}$$

where the free space Green's function is given by,

$$G_0(t,\mathbf{x} \mid \tau,\mathbf{y}) = \frac{\delta(t-\tau-|\mathbf{x}-\mathbf{y}|/c_0)}{4\pi c_0^2 |\mathbf{x}-\mathbf{y}|} \quad . \tag{1.3}$$

This integral can seldom be evaluated analytically and quite often numerical methods have to be used. In addition, approximations have to be made to simplify the stress tensor which consists of contributions from the mean and disturbance fields. Furthermore, the integral is evaluated over time; this means that any turbulence contributions to the stress tensor could be smoothed out over time and hence incorrectly accounted for. As a result, certain details of the flow and acoustic disturbance fields could be lost through this time integral over the whole domain.

In practice, the unsteady flow solution used to compute the sound sources can be based on incompressible or compressible equations; either solved using finite difference methods, DNS or LES technique. The difficulty in implementing Lighthill's acoustic analogy is the determination of the stress tensor T_{ij} for unsteady flows. Therefore, it is necessary to assume that the flow (or computational) domain already includes most of the noise-source region. However, in some flow cases, even the computational outlet boundary (no matter how large in realistic computational terms) contains a strong unsteady flow, such as a developing boundary layer. Therefore, care should be taken in the specification of the boundary conditions for the aerodynamic flow. One important consideration is to ensure that most of the strong sound sources are included inside the computational domain and the outside sources are negligible (Gloerfelt et al 2003). Another important issue is that the computational outlet boundary should be nonreflecting so that all disturbance waves are not reflected back into the computational domain to affect the aerodynamic calculations (Poinsot and Lele 1992). A more detailed discussion of this latter consideration is given in Chapter 2.

Much of the effort in using this acoustic analogy comes in the form of attempts to characterize the stress tensor. Lighthill (1952) applied this analogy to the delicate problem of sound production by a free turbulent flow and found that the sound source power scales as the 8th power of the mean velocity of the jet. The scaling law was correct for clod jets. However it is not valid for hot jets. Subsequently, Lighthill's theory was improved by Ffowcs-Williams and Hawkings (1969) and this gave rise to the Ffowcs-Williams-Hawkings equation (Ffowcs-Williams and Hawkings 1969), Leung and So (2001) used this equation to study the far-field noise generation from blade-vortex resonance. Wang and Moin (2000) predicted the far-field noise of a turbulent flow over the trailing edge of a hydrofoil using an incompressible LES code to evaluate the half-plane Green's function. More recently, Gloerfelt et al. (2003) and Larsson (2004) studied the far-field noise radiations of a subsonic cavity flow using the Ffowcs-Williams-Hawkings model and aerodynamic flow results obtained from DNS simulations.

Another widely used acoustic analogy is the vortex sound method. Since vortex dynamics can also explain the lift on an airfoil, the sound sources could be expressed in the form of vorticity distribution (Powell 1964). If Lighthill's acoustic analogy is invoked, the whole unsteady flow region needs to be considered in performing the integration. On the other hand, if the vortex sound method is used, only the region where vorticity is present needs to be included in the evaluation of the integral to deduce sound radiation. The advantage of using the vortex sound method is that a smaller domain can be used so the noise prediction step can be faster. This method provides a quick assessment of the design variables on radiated noises. It should be stressed that the noise prediction is only correct if there is sufficient accuracy in the simplified flow model. Howe (2002) studied blade-vortex interactions, interactions at the trailing edge and leading edge, and resonant oscillations inside tubes using the vortex sound method. His prediction results compared favorably with experimental data. The vortex sound method is more appropriate when used to explain the sound sources in vortex-structure interaction flow, such as cavity noise, whistle-nozzle and human whistling.

However the validity of acoustic analogy theory has not been universally accepted. Lighthill's analogy rearranged the compressible Navier-Stokes equations in a way that the linear acoustic propagation was shown in the left side of the Eq.(1.1), then, he called the right hand side of Eq.(1.1) $\partial T_{ij} / \partial x_i \partial x_j$ be the noise source. Actually, if realizing the mean flow refraction, the full wave propagation operator may not have the simple form as left hand side of Eq.(1.1). It was proved by some experimental works that Lighthill's analogy was correct for clod jets but not valid for hot jets (Atvars et al 1965, Grande 1965). Lilley derived a new equation that included acoustic mean flow interaction (Tam 2002). The noise source terms are quite different from Lighthill's quadrupole source terms. Tam (2002) gave four numerical examples to show the failure of acoustic analogy. It was proved that the quadrupole noise source terms are not unique, and acoustic analogy theory may mislead the physics for the noise sources. However, whether the Lilley's source terms are more accurate for jet noise or not, has not been proved by experiments. Many jet noise problems are due to the turbulent of flows, Lighthill's formula dose not distinguish whether the flow is turbulent or not, so it can hardly to be believed that this theory can predict turbulent noise sources correctly.

For the hybrid methods, any conventional CFD programs can be used to calculate the unsteady flow field. Since most, if not all, available CFD computer codes are well developed, there is no need to develop new CFD schemes for CAA problems. Once the aerodynamic solution is available, noise in the far field can be calculated by solving the Lighthill equation. This linear wave equation can be solved assuming either the acoustic analogy or the vortex-sound theory. Both approaches presumed a known constant speed of sound in a stagnant uniform fluid

(In reality, this sound speed might need to be adjusted according to the fluid state.). Consequently, the hybrid method could only estimate the noise level due to the unsteady flow. The method cannot provide information on sound generation mechanisms and the near-field acoustic disturbance behavior. Furthermore, the hybrid method implies that the interaction between the unsteady aerodynamic flow and acoustic field cannot be properly accounted for. Only the noise generated can be predicted but sound-flow interaction could not be studied. For these interaction problems, the unsteady flow and the acoustic fluctuations should be calculated simultaneously in the same step. This direct noise computation method is discussed below.

1.2 Direct Noise Computation Using Navier-Stokes Equations

If the noise source generation mechanism and the far field noise are to be determined, the acoustic disturbances in the whole field need to be calculated simultaneously with the aerodynamic field. This means that both the aerodynamic and acoustic fields have to be calculated simultaneously so that their interaction is resolved in the same calculation. This approach for CAA is either called the direct noise calculation (DNC) or the one-step method for CAA and is able to yield the aerodynamic and acoustic field as well as the sound propagation speed directly. This one-step computation should give the unsteady aerodynamic flow, and at the same time, predict the small acoustic disturbances and their propagation, thus giving rise to noises in the far field. In view of scale disparity (the aerodynamic disturbances are 10^3 to 10^4 times larger than acoustic fluctuations); the one-step method has to be highly accurate in order that both aerodynamic and acoustic disturbances can be resolved accurately. Otherwise, the acoustic disturbances could not be distinguished from numerical errors and the whole computation is in doubt.

Present research on one-step method indicates that a low-dispersion, low-dissipation scheme is required to give highly accurate solutions for the governing equations. Most widely used CAA schemes are formulated based on finite difference methods, finite volume methods or the conservation element (CE) method. Among the more commonly used schemes are the dispersion-relation-preserving (DRP) scheme of Tam and Webb (1993), the method of minimization of group velocity error (MGV) scheme by Holberg (1992), the high-order compact differencing scheme of Lele (1992) and the Essentially Non-Oscillatory (ENO) scheme by Casper (1994). The DRP, MGV and compact schemes are centered non-dissipative schemes, a property which is desirable for liner wave propagation. In this thesis, a 6th-order compact finite difference scheme suggested by Lele (1992) is introduced in Chapter 2. This DNS scheme is used to provide the benchmark solutions to verify the results obtained by solving the Boltzmann equation using the lattice Boltzmann method to carry out a direct noise computation.

An inherent lack of numerical dissipation of this high-order finite difference scheme might result in spurious numerical oscillations and instability in nonlinear problems, especially in boundary-layer type problems. Thus, the computations could be susceptible to failure from the unrestricted growth of numerical instabilities. These difficulties originate from a variety of sources including mesh non-uniformity, approximate boundary conditions and nonlinearity. A high-order filter is needed to suppress numerical instabilities in the computations arising from these sources (Gaitonde and Visbal 1999).

In one-step aeroacoustic computation, the treatment of the boundary points is very important. Incorrect treatment could cause serious numerical errors in the computations. For example, the lack of grid points near the computational boundaries will cause the accuracy of the 6th-order compact finite difference scheme and the high-order filtering scheme to reduce as the boundary is approached. Therefore, a lower-order finite difference scheme and a lower-order filtering scheme will have to be implemented near and at the boundary. Furthermore, when a pulse is crossing the computational boundary, if the treatment of the pulse is not correct, numerical errors would arise and a spurious reflected wave would be created at the boundary. These spurious reflected waves would propagate inward towards the computational domain. For most high-order finite difference schemes (with low-dispersion and low-dissipation), numerical viscosity could not erase the errors created by the spurious waves when they are transmitted over finite grid distances away from the boundary. Since the aerodynamic flow scales are 10^3 times larger than the acoustic scales, the spurious reflected waves from the boundary could be much larger than the real sound waves in the problem under investigation. The spurious waves could propagate into the region of interest, thus contaminating the calculation and contribute to a decrease in the computational accuracy. They could even drive the whole solution to a wrong state. Therefore, correct boundary conditions play a key role in aeroacoustic computations. Much of the effort has been focused on finding proper and correct boundary conditions for CAA problems (Poinsot and Lele 1992), especially on non-reflecting boundary conditions (Colonius et al. 1993, Giles 1990, Freund 1997, Hu 1996).

An effective DNC method has been proposed and verified against a number of classical aeroacoustic problems (Lele 1992). This DNC scheme solves the complex nonlinear unsteady compressible Navier-Stokes equations using a combined a 6th-order compact finite difference scheme for spatial differencing, 4th-order Runger-Kutta scheme for time marching, and high-order filters and high-order non-reflecting boundary conditions. However, this code is very complicated and parallel computation could not be fully made used of. Therefore, computational time becomes an important issue in one-step CAA using this numerical method. In view of this, an alternative approach is proposed whereby a linear equation is solved instead of the Navier-Stokes equation. This proposed method is based on the Boltzmann equation. A brief discussion on previous work related to the Boltzmann equation and its application to aeroacoustic computation is given below.

1.3 Objectives of the Present Thesis

This thesis proposes an alternative to conventional one-step methods and attempts to solve a modeled Boltzmann equation (BE) rather than the nonlinear Navier-Stokes equations. Since the BE is linear (Harris 1999, Wolf-Gladrow 2000), the computational code has a very simple structure. An effective numerical simulation of the modeled BE is the lattice Boltzmann method (LBM) where the collision function is approximated by the commonly used BGK model involving a single relaxation time (Bhatnagar et al. 1954), the continuous velocity space is discretized and the particles are allowed to move with specific speeds (Chen and Doolen 1998). The LBM has been developed mostly for incompressible flows (He and Doolen 1997, Guo 2000, Premnath and Abraham 2004) and very low Mach number flows (He and Luo 1997, Filippova and Hänel 2000, Ricot et al 2002) and is limited to mono-atomic gases. If the LBM were to be applicable to aeroacoustics simulation, it should recover the specific heat ratio and gas properties correctly for diatomic gases. Recent LBM simulations of compressible flows still invoke the mono-atomic gas model (Palmer and Rector 2000, Tsutahara et al 2002, Kang et al 2003); hence the calculated specific heat ratio differs from 1.4 for diatomic gas and the Sutherland law and Fourier law of heat conduction are not recovered correctly. In other words, the calculated Reynolds and Prandtl numbers would be different from the specified values. Therefore, the conventional LBM methods could not be used to simulate aeroacoustic problems for diatomic gases, such as air.

The present thesis proposes to tackle the problem in a systematic way. A three step approach is adopted; recovering the specific heat ratio for diatomic gas, recovering the correct first coefficient of viscosity and recovering the correct thermal conductivity. In the present study, focus is put on sound propagation in low Mach number flows. Therefore, it is most important to treat the first two concerns, i.e., recovering the specific heat ratio and the coefficient of viscosity correctly. The last concern will be tackled after the present approach has been fully validated and the present study completed. Therefore, the present thesis would concentrate on modifying conventional LBM methods so that the specific heat ratio for diatomic gases and the first coefficient of viscosity are recovered correctly. Thus, the calculated Reynolds number is ensured to be the same as the specified Reynolds number for the problem. In order to recover the specific heat ratio for diatomic gases, the rotation energy of the diatomic particles needs to be considered in the energy conservation equation. Therefore, a revised energy conservation law for diatomic particles is proposed so that the fully unsteady Navier-Stokes equations could be recovered from the modeled BE. In order to recover the viscosity coefficient correctly, a proposed approach is to modify the relaxation time using the Sutherland law as a constraint. The improved modeled BE can be used to carry out one-step aeroacoustic calculations of compressible flows in air. From this point on, the terminology improved BE is used to denote the improved modeled BE.

The improved BE is solved using a 6th-order compact finite difference method to evaluate the streaming term combined with a second order Runge-Kutta scheme for time marching. Some classical CAA problems are used to validate this one-step LBM computation. From this point on, the term improved LBM is used to designate the LBM based on the improved BE. These problems are: propagation of plane pressure pulse, propagation of circular pulse, simulations of acoustic, entropy and vortex pulses, speed of sound and sound scattering by a vortex. All these LBM solutions will be validated against DNS benchmark results and/or theoretical solutions. The structure of this code is quite simple and is about 400 lines, whereas the DNS code for the solution of the Navier-Stokes equations will involve at least 1400 lines. The simple structure of the improved LBM code is most suitable for parallel computation, which means a significant saving in computational time. The other advantage of this improved LBM is that a very simple form of boundary condition could be developed for CAA problems. The next step is to require the modeled BE to recover the Prandtl number correctly. Once that is accomplished, the improved LBM could be extended to calculate compressible flows with shocks.

1.4 Outline of the Thesis

The thesis is organized in the following manner. Chapter 2 outlines the one-step CAA solving the Navier-Stokes equations using a DNS technique, the finite-difference schemes, the time marching scheme, the boundary filters and the boundary treatment techniques. The proposed boundary techniques would be validated against some specific aeroacoustic problems in Chapter 3. Then using this proposed boundary technique, some basic aeroacoustic problems are calculated and the solutions are used to validate those obtained from the improved LBM. Chapter 4 outlines the derivation of the improved BE and the improved LBM. In this chapter, the approaches used to recover the specific heat ratio and the viscosity coefficient are discussed and a one-step CAA method based on the improved LBM is proposed.

Some basic aeroacoustic problems are calculated using this improved LBM in Chapter 5 and the results are validated against previously obtained DNS solutions (in Chapter 3) and/or theoretical predictions. The problem of sound scattering by a vortex is calculated using the improved LBM and a modified boundary treatment in Chapter 6 where the LBM results are also verified against DNS computations. This last example is essentially used to test the ability of the improved LBM to replicate the prediction of directivity in aeroacoustic problems correctly. Chapter 7 summarizes the contributions of this thesis with recommendations for further work.

2 One-Step Computational Aeroacoustics Method Using Navier-Stokes Equations

Two basic methods for computational aeroacoustics (CAA) have been introduced in Chapter 1; namely a two-step method and a one-step method. For two-step methods, there is an unsteady flow prediction step and a noise radiation step. The aerodynamic flow state is used to estimate the noise sources for noise prediction using either Lighthill's acoustic analogy (Lighthill 1952, Ffowcs-Williams and Hawkings 1969) or vortex sound theory (Davies 1988, Howe 1999, Freund 2000, Agarwal et al. 2004). The unsteady flow and acoustic fields are not evaluated simultaneously so the interaction between the noise and the flow could not be explored, hence the noise source generation mechanism. Using direct noise computation (DNC) method, better known as the one-step method, both the far-field sound and the near-field aerodynamics are evaluated in the same calculation step. This way, the method takes into account the direct interaction between the noise and aerodynamic fields, thus it is able to yield important information on the noise source generation mechanism.

In view of the large difference in scales between the aerodynamic and acoustic fluctuations, the solutions should be highly accurate to fully reveal the acoustic fluctuations within the aerodynamic solutions. Since DNC methods could yield noise predictions in one step and the results are likely to give near-field information on noise source as well as far-field noise compared to two-step methods, an effective DNC method using Navier-Stokes equations would be first discussed in detail in this chapter. This method is then used as a benchmark to gage the success of a proposed one-step method based on the solution of the Boltzmann equation making use of the lattice Boltzmann method. This latter one-step method is the main objective of the present thesis. Altogether, there are four sections in this chapter; they are: (1) the governing Navier-Stokes equations; (2) a 6th-order compact finite difference scheme; (3) a 4th-order Runge-Kutta method and filters; and (4) boundary treatment schemes for open as well as solid boundaries. In presenting the DNS scheme, its ability to accurately resolve the disparity in scales is pointed out. These sections are described in detail below.

2.1 Governing Equations

The governing equations for the DNC method proposed in this thesis are the two-dimensional (2D) fully unsteady compressible Navier-Stokes equations and they are cast in a strong conservation form. The vector form of the equations in Cartesian coordinates (*x, y*) can be written in a compact form as

$$\frac{\partial \boldsymbol{Q}}{\partial t}+\frac{\partial \boldsymbol{E}}{\partial x}+\frac{\partial \boldsymbol{F}}{\partial y}=\frac{\partial \boldsymbol{E}_v}{\partial x}+\frac{\partial \boldsymbol{F}_v}{\partial y} \quad , \tag{2.1}$$

where Q denotes the conservative variable matrix $\boldsymbol{Q}=\left[\rho,\ \rho u,\ \rho v,\ E_t\right]^T$, and $E_t = p/(\gamma-1)+\rho(u^2+v^2)/2$. The equation of state for a perfect gas is

$$p=\rho RT \quad , \tag{2.2}$$

where *R* is the Universal gas constant. Equations (2.1) and (2.2) as given are dimensional; however, they will be made dimensionless by normalizing with appropriate characteristic length, velocity and time scales when solved numerically. The inviscid flux vectors and the viscous flux derivative terms are represented by

$$\boldsymbol{E}=\left[\rho u,\ \rho u^2+p,\ \rho uv,\ (E_t+p)u\right]^T \quad , \tag{2.3a}$$

$$\boldsymbol{F}=\left[\rho v,\ \rho uv,\ \rho v^2+p,\ (E_t+p)v\right]^T \quad , \tag{2.3b}$$

$$\boldsymbol{E}_v = \left[0, \ \tau_{xx}, \ \tau_{xy}, \ u\tau_{xx} + v\tau_{xy} + q_x \right]^T \quad , \tag{2.3c}$$

$$\boldsymbol{F}_v = \left[0, \quad \tau_{xy}, \quad \tau_{yy}, \quad u\tau_{xy} + v\tau_{xy} + q_y \right]^T \quad , \tag{2.3d}$$

where the stress tensor components and the heat fluxes are given as

$$\tau_{xx} = \frac{2}{3}\mu\left(2\frac{\partial u}{\partial x} - \frac{\partial v}{\partial y}\right), \tau_{xy} = \mu\left(\frac{\partial u}{\partial y} + \frac{\partial v}{\partial x}\right), \tau_{yy} = \frac{2}{3}\mu\left(2\frac{\partial v}{\partial y} - \frac{\partial u}{\partial x}\right) \quad , \tag{2.4a}$$

$$q_x = k\frac{\partial T}{\partial x}, q_y = k\frac{\partial T}{\partial y} \quad . \tag{2.4b}$$

The first coefficient of viscosity μ can be related to the fluid temperature by Sutherland law, i.e.,

$$\frac{\mu}{\mu_0} = \left(\frac{T}{T_0}\right)^{3/2} \frac{T_0 + S}{T + S} \quad , \tag{2.5}$$

where μ_0 and T_0 are reference values and S is an effective temperature called Sutherland constant. The coefficient of thermal conductivity could be evaluated from the definition of the Prandtl number, Pr

$$\mathrm{Pr} = \frac{\mu C_p}{k} \Rightarrow k = \frac{\mu C_p}{\mathrm{Pr}} \Rightarrow k = \frac{\mu\gamma R}{\mathrm{Pr}(\gamma - 1)} \quad , \tag{2.6}$$

where C_p is the specific heat at constant pressure and can be evaluated from $\gamma = C_p / C_v$ and $C_p - C_v = R$, and γ is the specific heat ratio. For air, Pr = 0.71 which can be substituted into Eq. (2.6) to give an equation for *k*.

These governing equations for the fluid can be normalized using appropriately defined characteristic length, time and velocity scales. For the acoustics problem under investigation, let the characteristic scales be defined as the characteristic length L*, the characteristic speed of the flow u*, the mean temperature T*, and the mean density ρ*. Thus defined, the dimensionless parameters can be written as

$$x = x'L^*, t = t'L^*/u^*, u = u'u^*, T = T'T^*, \rho = \rho'\rho^*, p = p'\rho^* u^{*2} \quad ,$$

where the “prime” is used to denote the dimensionless values. After normalization, Eq. (2.1) can be written as

$$\frac{\partial \boldsymbol{Q}'}{\partial t'}+\frac{\partial \boldsymbol{E}'}{\partial x'}+\frac{\partial \boldsymbol{F}'}{\partial y'}=\frac{1}{\mathrm{Re}}\left(\frac{\partial \boldsymbol{E}_v'}{\partial x'}+\frac{\partial \boldsymbol{F}_v'}{\partial y'}\right) \quad ,$$

where $\boldsymbol{Q}'$ denotes the non-dimensional conservative variable vector, and $\mathrm{Re}=\rho^* u^* L^* / \mu^*$ is the Reynolds number of the flow under investigation. All definitions for the inviscid fluxes, viscous fluxes, stress tensors and the heat fluxes have the same forms as their dimensional counterparts; however, the dimensional quantities are replaced by their non-dimensional ones. In order to simplify the writing of the dimensionless Navier-Stokes equations in the following chapters, the “prime” will be dropped from all non-dimensional quantities from this point on and Eq. (2.1) will become

$$\frac{\partial \boldsymbol{Q}}{\partial t}+\frac{\partial \boldsymbol{E}}{\partial x}+\frac{\partial \boldsymbol{F}}{\partial y}=\frac{1}{\mathrm{Re}}\left(\frac{\partial \boldsymbol{E}_v}{\partial x}+\frac{\partial \boldsymbol{F}_v}{\partial y}\right) \quad . \tag{2.7}$$

The gas equation of state becomes $p=\left(RT^* / u^{*2}\right)\rho T$. If a Mach number $M=u^* / c^* = u^* / \sqrt{\gamma R T^*}$ is defined, where c^* is the dimensional speed of sound for the gas with temperature T^*, then the state equation can be reduced to

$$p=\frac{1}{\gamma M^2}\rho T \quad .$$

The non-dimensional viscosity can be reduced to $\mu = T^{3/2}\dfrac{1+S/T^*}{T+S/T^*}$ and it follows that the dimensionless k is given by $k/k^* = \mu/\mu^*$. In the following computations, $S=110.4K$ and $T^*=288.2K$ are assumed.

In the course of numerical computation of flows with different boundary geometries, a body-fitted grid or grid stretching is quite often used. Therefore, coordinate transformation is needed to bridge the coordinate system in the physical domain to that in the computational domain. Since the grid in the physical domain is by necessity non-uniform and a uniform grid would be preferred in the computational domain, a transformation should be sought such that a non-uniform grid can be transformed into a uniform grid. The computation would be further simplified if the grid size is constant in the computational domain. The normalized equations are then solved in the computational domain using such a grid. Let the grid in the physical domain (x, y) be transformed into the computational domain (ξ, η) such that the grid size along each direction is constant and is given by $\Delta\xi = M$ and $\Delta\eta = N$. The Jacobian matrix is defined as

$$J = \begin{vmatrix} \partial\xi/\partial x & \partial\xi/\partial y \\ \partial\eta/\partial x & \partial\eta/\partial y \end{vmatrix} = \begin{vmatrix} \xi_x & \xi_y \\ \eta_x & \eta_y \end{vmatrix} \quad . \tag{2.8}$$

The corresponding Navier-Stokes equations in the transformed computational domain can be written as

$$\frac{\partial \hat{\mathbf{Q}}}{\partial t} + \frac{\partial \hat{\mathbf{E}}}{\partial \xi} + \frac{\partial \hat{\mathbf{F}}}{\partial \eta} = \frac{1}{\mathrm{Re}}\left(\frac{\partial \hat{\mathbf{E}}_v}{\partial \xi} + \frac{\partial \hat{\mathbf{F}}_v}{\partial \eta} \right) \quad , \tag{2.9}$$

where

$$\hat{\mathrm{Q}} = \frac{1}{J}\mathrm{Q} \quad , \tag{2.10a}$$

$$\hat{\mathrm{E}} = \frac{1}{J}\left(\xi_x \mathrm{E} + \xi_y \mathrm{F}\right), \ \hat{\mathrm{F}} = \frac{1}{J}\left(\eta_x \mathrm{E} + \eta_y \mathrm{F}\right) \quad , \tag{2.10b}$$

$$\hat{\mathrm{E}}_v = \frac{1}{J}\left(\xi_x \mathrm{E}_v + \xi_y \mathrm{F}_v\right), \ \hat{\mathrm{F}}_v = \frac{1}{J}\left(\eta_x \mathrm{E}_v + \eta_y \mathrm{F}_v\right) \quad . \tag{2.10c}$$

The other governing equations can be similarly transformed and the complete set of governing equations is solved in the transformed plane.

Once the governing equations are written in terms of the transformed coordinates, they can be solved numerically in the computational domain. Firstly the grids in the physical domain (x,y) are cast into the computational domain (ξ,η)

where the grid size is uniform. All the transformed functions $\xi_x, \xi_y, \eta_x, \eta_y$ and the Jacobian J are evaluated at each grid point. Then the convection terms in Eq.(2.10b, c) can be evaluated at grid point. Substituting these values into Eq.(2.9) and using an ordinary finite difference scheme on the uniform mesh, the physical solutions can be determined from $\mathrm{Q} = J\hat{\mathrm{Q}}$. Similarly, all other variables can be obtained as well.

2.2 A 6th-Order Finite Difference Scheme

The need for a highly accurate numerical method was recognized from the earliest stages in the development of CAA (Tam 1995). A simple analysis of the linearized compressible Euler equations reveals that basically three types of waves could exist in a uniform mean flow, namely acoustic, entropy and vorticity waves (Tam and Webb 1993). The acoustic waves are isotropic, low-dispersive, low-dissipative and propagate with the speed of sound. The entropy and vorticity waves are non-dispersive, non-dissipative, and highly directional. They propagate in the direction of the mean flow with essentially the same speed as the flow itself.

In most current CFD schemes, there is no guarantee that the finite difference equations could support waves with these diverse characteristics. In fact, many popular codes are dispersive, anisotropic, and even highly dissipative (Lele 1992, Bogey and Bailly 2004). Therefore, new schemes with improved accuracy have been proposed by various researchers. These schemes are usually low-dispersive and low-dissipative so they can be used to resolve the widely diverse waves encountered in CAA. In general, the spatial derivatives in the Navier-Stokes equations are replaced by some high-order finite-difference equations and the time derivatives are approximated by a lower-order finite-difference scheme. The accuracy of the scheme is usually ranked by the order where the Taylor series expansion of the original governing equations was truncated. Therefore, it is expected that a fourth-order scheme is better than a second-order one. A proven scheme was proposed by Lele (1992) where a 6th-order compact finite-difference scheme and a 4th-order time march scheme was used to solve the governing equations. In the present treatment of CAA, the Lele (1992) scheme, which is a central-difference scheme, was used to solve the governing Navier-Stokes equations. This finite-difference method is briefly described below while the 4th-order time marching scheme is discussed in the next section.

For any scalar quantity, *f*, such as a flux component or a convective flow variable, the spatial derivative f' is obtained in the transformed plane by solving the following tri-diagonal system. Suppose *f* are known at points $i \in \{1, 2, ..., n-1, n\}$, where $i \in \{3, ..., n-2\}$ are the inner points, $i = 1, 2$ and $i = n-1, n$ are the boundary points on the left side and the right side of the computational domain, respectively. For the inner points, the first derivative can be solved by

$$\frac{1}{3}f'_{i-1} + f'_i + \frac{1}{3}f'_{i+1} = \frac{1}{h}\left(-\frac{1}{36}f_{i-2} - \frac{7}{9}f_{i-1} + \frac{7}{9}f_{i+1} + \frac{1}{36}f_{i+2}\right), \quad i \in \{3,4,...,n-3,n-2\} \quad , \tag{2.11}$$

where *h* is the grid size. At the boundary points, high-order one-sided formulas are invoked. For the boundary points $i = 1$ and $i = n$, the derivatives are calculated from

$$f'_1 + 3f'_2 = \frac{1}{h}\left(-\frac{17}{6}f_1 + \frac{3}{2}f_2 + \frac{3}{2}f_3 - \frac{1}{6}f_4\right) \quad , \tag{2.12a}$$

$$3f'_{n-1} + f'_n = \frac{1}{h}\left(\frac{1}{6}f_{n-3} - \frac{3}{2}f_{n-2} - \frac{3}{2}f_{n-1} + \frac{17}{6}f_n\right) \quad . \tag{2.12b}$$

At the boundary points $i = 2$ and $i = n-1$, the derivatives are given by

$$\frac{1}{6}f'_1 + f'_2 + \frac{1}{2}f'_3 = \frac{1}{h}\left(-\frac{5}{9}f_1 - \frac{1}{2}f_2 + f_3 + \frac{1}{18}f_4\right) \quad , \tag{2.13a}$$

$$\frac{1}{2}f_{n-2}^{'}+f_{n-1}^{'}+\frac{1}{6}f_{n}^{'}=\frac{1}{h}\left(-\frac{1}{18}f_{n-3}-f_{n-2}+\frac{1}{2}f_{n-1}+\frac{5}{9}f_{n}\right) \quad . \tag{2.13b}$$

Finally, the resulting algebraic equations can be simply written as

$$\begin{bmatrix} 1 & 3 & 0 & 0 & 0 & 0 & 0 & 0 & 0 & 0 & 0 \\ 1/6 & 1 & 1/2 & 0 & 0 & 0 & 0 & 0 & 0 & 0 & 0 \\ 0 & 1/3 & 1 & 1/3 & 0 & 0 & 0 & 0 & 0 & 0 & 0 \\ 0 & 0 & \ldots & \ldots & \ldots & 0 & 0 & 0 & 0 & 0 & 0 \\ 0 & 0 & 0 & \ldots & \ldots & \ldots & 0 & 0 & 0 & 0 & 0 \\ 0 & 0 & 0 & 0 & 1/3 & 1 & 1/3 & 0 & 0 & 0 & 0 \\ 0 & 0 & 0 & 0 & 0 & \ldots & \ldots & \ldots & 0 & 0 & 0 \\ 0 & 0 & 0 & 0 & 0 & 0 & \ldots & \ldots & \ldots & 0 & 0 \\ 0 & 0 & 0 & 0 & 0 & 0 & 0 & 1/3 & 1 & 1/3 & 0 \\ 0 & 0 & 0 & 0 & 0 & 0 & 0 & 0 & 1/2 & 1 & 1/6 \\ 0 & 0 & 0 & 0 & 0 & 0 & 0 & 0 & 0 & 3 & 1 \end{bmatrix} \begin{bmatrix} f_1' \\ f_2' \\ f_3' \\ \ldots \\ \ldots \\ f_i' \\ \ldots \\ \ldots \\ f_{n-2}' \\ f_{n-1}' \\ f_n' \end{bmatrix} = \frac{1}{h} \begin{bmatrix} -\frac{17}{6}f_1+\frac{3}{2}f_2+\frac{3}{2}f_3-\frac{1}{6}f_4 \\ -\frac{5}{9}f_1-\frac{1}{2}f_2+f_3+\frac{1}{18}f_4 \\ -\frac{1}{36}f_1-\frac{7}{9}f_2+\frac{7}{9}f_4+\frac{1}{36}f_5 \\ \ldots \\ \ldots \\ -\frac{1}{36}f_{i-2}-\frac{7}{9}f_{i-1}+\frac{7}{9}f_{i+1}+\frac{1}{36}f_{i+2} \\ \ldots \\ \ldots \\ -\frac{1}{36}f_{n-4}-\frac{7}{9}f_{n-3}+\frac{7}{9}f_{n-1}+\frac{1}{36}f_n \\ -\frac{1}{18}f_{n-3}-f_{n-2}+\frac{1}{2}f_{n-1}+\frac{5}{9}f_n \\ \frac{1}{6}f_{n-3}-\frac{3}{2}f_{n-2}-\frac{3}{2}f_{n-1}+\frac{17}{6}f_n \end{bmatrix} . \tag{2.14}$$

This tri-diagonal system is solved by the Thomas algorithm or the tri-diagonal matrix algorithm (TDMA) (Ferziger and Peric 1999). It is easily programmed and, more importantly, the number of operations is proportional to n, the number of unknowns, rather than n3 of a full matrix Gaussian elimination scheme. In other words, the cost per unknown is independent of the number of unknowns, which is almost as good a scaling as one could desire. The low cost suggests that this algorithm can be employed whenever possible.

2.3 4th-Order Runge-Kutta Method and High-Order Filter

A 4th-order Runge-Kutta method is used for time matching. Rewriting the original governing equations (2.7) as:

$$\frac{\partial \mathrm{Q}}{\partial t}=R(\mathrm{Q})=\frac{1}{Re}\left(\frac{\partial \mathrm{E}_v}{\partial x}+\frac{\partial \mathrm{F}_v}{\partial y}\right)-\frac{\partial \mathrm{E}}{\partial x}-\frac{\partial \mathrm{F}}{\partial y} \quad . \tag{2.15}$$

Once Q is known at time step *n* as Q^n, $R(\mathrm{Q}^n)$ can be evaluated using a finite difference scheme such as Eq. (2.14). A few inter-step predictors are used to find the next time step solutions Q^{n+1}. The first two steps of this method assume an explicit Euler predictor and an implicit Euler corrector at $n+1/2$. This is followed by a midpoint rule predictor for the full step. These steps can be written in mathematical form as

$$\begin{aligned} Q^1 &= Q^n + \frac{\Delta t}{2} R\left(Q^n\right) \quad , \\ Q^2 &= Q^n + \frac{\Delta t}{2} R\left(Q^1\right) \quad , \\ Q^3 &= Q^n + \Delta t R\left(Q^2\right) \quad , \\ Q^{n+1} &= Q^n + \frac{\Delta t}{6}\left[R\left(Q^n\right) + 2R\left(Q^1\right) + 2R\left(Q^2\right) + R\left(Q^3\right)\right] \quad . \end{aligned} \tag{2.16}$$

From time step n to time step $n+1$, this 4th-order Runge-Kutta method only involves solution Q^n, and gives a 4th-order time advancement solution for time step $n+1$. For other high-order time advancement methods such as the normal predictor-corrector or multipoint methods, the earlier time solutions such as $n-1$ or even $n-2$ are required for high-order time schemes. The Runge-Kutta method can reduce memory cost in the computations.

Like other central-difference approaches, this 6th-order compact finite difference scheme is low-dissipative, thus it is known to be susceptible to failure from the unrestricted growth of numerical instabilities (Lele 1992). These difficulties originate from a variety of sources including mesh non-uniformity, approximate boundary conditions and nonlinearity. A filter is used to suppress numerical instabilities in the computations arising from these sources (Gaitonde and Visbal 1999). In this thesis, a 10th-order filter that requires an 11-point stencil is introduced. Suppose a computational solution is known as f, the filtered values $\hat{f}$ satisfy the following equation

$$\alpha\hat{f}_{i-1} + \hat{f}_i + \alpha\hat{f}_{i+1} = \sum_{k=0}^{5} \frac{a_k}{2}\left(f_{i+k} + f_{i-k}\right), \quad i \in \{6,7,...,n-6,n-5\} \quad , \tag{2.17}$$

where $\alpha = 0.495$ and the coefficients a_k can be evaluated from the formulas given in Table 2.1.

The relatively large stencil of high-order filters requires special formulations at several points near the boundaries. For the near boundary points $i \in \{1,...,5\}$ and correspondingly at $i \in \{n-4,...,n\}$ where it protrudes the boundary, this 10th-order interior filter requires an 11-points stencil and thus cannot be applied at these points. The values at points 1 and n are specified explicitly through the boundary conditions and are not filtered. For the point $i = 5$ and $i = n-4$, an 8th-order centered formula is used:

$$\alpha\hat{f}_{i-1} + \hat{f}_i + \alpha\hat{f}_{i+1} = \sum_{k=0}^{4} \frac{b_k}{2}\left(f_{i+k} + f_{i-k}\right), \quad i = 5 \text{ or } i = n-4 \quad , \tag{2.18}$$

where the coefficients can be determined from the formulas given in Table 2.1a.

An 8th-order centered formula for $i = 5$ and $i = n-4$ has been introduced in this thesis. If the stencil-size is reduced by applying lower-order centered formulas, the error induced by these low-order central techniques may eventually become unacceptable and adversely affect the global solution accuracy. A more general approach is to use higher-order one-sided filter formulas (The coefficients are list in Table 2.1b)

$$\alpha\hat{f}_{i-1} + \hat{f}_i + \alpha\hat{f}_{i+1} = \sum_{k=1}^{9} a_{k,i} f_k, \quad i \in \{2, 3, 4\} \quad , \tag{2.19a}$$

$$\alpha\hat{f}_{i-1} + \hat{f}_i + \alpha\hat{f}_{i+1} = \sum_{k=1}^{9} a_{k,n-i+1} f_{n-k+1}, \quad i \in \{n-3, n-2, n-1\} \quad . \tag{2.19b}$$

This choice retains the tri-diagonal form of the filter for these boundary points. Finally the algebraic equations can be written into a tri-diagonal matrix form as

$$
\begin{bmatrix}
1 & 0 & 0 & 0 & 0 & 0 & 0 & 0 & 0 & 0 & 0 & 0 & 0 & 0 & 0 \\
\alpha & 1 & \alpha & 0 & 0 & 0 & 0 & 0 & 0 & 0 & 0 & 0 & 0 & 0 & 0 \\
0 & \alpha & 1 & \alpha & 0 & 0 & 0 & 0 & 0 & 0 & 0 & 0 & 0 & 0 & 0 \\
0 & 0 & \alpha & 1 & \alpha & 0 & 0 & 0 & 0 & 0 & 0 & 0 & 0 & 0 & 0 \\
0 & 0 & 0 & \alpha & 1 & \alpha & 0 & 0 & 0 & 0 & 0 & 0 & 0 & 0 & 0 \\
0 & 0 & 0 & 0 & \ldots & \ldots & \ldots & 0 & 0 & 0 & 0 & 0 & 0 & 0 & 0 \\
0 & 0 & 0 & 0 & 0 & \ldots & \ldots & \ldots & 0 & 0 & 0 & 0 & 0 & 0 & 0 \\
0 & 0 & 0 & 0 & 0 & 0 & \alpha & 1 & \alpha & 0 & 0 & 0 & 0 & 0 & 0 \\
0 & 0 & 0 & 0 & 0 & 0 & 0 & \ldots & \ldots & \ldots & 0 & 0 & 0 & 0 & 0 \\
0 & 0 & 0 & 0 & 0 & 0 & 0 & 0 & \ldots & \ldots & \ldots & 0 & 0 & 0 & 0 \\
0 & 0 & 0 & 0 & 0 & 0 & 0 & 0 & 0 & \alpha & 1 & \alpha & 0 & 0 & 0 \\
0 & 0 & 0 & 0 & 0 & 0 & 0 & 0 & 0 & 0 & \alpha & 1 & \alpha & 0 & 0 \\
0 & 0 & 0 & 0 & 0 & 0 & 0 & 0 & 0 & 0 & 0 & \alpha & 1 & \alpha & 0 \\
0 & 0 & 0 & 0 & 0 & 0 & 0 & 0 & 0 & 0 & 0 & 0 & \alpha & 1 & \alpha \\
0 & 0 & 0 & 0 & 0 & 0 & 0 & 0 & 0 & 0 & 0 & 0 & 0 & 0 & 1
\end{bmatrix}
\begin{bmatrix}
\hat{f}_1 \\ \hat{f}_2 \\ \hat{f}_3 \\ \hat{f}_4 \\ \hat{f}_5 \\ \ldots \\ \ldots \\ \hat{f}_i \\ \ldots \\ \ldots \\ \hat{f}_{n-4} \\ \hat{f}_{n-3} \\ \hat{f}_{n-2} \\ \hat{f}_{n-1} \\ \hat{f}_n
\end{bmatrix}
=
\begin{bmatrix}
f_1 \\
\sum_{k=1}^{9} a_{k,2} f_k \\
\sum_{k=1}^{9} a_{k,3} f_k \\
\sum_{k=1}^{9} a_{k,4} f_k \\
\sum_{k=0}^{4} \frac{b_k}{2}\left(f_{5+k} + f_{5-k}\right) \\
\ldots \\
\ldots \\
\sum_{k=0}^{5} \frac{a_k}{2}\left(f_{i+k} + f_{i-k}\right) \\
\ldots \\
\ldots \\
\sum_{k=0}^{4} \frac{b_k}{2}\left(f_{n-4+k} + f_{n-4-k}\right) \\
\sum_{k=1}^{9} a_{k,4} f_{n-k+1} \\
\sum_{k=1}^{9} a_{k,3} f_{n-k+1} \\
\sum_{k=1}^{9} a_{k,2} f_{n-k+1} \\
f_n
\end{bmatrix}
. \tag{2.20}
$$

A 10th-order centered formula has been chosen for the inner points, an 8th-order centered formula for point $i = 5$ and $i = n - 4$, an 8th-order one-sided formula for $i \in \{2, 3, 4\}$ and $i \in \{n-3, n-2, n-1\}$, while the values at points 1 and n are not filtered. All coefficients in the above matrix are respected to α where α must satisfy $-0.5 < \alpha \le 0.5$ for a stable filter. Higher values of α correspond to a less dissipative filter (Gaitonde and Visbal 1999); when $\alpha = 0.5$, there is no filtering effect. In the present computations, $\alpha = 0.495$ is fixed and the solutions are filtered once after the final stage of the 4th-order Runge-Kutta scheme.

2.4 Boundary Treatment Schemes

For the above finite difference scheme and filters, the lack of grid points near computational boundaries will cause the accuracy of the 6^{th}-order compact finite difference scheme and the high-order filtering scheme to reduce as the boundary is approached. Therefore, lower-order finite difference schemes and lower-order filtering schemes will have to be implemented near and at the boundary. Furthermore, when a pulse is crossing the computational boundary, if the treatment of the pulse is not correct, numerical errors would arise and a spurious reflected wave would be created at the boundary. These spurious reflected waves would propagate inward towards the computational domain and cause disturbances that could lead to unstable numerical behavior.

For most high-order finite difference schemes (with low-dispersion and low-dissipation), numerical viscosity could not erase the errors created by the spurious waves when they are transmitted over finite grid distances away from the boundary. Since the aerodynamic flow scales are 10^3 times larger than the acoustic scales, the spurious reflected waves from the boundary could be much larger than the real sound waves in the problem under investigation. The spurious waves could propagate into the region of interest, thus contaminating the calculation and contribute to a decrease in computational accuracy. They could even drive the whole solution to a wrong state. Therefore, correct boundary treatments play a key role in aeroacoustic computations. Much of the effort has been focused on finding proper and correct boundary conditions for CAA problems (Poinsot and Lele 1992, Grinstein 1994), especially on non-reflecting boundary conditions (Rudy and Strikwerda 1980, Giles 1990, Colonius et al. 1993, Hu 1996, Freund 1997, Rowley and Colonius 2000) to treat acoustic waves.

In general, three types of non-reflecting boundary conditions are wildly used in high-order scheme simulations; these are characteristic–based boundary conditions for Navier-Stokes equations (NSCBC), absorbing boundaries (Freund

1997) and the recently developed perfectly matched layer (PML) method of Hu (1996). A brief summary of these three different treatments is given below; a more detailed review of these artificial boundary conditions can be found in Colonius and Lele (2004).

2.4.1 Characteristic-Based Boundary Conditions

The most widely used boundary conditions are the characteristic-based relations. This method was derived by Engquist and Majda (1977) and improved by Roe (1986), Thompson (1987), Giles (1990), Colonius et al. (1993), and Kim and Lee (2000). Characteristic variables can be identified from an analysis of the Euler equations. Each variable then follows its own transmission equation, which is a wave-like equation. Consequently, each variable has wave property with specific propagating speed in the flow. Therefore, once these analyses are applied to the computational boundaries, outgoing waves (propagating outwards away from the boundary) and incoming waves (propagating inward towards domain) are created. In order to achieve a non-reflecting condition for the numerical boundaries, all incoming waves are set to zero in the characteristic variable equations. As a result, there are no incoming waves generated at the boundaries. This then is the basic idea of the non-reflecting characteristic boundary conditions (Yee et al 1982, Thompson 1987).

Mathematically, the starting point is the original Euler equations. Written in the primitive variable vector form, the 2-D Euler equation can be expressed as

$$\frac{\partial \mathbf{V}}{\partial t} + \mathbf{A}\frac{\partial \mathbf{V}}{\partial x} + \mathbf{B}\frac{\partial \mathbf{V}}{\partial y} = 0 \quad , \tag{2.21a}$$

$$\mathbf{A} = \begin{bmatrix} u & \rho & 0 & 0 \\ 0 & u & 0 & 1/\rho \\ 0 & 0 & u & 0 \\ 0 & \rho c^2 & 0 & u \end{bmatrix}, \quad \mathbf{B} = \begin{bmatrix} v & 0 & \rho & 0 \\ 0 & v & 0 & 0 \\ 0 & 0 & v & 1/\rho \\ 0 & 0 & \rho c^2 & v \end{bmatrix} \quad , \tag{2.21b}$$

where $\mathrm{V} = [\rho, \quad u, \quad v, \quad p]^{\mathrm{T}}$ is the primitive variable vector. Since the idea of the characteristic relations is deriving from the incoming waves and outgoing waves (Thompson 1987, Rowley and Colonius 2000), a simple wave-like solution can be assumed so that $\mathbf{V} = \hat{\mathbf{V}} e^{i(\vec{\mathbf{K}} \cdot \mathbf{X} - \omega t)}$ where $\vec{\mathbf{K}}$ is the wave direction vector.

As an illustration, the characteristic method under a 1-D assumption will be presented first. By means of 1-D, it is assumed that the outgoing waves and incoming waves only have components that are perpendicular to the computational boundaries. In other words, these waves would incident and transmit through these boundaries in the normal direction only. Consider a 2-D rectangular computational area in Cartesian coordinate (x, y); the left and right hand side boundaries are parallel to the y-axis. The 1-D assumption only considers waves with directions parallel to the x-axis. The flow is assumed uniform along the y-direction, so the gradient of the scale quantity along the y-direction is essentially zero; i.e., $\partial \mathrm{V} / \partial y \approx 0$. It should be noted that spurious errors would be created when an outgoing pulse is incorrectly estimated on the boundary; therefore, most error contributions come from an incorrect estimate of $\partial \mathrm{V} / \partial x$ under the 1-D assumption. As a result, the Matrix A needs to be diagonalized in order to determine the characteristic variables along the x-direction.

This process implies that it is necessary to deduce the sets of left (row) eigenvectors $\mathbf{L}_i$, right (column) eigenvectors $\mathbf{R}_i$, and the eigenvalues λ_i for matrix A. This requires diagonalizing matrix A using the formula $\mathbf{P}^{-1}\mathbf{AP} = \mathbf{\Lambda}$, where the rows of P-1 are the left eigenvectors and the columns of P are the right eigenvectors, and the matrix $\mathbf{\Lambda}$ is diagonal with $\Lambda_{i,i} = \lambda_i$. Analysing the characters of the matrix A, the appendant matrix P and P-1 can be determined to be

$$\mathbf{P}=\begin{bmatrix}1 & 0 & \rho/2c & \rho/2c\\ 0 & 0 & 1/2 & -1/2\\ 0 & -1 & 0 & 0\\ 0 & 0 & \rho c/2 & \rho c/2\end{bmatrix},\ \mathbf{P}^{-1}=\begin{bmatrix}1 & 0 & 0 & -1/c^2\\ 0 & 0 & -1 & 0\\ 0 & 1 & 0 & 1/\rho c\\ 0 & -1 & 0 & 1/\rho c\end{bmatrix} \quad . \tag{2.22}$$

Four eigenvalues are obtained and they are: $\lambda_1 = u, \lambda_2 = u, \lambda_3 = u + c, \lambda_4 = u - c$.

Then Eq.(2.21) can be reduced to a characteristic wave equation through the following process

$$\mathrm{P}^{-1}\frac{\partial \mathrm{V}}{\partial t}+\mathrm{P}^{-1}\mathrm{A}\frac{\partial \mathrm{V}}{\partial x}=0 \ ,\ \Rightarrow \frac{\partial \mathrm{W}}{\partial t}+\mathrm{P}^{-1}\mathrm{AP}\frac{\partial \mathrm{W}}{\partial x}=0 \quad ,$$

$$\Rightarrow \frac{\partial \mathrm{W}}{\partial t}+\begin{bmatrix}u & 0 & 0 & 0\\ 0 & u & 0 & 0\\ 0 & 0 & u+c & 0\\ 0 & 0 & 0 & u-c\end{bmatrix}\frac{\partial \mathrm{W}}{\partial x}=0 \quad , \tag{2.23}$$

where a set of new variables are defined and if written into vector form it is given by

$$\partial \mathrm{W}=\mathrm{P}^{-1}\partial \mathrm{V}=\left[\partial\rho-\partial p/c^2, \quad -\partial v, \quad \partial u+\partial p/\rho c, \quad -\partial u+\partial p/\rho c\right]^T \quad . \tag{2.24}$$

The variables inside the square bracket are called the characteristic variables. Obviously Eq. (2.23) can be separated into four independent wave-like equations

$$\partial w_i/\partial t+\lambda_i\partial w_i/\partial x=0,\ i\in\{1,\ 2,\ 3,\ 4\} \quad . \tag{2.25}$$

Each characteristic variable w_i is moving with the corresponding speed λ_i along the *x*-direction. These four characteristic variables represent four independent waves in the fluid; they are respectively the entropy wave $\partial w_1 = \partial\rho - \partial p/c^2$, the vorticity wave $\partial w_2 = -\partial v$, and two acoustic pressure waves $\partial w_3 = \partial u + \partial p/\rho c$ and $\partial w_4 = -\partial u + \partial p/\rho c$. Since independent waves are found in the flow, the incoming waves and outgoing waves could be specified by checking their propagating speeds on the numerical boundaries. If the flow is from left to right, for the right hand boundary, the waves w_1, w_2 w_3 have speeds *u*, *u* and *u*+*c*, respectively, so these waves are outgoing waves. The other wave w_4 has speed u-c < 0 (mostly a subsonic flow is assumed) and would propagate into the computational domain. If this part is set to zero, then there would have no acoustic waves propagating away from the boundary and into the computational domain. Consequently, a non-reflecting condition would exist at the boundary. If the upper and lower boundaries also need to be treated as non-reflecting, the same basic idea can be applied, but only the terms related to the *y*-direction in Eq. (2.21) need be considered. The derivation essentially follows that presented above for the *x*-direction and will not be repeated again.

The idea behind this characteristic-based boundary treatment is simple and only the boundary points need to be re-calculated in the computational method, this would have very little cost implication on the boundary treatment computations. The method has been widely used for CAA problems, e.g. Rudy and Strikwerda (1980), Yee et al (1982), Grinstein (1994), Mu and Mahalingam (1996), Stanley and Sarkar (1997), and Lockard and Morris (1998). Since the characteristic-based boundary conditions are derived from the Euler equations, all viscous terms are neglected. As a result, computations in the presence of a strong shear flow might not be stable. Poinsot and Lele (1992) attempted to improve the stability by considering the characteristic-based boundary conditions derived from the Navier-Stokes equations (NSCBC) with a local one-dimensional inviscid (LODI) assumption. The result was not too encouraging because the computation was still not stable enough in the presence of strong shear flows. Damping (Colonius et al. 1993) and grid stretching (Visbal and Gaitonde 2001) techniques were used to absorb the strong nonlinear fluctuations before they approached the boundaries. This technique was further extended by Kim and Lee (2000) to a general coordinate system. However, this kind of 1-D characteristic boundary condition works well only if the waves are incident normally on a boundary. Even though the 1-D characteristic boundary condition was used widely, the inherent weakness limits its accuracy for common use (Hixon and Mankbadi 1995, Hixon 2004).

Under the 1-D assumption, the incident waves are assumed to be perpendicular to the boundary. This condition is not exactly correct if the incident waves approach the boundary at an angle. The error will then become dependent on the deviation of the incident angle away from π/2. If wave direction is known, a more general formulation can be found to analyze the outgoing and incoming waves. Assuming that the wave vector is given by $\vec{\mathbf{K}} = (k_x, k_y)$, a general appendant matrix P and P-1 can be found. The resulting characteristic equations can be expressed as

$$\frac{\partial \mathbf{W}}{\partial t} + \begin{bmatrix} u & 0 & 0 & 0 \\ 0 & u & \frac{c}{2}k_y & \frac{c}{2}k_y \\ 0 & ck_y & u + ck_x & 0 \\ 0 & ck_y & 0 & u - ck_x \end{bmatrix} \frac{\partial \mathbf{W}}{\partial x} + \begin{bmatrix} v & 0 & 0 & 0 \\ 0 & v & -\frac{c}{2}k_x & -\frac{c}{2}k_x \\ 0 & -ck_x & v + ck_y & 0 \\ 0 & -ck_x & 0 & v - ck_y \end{bmatrix} \frac{\partial \mathbf{W}}{\partial y} = 0 \tag{2.26}$$

These equations would reduce to the 1-D relations (2.23) when $k_x = 1, k_y = 0$. The 1-D characteristic-based non-reflecting boundary conditions only estimate the normal parts of the four waves (entropy, vorticity and two acoustic waves). The 2-D formulation also defines wave direction different from the normal wave direction. Therefore, theoretically, these formulas can deal with the conditions when the outgoing waves are not necessary perpendicular to the computational boundaries. In principle, the 2-D formulation should yield better non-reflecting performance compared to the 1-D formulation. However, numerical test of the 2-D formulation fails to show much improvement as anticipated.

The test is carried out assuming a simple circular Gaussian pulse in a stagnant fluid (Fig. 2.1). When this circular pulse is developing from the center of a rectangular computational region (height equal to 10 and width equal to 2.5), the wave front would cross the computational boundaries shortly after the pulse is released. The real physical wave direction can be determined, and the result is $k_x = x/\sqrt{x^2+y^2}$, $k_y = y/\sqrt{x^2+y^2}$, where (x, y) is the position of the boundary point. At a non-dimensional time T equal to 2, the solutions (pressure contours) based on a 1-D characteristic method show significant reflection from the computational boundary, but there is relatively much less reflection using the 2-D characteristic-based method. However, as the computation proceeds to larger and larger time, the wave would cross the computational boundaries with a bigger and bigger angle. When T = 3, both the 1-D and 2-D approaches give significant spurious reflecting waves from the computational boundaries.

The linear analysis of the compressible Euler equations given above reveals that these partial differential equations support three types of waves, namely entropy, vorticity and acoustic waves. Actually these three types of waves are the basic fluctuations in aeroacoustic flows (Tam and Webb 1993). The flow solutions can be viewed as linear combinations of these waves. Physically these waves may not have the same direction, so the linear wave-like solution of the Euler equations could not be defined as $\mathbf{V} = \hat{\mathbf{V}} e^{i(\vec{\mathbf{K}} \cdot \mathbf{X} - \omega t)}$, where a single wave-vector $\vec{\mathbf{K}}$ is defined for all the waves. This is the reason why even after a general wave direction is defined as in Eq. (2.26) it is not possible to separate the characteristic variables (non-diagonal terms still exist in the convection matrices). After assuming the wave direction to be parallel to the x-axis and neglecting the gradients along the y-direction, Eq. (2.26) could be reduced to Eq. (2.25). Therefore, not much improvement could be realized by formulating the boundary treatment based on a 2-D assumption. After this test, it was concluded that generalizing the treatment by including 2-D effects would not lead to improved performance for characteristic-based non-reflecting boundary treatment.

Originally the characteristic-based method is derived from the Euler equations where flow changes are due to convection only. These inviscid terms are related to the first order spatial derivatives of the primitive variables. The basic equations for the characteristic-based method are inviscid. If viscosity could not be neglected in the flow, such as a boundary-layer flow, the second order spatial derivative terms would give rise to instability behavior if characteristic-based boundary treatment is used. To stabilize shear flow computations, Colonius et al. (1993) proposed to add damping terms into the NSCBC formulation. An alternative is to use filtering and/or artificial viscosity with a buffer zone to damp out the vortical structure before it leaves the computational domain.

The damping technique could also be applied to damp out the spurious reflected waves created by incorrect estimate of the outgoing waves at the boundaries. This suggests that a buffer zone could be added to characteristic-based boundary method to provide an even better technique for non-reflecting boundary treatment. This buffer zone technique will be further discussed below.

2.4.2 Buffer Zone/Absorbing Boundary Condition

In the present study, a widely used technique adopted is the buffer zone technique. This technique was used to absorb the perturbations before they cross the computational boundaries. Ta’asan and Nark (1995) added a convective term to the linearized Euler equations and thereby force the solution to be supersonic at the border of the computational domain. Freund (1997) improved this for the Navier-Stokes equations with an exit zone. By prescribing a desired flow, the damping terms drive the solution to this desired flow. The equation in the damping region can be written as

$$\frac{\partial \mathbf{V}}{\partial t}+\mathbf{A}\frac{\partial \mathbf{V}}{\partial x}+\mathbf{B}\frac{\partial \mathbf{V}}{\partial y}+\sigma(\mathbf{V}-\mathbf{V}_T)=0 \quad , \tag{2.27}$$

where $\mathbf{V}_T=[\rho, u, v,\ p]^T$ is the target vector of the desired flow, σ is the absorption coefficient that varies smoothly from zero at the edge of the buffer to a constant value near the boundaries. With this damping function $\sigma(\mathbf{V}-\mathbf{V}_T)$, the solutions would be forced to approach the desired flow near the computational boundaries. In general, a uniform mean flow is used as the target, so most disturbances originating from the inner field would be absorbed in the damping region and minimal fluctuations would pass the computational boundaries. This way, spurious reflected waves are reduced to a minimum and the solutions at and near the computational boundaries would be very close to the target flow quantities.

Additional grids are needed outside the computational area to accommodate the buffer region. It means that additional computing time is required to solve the governing equations over the complete domain. If really effective non-reflecting boundary conditions were to be realized, large damping regions are needed. This would increase the computational cost significantly. An attractive alternative is the perfectly matched layer technique.

2.4.3 Buffer Zone/Perfectly Matched Layer (PML)

Berenger (1994) introduced a perfectly matched layer (PML) technique for solving the Maxwell equation for electromagnetic waves. The idea is similar to the absorbing boundary condition but the damping terms were introduced based on a perfectly matched method. In the physical domain, the PML equations are the same as the original equations, in the damping region, all the disturbances are absorbed and the solutions near the computational boundaries are forced to a desired solution.

For the linearized Euler equations, there are two kinds of PML formulations. The first used split physical variables in the PML domain (Ta'asan et al. 1995, Hesthaven 1998, Turkel and Yefet 1998). The second formulation was given by Hu (1996, 2001) and did not split the physical variables. Instead, Hu (1996, 2001) introduced additional terms to the linearized Euler equations. The split variables method was not as effective as the method of Hu (1996, 2001). Therefore, in the following, the PML method in a no mean flow condition (Hu 1996) is discussed first and this is followed by a discussion of an improved method where uniform mean flow is not assumed.

(i) Zero mean flow condition

Referring to the linearized Euler equation given in Eq. (2.21), the linear solution can be split into two parts, $\mathbf{V} = \mathbf{V_1} + \mathbf{V_2}$, so that $\mathbf{V_1}$ is propagating along the *x*-direction and $\mathbf{V_2}$ is propagating along the *y*-direction. The split version of the PML equations can then be written as

$$\frac{\partial \mathrm{V}_1}{\partial t} + \sigma_x \mathrm{V}_1 + \mathrm{A}\frac{\partial \mathrm{V}}{\partial x} = 0 \quad , \tag{2.28a}$$

$$\frac{\partial \mathrm{V}_2}{\partial t} + \sigma_y \mathrm{V}_2 + \mathrm{B}\frac{\partial \mathrm{V}}{\partial y} = 0 \quad , \tag{2.28b}$$

where σ_x and σ_y are positive absorption coefficients. In the frequency domain, the equations can be written as

$$-i\omega\tilde{\mathbf{V}}_\mathbf{1} + \sigma_x \tilde{\mathbf{V}}_\mathbf{1} + \mathbf{A}\frac{\partial \tilde{\mathbf{V}}}{\partial x} = 0 \quad , \tag{2.29a}$$

$$-i\omega\tilde{\mathbf{V}}_\mathbf{2} + \sigma_y \tilde{\mathbf{V}}_\mathbf{2} + \mathbf{B}\frac{\partial \tilde{\mathbf{V}}}{\partial y} = 0 \quad . \tag{2.29b}$$

These two split equations can be combined to give one non-split form as

$$-i\omega\tilde{\mathbf{V}}+(\sigma_x+\sigma_y)\tilde{\mathbf{V}}+\frac{i\sigma_x\sigma_y}{\omega}\tilde{\mathbf{V}}+(1+\frac{i\sigma_y}{\omega})\mathbf{A}\frac{\partial\tilde{\mathbf{V}}}{\partial x}+(1+\frac{i\sigma_x}{\omega})\mathbf{B}\frac{\partial\tilde{\mathbf{V}}}{\partial y}=0 \quad . \quad (2.30)$$

Introducing an auxiliary variable **q**, Eq. (2.30) can be converted back to the time domain as

$$\frac{\partial\mathbf{V}}{\partial t}+\mathbf{A}\frac{\partial\mathbf{V}}{\partial x}+\mathbf{B}\frac{\partial\mathbf{V}}{\partial y}+\sigma_y\mathbf{A}\frac{\partial\mathbf{q}}{\partial x}+\sigma_x\mathbf{B}\frac{\partial\mathbf{q}}{\partial y}+(\sigma_x+\sigma_y)\mathbf{V}+\sigma_x\sigma_y\mathbf{q}=0 \quad , \quad (2.31a)$$

$$\frac{\partial\mathbf{q}}{\partial t}=\mathbf{V} \quad . \quad (2.31b)$$

These equations are correct when there is no mean flow in the computational domain. In the presence of a mean flow, there exist acoustic waves that have positive group velocity but a negative phase velocity in the direction of the mean flow and these waves will be amplified under the previous formulation, thus giving rise to computational instability. To remedy this shortcoming, Hu (1996) gave a stable PML formulation in unsplit physical variables for the linearized Euler equations as follow

$$\frac{\partial\mathbf{V}}{\partial t}+\mathbf{A}\frac{\partial\mathbf{V}}{\partial x}+\mathbf{B}\frac{\partial\mathbf{V}}{\partial y}+\mathbf{D}=0 \quad , \quad (2.32a)$$

$$\frac{\partial\mathbf{q}}{\partial t}=\mathbf{V} \quad , \quad (2.32b)$$

where $\mathbf{D}=\sigma_y\mathbf{A}\frac{\partial\mathbf{q}}{\partial x}+\sigma_x\mathbf{B}\frac{\partial\mathbf{q}}{\partial y}+(\sigma_x+\sigma_y)\mathbf{V}+\sigma_x\sigma_y\mathbf{q}+\frac{\sigma_x M}{1\text{-}M^2}\mathbf{A}(\mathbf{V}+\sigma_y\mathbf{q})$ is the damping term.

The derivation of this damping term D is quite complicated; as a result, it is very difficult to recover the Euler equation from Eq. (2.32). A simple coordinate transformation can be used to derive a similar PML damper for the Euler equation. The results showed that the PML thus derived has the same character as that given by Hu's method. The PML method is preferable compared to the damping method for the following reasons. Firstly, the absorbing boundary conditions are constructed in a rude way to force the solutions to a prescribed form. Secondly, the damping terms in the PML are formulated to absorb the waves inside the buffer zone. Therefore, theoretically, the PML damping domain usually is more effective than the absorbing boundary conditions.

(ii) With mean flow

With a mean flow, the pressure equation will become a convective wave equation (Turkel 1998). In order to deal with a local mean flow, it is suggested that the PML formulation should be set up in a new coordinate system so that the pressure equation will be reduced to a standard wave equation. That way, the instability introduced by the local mean flow could be eliminated in the solution process and stable solutions could be achieved again. A simple idea to derive the new coordinate system is to follow the mean flow speed to study the waves.

Starting with the Euler equation in primitive variables, i.e., Eq. (2.21), the velocity perturbations (disturbances) in vector form could be written as $\mathbf{V}' = \mathbf{V} - \overline{\mathbf{V}}$. From Eq. (2.21), the perturbations are governed by the following equation

$$\left(\frac{\partial \mathbf{V}'}{\partial t} + \mathbf{A}\frac{\partial \mathbf{V}'}{\partial x} + \mathbf{B}\frac{\partial \mathbf{V}'}{\partial y}\right) + \left(\frac{\partial \overline{\mathbf{V}}}{\partial t} + \mathbf{A}\frac{\partial \overline{\mathbf{V}}}{\partial x} + \mathbf{B}\frac{\partial \overline{\mathbf{V}}}{\partial y}\right) = 0 \quad . \tag{2.33}$$

Invoking the linear assumption again and assuming the perturbations to be much less than either $\mathbf{V}$ or $\overline{\mathbf{V}}$, the first bracketed term of Eq. (2.33) is very small compared with the second bracketed term. In other words, it can be neglected as a first approximation. Eq. (2.33) is then reduced to

$$\left(\frac{\partial \overline{\mathbf{V}}}{\partial t} + \mathbf{A}\frac{\partial \overline{\mathbf{V}}}{\partial x} + \mathbf{B}\frac{\partial \overline{\mathbf{V}}}{\partial y}\right) \cong 0 \quad , \tag{2.34}$$

and the Euler equation for the perturbations, Eq. (2.33), reduces to

$$\frac{\partial \mathbf{V}'}{\partial t} + \mathbf{A}\frac{\partial \mathbf{V}'}{\partial x} + \mathbf{B}\frac{\partial \mathbf{V}'}{\partial y} \cong 0 \quad . \tag{2.35}$$

A coordinate transformation can be proposed to allow the wave to follow the mean flow speed. Such a transformation can be defined as

$$\begin{bmatrix} \xi \\ \eta \\ \tau \end{bmatrix} = \begin{bmatrix} 1 & 0 & -\bar{u} \\ 0 & 1 & -\bar{v} \\ 0 & 0 & 1 \end{bmatrix} \begin{bmatrix} x \\ y \\ t \end{bmatrix} \quad , \tag{2.36a}$$

where $\bar{u}$ and $\bar{v}$ are the mean *x*- and *y*-component of $\overline{\mathbf{V}}$. In this coordinate transformation, it should be pointed out that when the mean flow velocity is uniform and steady $\partial\bar{u}/\partial x = \partial\bar{u}/\partial y = \partial\bar{u}/\partial t = 0, \quad \partial\bar{v}/\partial x = \partial\bar{v}/\partial y = \partial\bar{v}/\partial t = 0$, the first partial derivatives in the new coordinate system (ξ,η,τ) can be derived as

$$\begin{bmatrix} \partial/\partial\xi \\ \partial/\partial\eta \\ \partial/\partial\tau \end{bmatrix} = \begin{bmatrix} 1 & 0 & 0 \\ 0 & 1 & 0 \\ \bar{u} & \bar{v} & 1 \end{bmatrix} \begin{bmatrix} \partial/\partial x \\ \partial/\partial y \\ \partial/\partial t \end{bmatrix} \quad . \tag{2.36b}$$

Therefore, in terms of the new coordinates (ξ,η,τ), Eq. (2.35) becomes

$$\frac{\partial \mathbf{V}'}{\partial \tau} + (\mathbf{A} - \bar{u}\mathbf{I})\frac{\partial \mathbf{V}'}{\partial \xi} + (\mathbf{B} - \bar{v}\mathbf{I})\frac{\partial \mathbf{V}'}{\partial \eta} = 0 \quad . \tag{2.37}$$

Again, if $\mathbf{V}' = \mathbf{V}_1' + \mathbf{V}_2'$ is assumed and introducing an auxiliary variable q, equations similar to Eq. (2.31) can be deduced. In terms of the coordinates (ξ,η,τ), they are

$$\frac{\partial \mathbf{V}'}{\partial \tau} + \tilde{\mathbf{A}}\frac{\partial \mathbf{V}'}{\partial \xi} + \tilde{\mathbf{B}}\frac{\partial \mathbf{V}'}{\partial \eta} + \sigma_\eta \tilde{\mathbf{A}}\frac{\partial \mathbf{q}}{\partial \xi} + \sigma_\xi \tilde{\mathbf{B}}\frac{\partial \mathbf{q}}{\partial \eta} + (\sigma_\xi + \sigma_\eta)\mathbf{V}' + \sigma_\xi\sigma_\eta\mathbf{q} = 0 , \tag{2.38a}$$

$$\frac{\partial \mathbf{q}}{\partial \tau} = \mathbf{V}' \quad , \tag{2.38b}$$

where $\tilde{\mathbf{A}} = (\mathbf{A} - \bar{u}\mathbf{I}),\ \tilde{\mathbf{B}} = (\mathbf{B} - \bar{v}\mathbf{I})$. Transforming back to the original coordinates (x,y,t), Eq. (2.38) can be written as

$$\frac{\partial \mathbf{V}'}{\partial t}+\mathbf{A}\frac{\partial \mathbf{V}'}{\partial x}+\mathbf{B}\frac{\partial \mathbf{V}'}{\partial y}+\sigma_\eta \mathbf{A}\frac{\partial \mathbf{q}}{\partial x}+\sigma_\xi \mathbf{B}\frac{\partial \mathbf{q}}{\partial y}+(\sigma_\xi+\sigma_\eta)\mathbf{V}'$$

$$+\sigma_\xi\sigma_\eta\mathbf{q}-\sigma_\eta\bar{u}\mathbf{I}\frac{\partial \mathbf{q}}{\partial x}-\sigma_\xi\bar{v}\mathbf{I}\frac{\partial \mathbf{q}}{\partial y}=0 \quad , \tag{2.39a}$$

$$\bar{u}\frac{\partial \mathbf{q}}{\partial x}+\bar{v}\frac{\partial \mathbf{q}}{\partial x}+\frac{\partial \mathbf{q}}{\partial t}=\mathbf{V}' \quad . \tag{2.39b}$$

It should be noted that under the linear assumption, Eq. (2.39) can be written as

$$\frac{\partial \mathbf{V}}{\partial t}+\mathbf{A}\frac{\partial \mathbf{V}}{\partial x}+\mathbf{B}\frac{\partial \mathbf{V}}{\partial y}+\sigma_\eta \mathbf{A}\frac{\partial \mathbf{q}}{\partial x}+\sigma_\xi \mathbf{B}\frac{\partial \mathbf{q}}{\partial y}+(\sigma_\xi+\sigma_\eta)\left(\mathbf{V}-\bar{\mathbf{V}}\right)$$

$$+\sigma_\xi\sigma_\eta\mathbf{q}-\sigma_\eta\bar{u}\mathbf{I}\frac{\partial \mathbf{q}}{\partial x}-\sigma_\xi\bar{v}\mathbf{I}\frac{\partial \mathbf{q}}{\partial y}=0 \quad , \tag{2.40a}$$

$$\bar{u}\frac{\partial \mathbf{q}}{\partial x}+\bar{v}\frac{\partial \mathbf{q}}{\partial x}+\frac{\partial \mathbf{q}}{\partial t}=\mathbf{V}-\bar{\mathbf{V}} \quad . \tag{2.40b}$$

There are two more damping terms in Eq. (2.40a) compared to Eq. (2.31) for the case where $\bar{\mathbf{V}}$ = 0. These two terms are $-\sigma_\eta\bar{u}\mathbf{I}\left(\partial\mathbf{q}/\partial x\right)-\sigma_\xi\bar{v}\mathbf{I}\left(\partial\mathbf{q}/\partial y\right)$. In addition, there is a convective contribution to the equation for **q**. The convective part is given by the first two terms on the left hand side of Eq. (2.40b). Together these four terms allow the modified PML to take the mean flow contribution into account in the formulation of the non-reflecting boundary conditions.

2.5 Summary

In this chapter, a one-step CAA method is introduced. The 2-D unsteady compressible Navier-Stokes equations are numerically solved using a 6th-order compact finite-difference scheme and with a 4th-order Runge-Kutta technique for time advancement. Since the scheme has low dissipation, a high-order filter is used to suppress numerical instabilities. Some special boundary treatment methods (characteristic-based method, absorbing technique and PML method) are discussed. Since most high-order schemes are time consuming, it is important to implement proper boundary treatment to reduce the computational domain and hence computational time. As a result, much work has been devoted to identify the best boundary treatment technique for CAA computations with the aim to reduce the computational time effectively for CAA. In the following chapter, a detail comparison would be given for these three types of non-reflecting boundary methods.

Table 2.1 Filter Coefficients.

a. For a_k , $i \in \{6,7,...,n-6,n-5\}$ and b_k , $i = 5$ or $i = n-4$.

	K=0	K=1	K=2	K=3	K=4	K=5
a_k	$\frac{193+126\alpha}{256}$	$\frac{105+302\alpha}{256}$	$\frac{-15+30\alpha}{64}$	$\frac{45-90\alpha}{512}$	$\frac{-5+10\alpha}{256}$	$\frac{1-2\alpha}{512}$
b_k	$\frac{93+70\alpha}{128}$	$\frac{7+18\alpha}{16}$	$\frac{-7+14\alpha}{32}$	$\frac{1-2\alpha}{16}$	$\frac{-1+2\alpha}{128}$	0

b. For $a_{k,4}$, $i = 4$ or $i = n-3$; $a_{k,3}$, $i = 3$ or $i = n-2$ and $a_{k,2}$, $i = 2$ or $i = n-1$.

	K=1	K=2	K=3	K=4	K=5	K=6	K=7	K=8	K=9
$a_{k,4}$	$\frac{1-2\alpha}{256}$	$\frac{-1+2\alpha}{32}$	$\frac{7+50\alpha}{64}$	$\frac{25+14\alpha}{32}$	$\frac{35+58\alpha}{128}$	$\frac{-7+14\alpha}{32}$	$\frac{7-14\alpha}{64}$	$\frac{-1+2\alpha}{32}$	$\frac{1-2\alpha}{256}$
$a_{k,3}$	$\frac{-1+2\alpha}{256}$	$\frac{1+30\alpha}{32}$	$\frac{57+14\alpha}{64}$	$\frac{7+18\alpha}{32}$	$\frac{-35+70\alpha}{128}$	$\frac{7-14\alpha}{32}$	$\frac{-7+14\alpha}{64}$	$\frac{1-2\alpha}{32}$	$\frac{-1+2\alpha}{256}$
$a_{k,2}$	$\frac{1+254\alpha}{256}$	$\frac{31+2\alpha}{32}$	$\frac{7+50\alpha}{64}$	$\frac{-7+14\alpha}{32}$	$\frac{35-70\alpha}{128}$	$\frac{-7+14\alpha}{32}$	$\frac{7-14\alpha}{64}$	$\frac{-1+2\alpha}{32}$	$\frac{1-2\alpha}{256}$

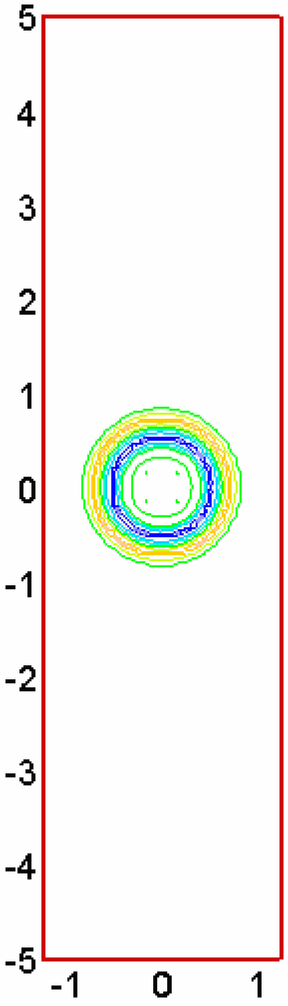

Figure 2.1 Gaussian pulse in the computational domain.

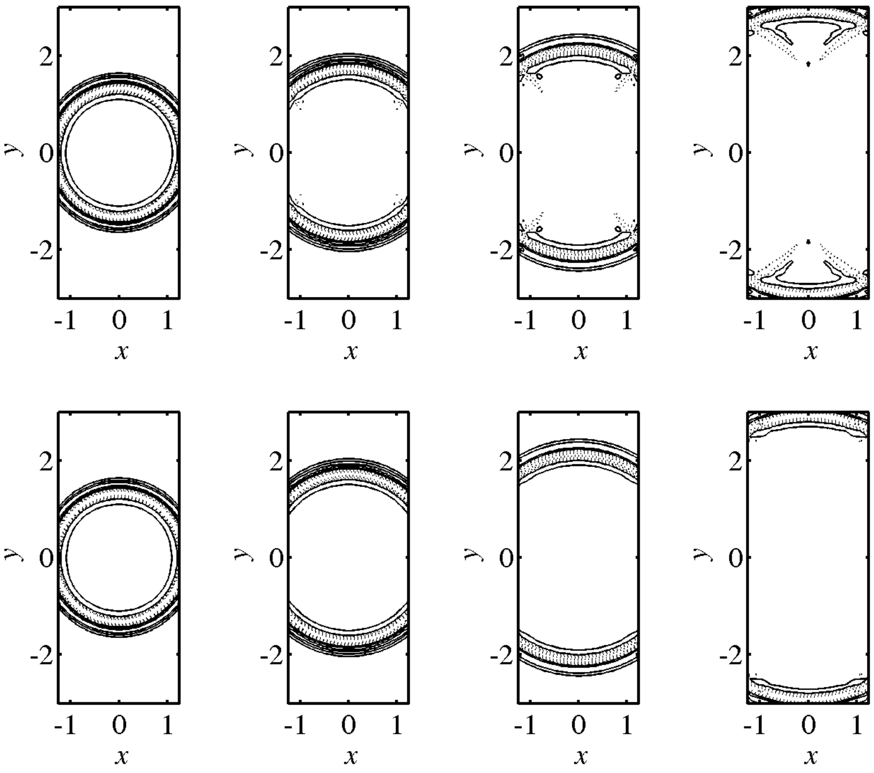

Figure 2.2 Non-reflecting boundaries with 1D NSCBC (upper) and 2D NSCBC (lower).

3 DNS Calculations of Benchmark Aeroacoustic Problems

In Chapter 2, a full description of an effective one-step CAA method based on direct numerical simulation (DNS) of the governing Navier-Stokes equations has been presented. In this chapter, the DNS scheme would be validated against some classical aeroacoustic problems. Since this scheme has been used to successfully calculate some complex aeroacoustic flows (Grinstein 1994, Freund 1997, Kim and Lee 2000, Gloerfelt et al 2003), its validation against these flow cases would not be repeated in this Chapter. Instead, the DNS scheme will be used to calculate some benchmark aeroacoustic problems in anticipation that these same cases will be used to validate the proposed lattice Boltzmann model (LBM) simulations. The purpose of this thesis is to develop a new one-step CAA scheme using LBM. The DNS calculations obtained in this Chapter could then serve as reference solutions for all LBM computations. Therefore, in the following, validation of the DNS scheme against a few classical pulse problems would be discussed.

The first part of this chapter would be used to validate the accuracy of computations and, at the same time, to seek proper boundary schemes for these open boundary problems. A propagation of entropy, acoustic and voriticity pulses in the mean flow would be calculated. There are no walls in all these computations. Even then, careful artificial boundary treatment should be applied to these boundaries, because physically there are no boundaries and all pulses should pass through the virtual boundaries freely. This means that if computational boundaries are imposed on the physical domain, they should be non-reflecting for all waves. Different boundary techniques would be test for the same problem. A larger domain computation would be used as reference. After the comparison, the proper non-reflecting boundary schemes would be found.

The proper non-reflecting boundary scheme would be used to calculate some basic acoustic pulses; those are the second part of this chapter. These are: (i), propagation of a plane pressure pulse; (ii), propagation of a circular pressure pulse; (iii), propagation of continuous plane waves; (iv), propagation speed of sound in different Mach number flow.

3.1 Propagation of Entropy, Vortex and Acoustic Pulses in a Mean Flow

The linear analysis of Euler equations shows that basically there are three kind of linear waves in the flow, these are entropy, vortex and acoustic waves. The acoustic waves have the propagation speed of sound but the entropy and vortex waves are translating with the mean flow. Proper non-reflecting boundary techniques should have the ability to let all these pulses pass freely. A propagation of entropy, vortex and acoustic pulses in the mean flow were studied to compare the boundary techniques.

The half-distance between the acoustic pulse and vortex pulse l_0 is chosen as the characteristic length. The characteristic scales for speed, time, density, pressure and temperature are defined from the mean flow quantities u_0, l_0/u_0, ρ_0, $\rho_0 u_0^2$ and T_0, respectively. The Mach number of this mean flow is $M = u_0/c_0 = 0.5$ and the Reynolds number is taken to be $Re = \rho_0 c_0 L_0 / \mu_0 = 10000$. After normalization, the center of the acoustic pulse is placed at *x* = -1, *y* = 0, the vortex pulse and the entropy center are located at *x* = 1, *y* = 0 as shown in Fig. 3.1. The initial condition for the computations can be defined as follow:

$$\rho = \rho_\infty + \rho' = 1 + \varepsilon_1 \exp\left\{-\ln 2 \times \frac{\left[(x+1)^2 + y^2\right]}{0.2^2}\right\} + \varepsilon_2 \exp\left\{-\ln 2 \times \frac{\left[(x-1)^2 + y^2\right]}{0.2^2}\right\} \tag{3.1a}$$

$$u = u_\infty + u' = 1 + \varepsilon_3 y \exp\left\{-\ln 2 \times \frac{\left[(x-1)^2 + y^2\right]}{0.2^2}\right\} \quad , \tag{3.1b}$$

$$v = v_\infty + v' = -\varepsilon_3 (x-1) \exp\left\{-\ln 2 \times \frac{\left[(x-1)^2 + y^2\right]}{0.2^2}\right\} \quad , \tag{3.1c}$$

$$p = p_\infty + p' = \frac{1}{\gamma M^2} + \frac{\varepsilon_1}{M^2} \exp\left\{-\ln 2 \times \frac{\left[(x+1)^2 + y^2\right]}{0.2^2}\right\} \quad . \tag{3.1d}$$

A uniform mesh ($\Delta x = \Delta y = 0.05$) is assumed for this case. The strength of the pulses are defined as $\varepsilon_1 = 0.0001, \varepsilon_2 = 0.001$ and $\varepsilon_3 = 0.0001$, respectively.

The physical area is bounded by $-2.5 \le x \le 2.5$ and $-2.5 \le y \le 2.5$. Four artificial boundaries are needed to close this physical area. Outside the physical area, there are no pulses and disturbances, so physically all the disturbances could only propagate to outside. Different non-reflecting boundary techniques would be used to close this area. A reference solution is obtained by carrying out the calculation using a larger computational domain. The size of the computational domain for this calculation is chosen such that the results in the smaller region are free of any disturbances. The errors are then deduced by subtracting the reference solution from the bounded solutions. The performance of the boundary techniques would be compared and the optimized boundary method would be found out. Another comparison is also made with the computing time and costs.

As shown in Table 3.1, Test 1 is based on the NSCBC method and no damping region is needed. Test 2 invokes the PML method. There are 4 damping layers with equal width of 0.5 added to the area outside of the physical domain. Test 3 uses

Freund's absorbing technique with the same damping areas as specified in Test 2. Test 4 uses Freund's absorbing layers with width equal to 2, which is 4 times that of Test 3. Finally, the reference solution is included as Test 5.

3.1.1 Damping Effect

In the NSCBC method, the instantaneous values for the boundary points ($i=1$ and $i=n$) are corrected by the characteristics analysis. It should be noted that, only the convection terms in the Naver-Stokes equations are greatly emphasized when using this linear analysis. This requires an inviscid flow condition. Fig. 3.2 shows the vorticity contours obtained using NSCBC (the dimensionless time for panels a, b, c and d are 1.2, 1.5, 1.8 and 2.1, respectively), where the dashed line is used to mark the computational outlet for Test 1. The vortex contours in Fig. 3.2a have the same shape as those in Fig. 3.2b. It shows that viscosity effect is very small in this case and the physical solution is close to an inviscid flow solution. Furthermore, it shows that the vortex can pass through the outlet (NSCBC) freely and without reflection. It should be noted that this does not mean that the NSCBC is a purely non-reflecting outlet. Actually, after the convection vortex passes through the outlet, some spurious acoustic waves come out from the artificial outlet. This would be discussed later in the accuracy comparison section.

In the other 4 tests with absorbing boundaries, damping layers are used to absorb the outgoing waves. Since most of the spurious waves are caused by the vorticity pulses, the damping effect on the vortex strength would be discussed first. Fig. 3.3 and Fig 3.4 are the vorticity contours for Test 2 and Test 3, respectively. Before the vortex touches the damping region, the vortex strength is almost the same as in the physical domain. When it enters the damping region, the vortex strength is decreased quickly by the damping effect. So the reflection caused by the vorticity pulse could be reduced. Since different damping terms are used in different methods, the PML and Freund's method give different solutions inside the damping region. The solutions inside the damping layer do not have any physical meaning. They only suggest how the vorticity pulse is absorbed step by step inside the damping layer.

The pressure contours of the physical field for all tests are plotted in Fig. 3.5 (Test 1), Fig. 3.6 (Test 2), Fig. 3.7 (Test 3) and Fig. 3.8 (Test 5). It should be noted that the irregularities in Fig. 3.5 and Fig. 3.7 are due to inappropriate boundary conditions. When the acoustic pulse passes through a boundary with NSCBC specified, there are clear reflections coming from the boundaries. This is especially true in the vicinity of the four corners where the wave fronts are close to $\pi / 4$ of the computational boundaries. In principle, the whole domain should not be bounded; however, because of the truncated computational boundary and the inaccuracy of the boundary methods some reflecting waves are created at the boundaries. The spurious reflecting waves are clearly visible in Fig. 3.5 (NSCBC) and Fig. 3.7 (Freund's absorbing technique). These results demonstrate that PML performs better than the methods of NSCBC and Freund. If damping technique is used (Test 2 and Test 3), the solutions are improved. The PML method is better than Freund's absorbing technique, but details of the accuracy comparison are discussed in the following.

3.1.2 Accuracy Comparison

Since the vorticity pulse would cause the most spurious waves on the boundaries, the solutions at the physical outlet (dashed line) are chosen for the accuracy comparisons because the vorticity pulse would pass through this line. Three kinds of errors are reported in the following comparisons.

At any instantaneous time, if any quantity (pressure, density or velocity component) for the local point i has a value f_i, and the unbounded solution has a value f_{ir}, then at this time, the mean error L_1, root-mean-square error L_2 and maximum error L_m can be defined as

$$L_1 = \sum_{i=1}^{N} \left(f_i - f_{ir} \right) \Big/ N \quad , \tag{3.2a}$$

$$L_2 = \sqrt{\sum_{i=1}^{N} \left(f_i - f_{ir} \right)^2 \Big/ N} \quad , \tag{3.2b}$$

$$L_m = \max\left(f_i - f_{ir} \right) \quad , \tag{3.2c}$$

where N = 101. In the following, the *p* and *u* errors are assessed and compared.

The pressure errors are compared in Fig. 3.9, Fig. 3.10 and Fig. 3.11 where the figures show the time-histories of L_1, L_2 and L_m, respectively. The errors of "u" histories are compared in Fig. 3.12, Fig. 3.13 and Fig. 3.14. In all these comparisons, NSCBC gives the biggest error at the physical outlet. The absorbing methods (PML or Freund's absorbing technique) could increase the non-reflecting accuracy by 2 orders higher than that of the NSCBC method. Using equal width damping layers, the PML method (Test 2) performs much better than the absorbing BC (Test 3). It means that the PML region is more efficient in absorbing disturbances than the corresponding Freund's damping region. It should be noted that, even after the Freund's damping domain size is increased by 4 times (Test 4), the error is still larger than that given by the PML with D = 0.5. In another words, the PML method could produce a solution with the same accuracy as the Freund's absorbing technique using a much smaller damping region. This will undoubtedly lead to reduced computing cost. However, the formulation of PML introduced an auxiliary variable q inside the damping region. This would cause additional computations for the spatial derivations of q. A detailed analysis of the computing cost is given below.

3.1.3 Computing Cost Comparison

From the previous discussion on damping effect and accuracy comparisons, the absorbing techniques show a coherent advantage in absorbing fluctuations of both aerodynamic and acoustical pulses; they are much better than NSCBC. The PML is more accurate than the Freund's absorbing method, but an auxiliary variable q is defined for the PML. Sine q depends on space and time it could give rise to additional computational cost. Instinctively, it can be expected that NSCBC has lowest cost, then Freund's technique, while the PML would take the most computing time.

The CPU time for Test 1, Test 2, Test 3, Test 4 and the reference computation are equal to 12:40, 24:49, 18:03, 53:06 and 74:44, respectively (1000 time-steps for each test). Test 1 (NSCBC) does not include any non-physical region; therefore, this time 12:40 represents the computing time for the solution of the physical domain. The additional time rang up for Test 2, Test 3 and Test 4 compared to Test 1 is 12:09, 5:23 and 40:26, respectively. It should be pointed out that, only Test 4 (absorbing BC with D = 2) has an accuracy comparable with Test 2 (PML), but the additional cost is at lest 3 times larger than Test 2. It suggests that, if computing cost and accuracy is a criterion, the PML is much more preferable than the Freund's absorbing technique.

3.2 Propagation of a Plane Pressure Pulse

A plane pulse is initiated in the quiescent fluid and it is allowed to propagate into the computational domain. The non-dimensional parameters for the length, time, density, velocity, pressure and temperature are specified as; L_0, L_0/c_0, ρ_0, c_0, ρc_0^2, T_0 and the Reynolds number is defined as $Re = \rho_0 L_0 c_0 / \mu$. Since the speed of sound c_0 is chosen as the characteristic velocity scale, the computational speed of sound within the computational region is set to 1 at every grid point initially. The dimensionless speed of sound at the various grid points in subsequent time will take on values given by the solution of the modeled Boltzmann equation.

This 1-D problem aims to validate the robustness of DNS computations and, at the same time, to test the NSCBC boundary. The initial fluid state is defined as a small plane pressure fluctuation in the center of a tube, such that

$$\rho = \rho_\infty,\ u = 0,\ v = 0,\ p = p_\infty + \varepsilon \exp(-\ln 2 \times \frac{x^2}{0.08^2}) \quad , \tag{3.3}$$

where mean field density and pressure are given by $\rho_\infty = 1$ and $p_\infty = 1/\gamma$, the pulse amplitude ε is set to 4×10^{-6}, 16×10^{-6} and 100×10^{-6}, respectively, and $\mathrm{Re} = 5000$ is specified in this case.

For this open region problem, the initialed 1-D disturbance would propagate to the left-hand side and right-hand side, the solutions should be only related to the *x*-location and time. In another word, if using a finite computational domain to simulate this open region problem, the upper and lower numerical boundaries should let the 1-D wave propagating along it without any change. Therefore the buffer-zone techniques such as PML or absorbing BC can not be used at upper and lower boundaries. Otherwise, the disturbances would be “damped”, then, near the upper and lower boundaries, the solutions would not 1-D only. To simulate this 1-D problem correctly, NSCBC is selected to treat these boundaries. Because NSCBC can let the disturbances out in the normal direction, and at the same time do not affect waves along the boundaries. Therefore if a 1-D wave is propagating along the boundary, the wave front would be rectangular to the boundary all the time. This property would be proved in the following discussion.

For the left-hand side and right-hand side boundaries, PML absorbing boundaries are used to give non-reflecting boundaries. The physical domain of this problem is defined as $-5 \le x \le 5$ by $0 \le y \le 2$. A uniform grid of size 0.02x0.02 is adopted. The buffer regions for the left-hand side and right-hand side absorbing boundary conditions are located at $-7 \le x \le -5$ and $5 \le x \le 7$ respectively. $\Delta t = 0.0001$ is chosen for the present computations.

Fig. 3.15 shows the contours of density fluctuations inside the physical region at t = 1.0 and t = 3.0 for the case $\varepsilon = 100 \times 10^{-6}$. It can be proved that this 1-D pulse is normal to the upper and lower NSCBC boundaries. NSCBC keeps this 1-D wave without any changes near the boundaries.

Fig. 3.16 and Fig. 3.17 show the density and pressure fluctuations along the centerline of the tube at t = 1.0 and t = 3.0 respectively. It is obviously that, after the acoustic waves go away, the density fluctuations in the central region appear and stay in the center, these fluctuations are actually solutions of the entropy wave. If checking the acoustic waves, the two positive density fluctuation peaks are leaving the center with a propagation speed $c = 1$ and the amplitude of this density fluctuation is $\hat{\rho} = 4 \times 10^{-5}$ (t = 3.0). At the same corresponding positions, there are two pressure fluctuation peaks with a value of $\hat{p} = 4 \times 10^{-5}$. Actually these two waves are the exact acoustic waves because the transmission speed is the physical sound speed and the amplitudes follow the acoustic relation, $\hat{p} = c^2 \hat{\rho}$. These results show that the proposed DNS can replicate the correct acoustic waves and the calculated macroscopic quantities are developing correctly.

3.3 Propagation of a Circular Pressure Pulse

If an initial circular pulse were imparted to a uniform fluid, the fluctuations thus created would propagate equally in all directions. This means that, at any time, the pulse would remain circular in shape. A circular initial pressure pulse is used to validate the direction problem of this DNS scheme. The distribution is defined as

$$\rho = \rho_\infty ,\ u = 0 ,\ v = 0 ,\ p = p_\infty + \varepsilon \exp(-\ln 2 \times \frac{x^2 + y^2}{0.2^2}) \quad , \tag{3.4}$$

where $\rho_\infty = 1$, $p_\infty = 1/\gamma$, $\varepsilon = 16 \times 10^{-6}$ and $Re = 5000$. The physical domain is $-10 \le x \le 10$ and $-10 \le y \le 10$, the grid size is 0.05x0.05. The physical region is closed by four buffer layers with width are equal to 1. PML absorbing technique is used for these buffer regions. Fig. 3.18 and Fig. 3.19 show contours of pressure fluctuations and “u” fluctuations at time *t=2.5* and *t=5.0* respectively. It can be shown that, the pressure fluctuations inside Fig. 3.18a and Fig. 3.18b are in good circular shape, it means that the disturbances are developing equally from all the directions to the outside.

3.4 Plane Sinusoidal Wave Propagation in Quiescent Fluid

Plane sinusoidal wave propagation in quiescent fluid is calculated in this case. The initial conditions of the fluid are $\rho = \rho_\infty = 1$, $u = 0$, $v = 0$ and $p = p_\infty = 1/\gamma$. The pressure at location $x = x_e$ is forced to follow a weak excitation with amplitude ε_p and wavelength λ, Fig. 3.20 shows the specification of this problem,

$$p_e = p_\infty \left[1 + \varepsilon_p \sin\left(\frac{2\pi c}{\lambda} t \right) \right] \quad , \tag{3.5}$$

where c=1 is the speed of sound. Because it is still a plane wave problem, the same boundary set-up as case 1 is used. PML absorbing boundary condition is adopted on the inlet and outlet boundaries with two buffer regions with respective size

$D_I = D_O = 1$. The upper and lower are using NSCBC. Two calculations are performed and the calculated density fluctuations. One is excited with $\lambda = 2$ (short waves) and $\varepsilon_p = 10^{-5}$ (Fig. 3.21) where the other is with $\lambda = 10$ (long waves) and $\varepsilon_p = 1.8 \times 10^{-4}$ (Fig. 3.22). Obviously, this DNS scheme can calculated all these waves correctly and there is no spurious reflecting from all the boundaries.

3.5 Speed of Sound in Flows with Different Mach Numbers

This section aims to validate the propagation speed of sound is correct in different Mach number flow conditions. As mentioned in Chapter 1, using the one-step method, the Navier-Stokes equations together with the gas equation of state are solved directly; the propagation speed of sound inside the flow is not defined but calculated from these governing equations. Therefore there is a need to validate the calculated speed of sound is indeed correct under different mean flow conditions. A simple 1-D Gaussian acoustic pulse is developing inside the mean flow. The characteristic scales for speed, time, density, pressure and temperature are defined from the mean flow quantities u_0, l_0 / u_0, ρ_0, $\rho_0 u_0^2$ and T_0, respectively. Therefore a Mach number for this mean flow could be defined as $M = u_0 / c_0$. Thus normalized, in the computational domain, the mean flow density, velocity, pressure and temperature are $\rho_\infty = 1$, $u_\infty = 1$, $v_\infty = 0$, $p_\infty = 1/\gamma M^2$ and $T_\infty = 1$, respectively. Physically the speed of sound should be $c_\infty = 1/M$. The initial condition is set to:

$$\rho = \rho_\infty + \varepsilon \exp(-\ln 2 \times \frac{(x+1)^2 + y^2}{0.2^2}) \quad , \tag{3.6a}$$

$$u = u_\infty \quad , \tag{3.6b}$$

$$v = v_\infty \quad , \tag{3.6c}$$

$$p = p_\infty + \frac{1}{M^2}\varepsilon \exp(-\ln 2 \times \frac{(x+1)^2 + y^2}{0.2^2}) \quad , \tag{3.6d}$$

where $\varepsilon = 10^{-4}$. Altogether 9 different inlet flows are investigated M = 0.01, 0.0125, 0.02, 0.05, 0.1, 0.3, 0.5, 0.7 and 0.9 respectively.

Some sample plots of the pressure pulse for four M cases are shown in Fig. 3.23. From these plots, the distance S between the peaks can be determined and since the time lapse is known, the speed with which the peaks moved away from each other can be determined. The calculations are carried out for different S and t and sample plots for M = 0.01 and 0.9 are shown in Fig. 3.24. In this figure is also shown the least square fit of all the S and t points chosen for the two M cases presented. It should be noted that the gradients of these lines are in fact twice the sound speed for each individual Mach number flow. After deducing the sound speed values, the calculated propagation speeds of sound c are plotted in Fig. 3.25 versus different Mach number flows. These results show little or no error in the determination of c under different Mach number conditions within the range tested.

3.6 Summary

In this chapter, the boundary techniques were investigated. The comparisons show that the PML gives the most accurate solutions and the best time cost performance. In general, the PML requires a smaller computational domain, has a wider frequency range, and requires less computational time for the same aeroacoustic simulation problem. This method is used to calculate some basic aeroacoustic problems: single plane pressure pulse, single circular pressure pulse, continuous pulses, acoustic pulse under different Mach number flow conditions. These solutions would be used as reference in Chapter 5 to validate the LBM.

Table 3.1 Computational configurations for the test with three pulses.

Grids	Test	Computational Region: X direction, Y direction	Boundary Conditions (Damping layer width D)
Uniform ($\Delta X = \Delta Y = 0.05$)	1	X(-2.5, 2.5), Y(-2.5, 2.5)	NSCBC
	2	X(-3, 3), Y(-3, 3)	PML (D = 0.5)
	3	X(-3, 3), Y(-3, 3)	Freund (D = 0.5)
	4	X(-4.5, 4.5), Y(-4.5, 4.5)	Freund (D = 2)
	5 (Reference)	X(-6, 6), Y(-6, 6)	Freund (D = 1)

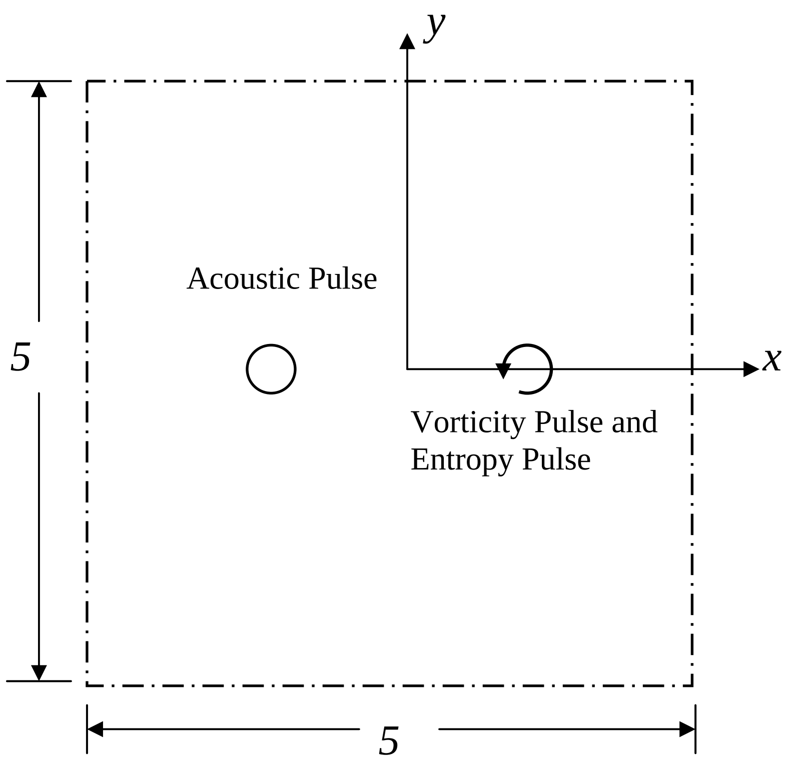

Figure 3.1 Configuration of three pulses in the flow.

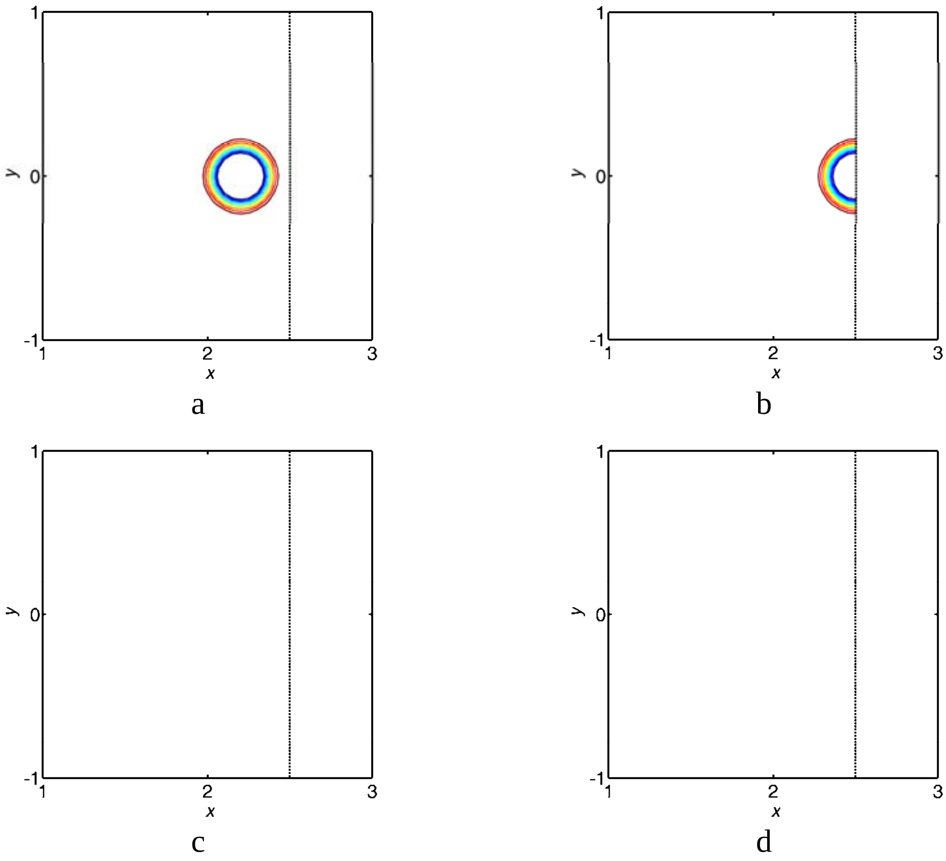

Figure 3.2 (NSCBC) Vorticity contours when time t is equal to 1.2, 1.5, 1.8 and 2.1.

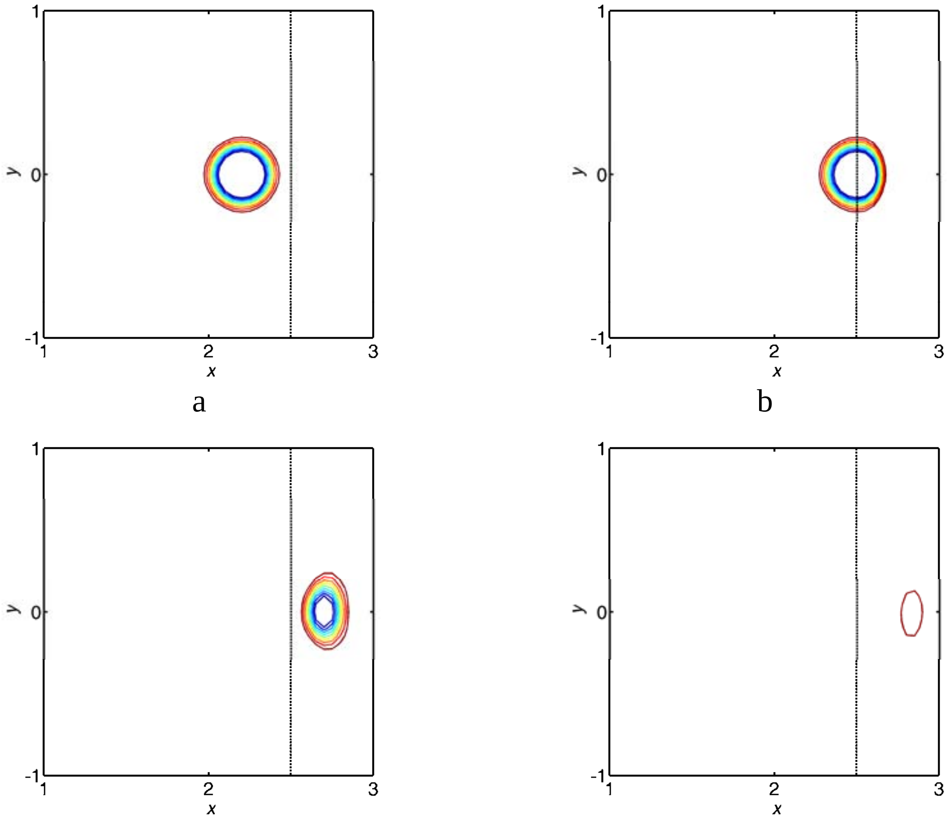

a

b

c

d

Figure 3.3 (PML) Vorticity contours when time *t* is equal to 1.2, 1.5, 1.8 and 2.1.

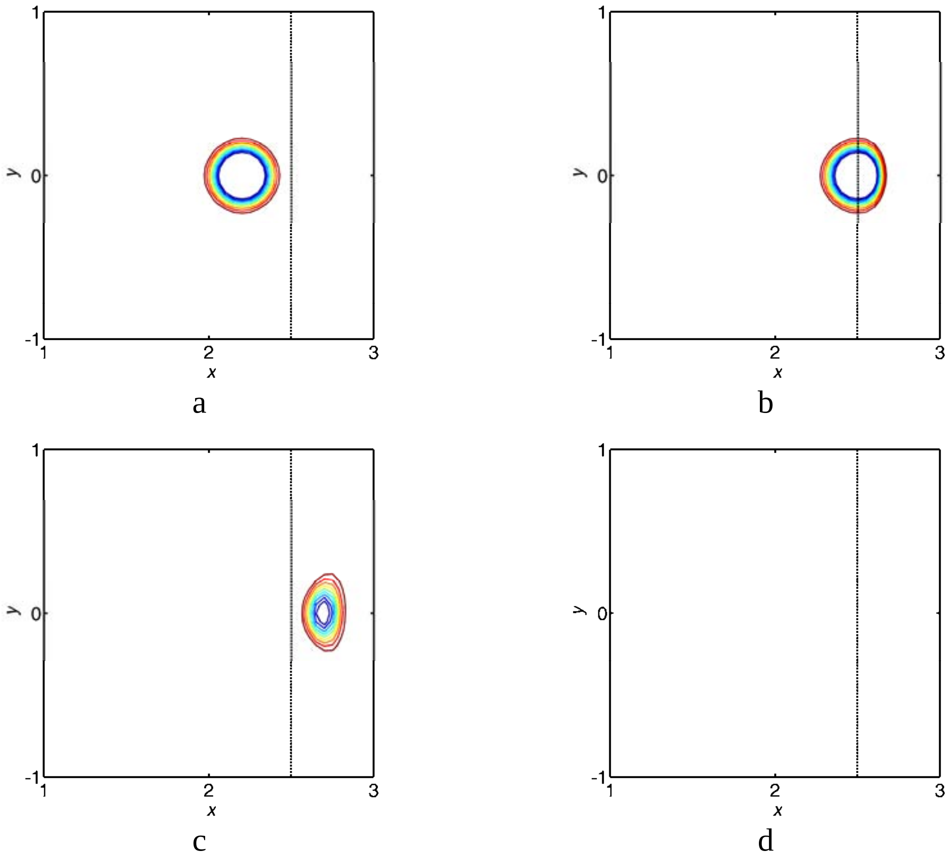

Figure 3.4 (Freund’s absorbing BC)Vorticity contours when time *t* is equal to 1.2, 1.5, 1.8 and 2.1.

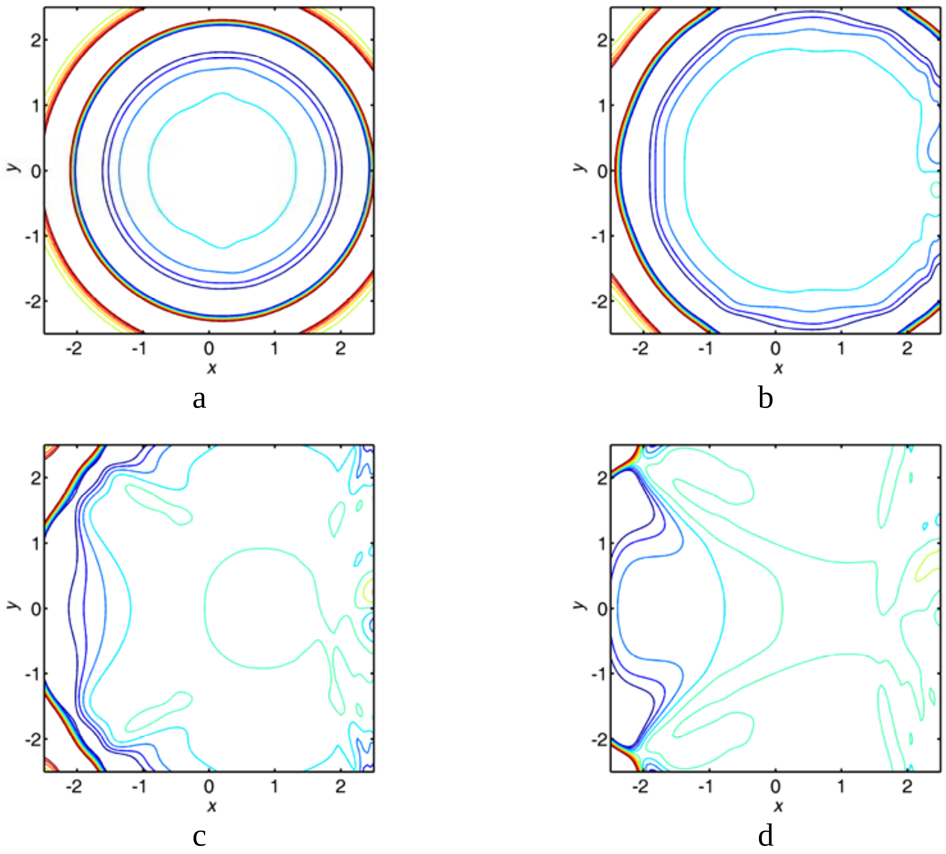

a

b

c

d

Figure 3.5 (NSCBC) Pressure contours when time *t* is equal to 1.2, 1.5, 1.8 and 2.1.

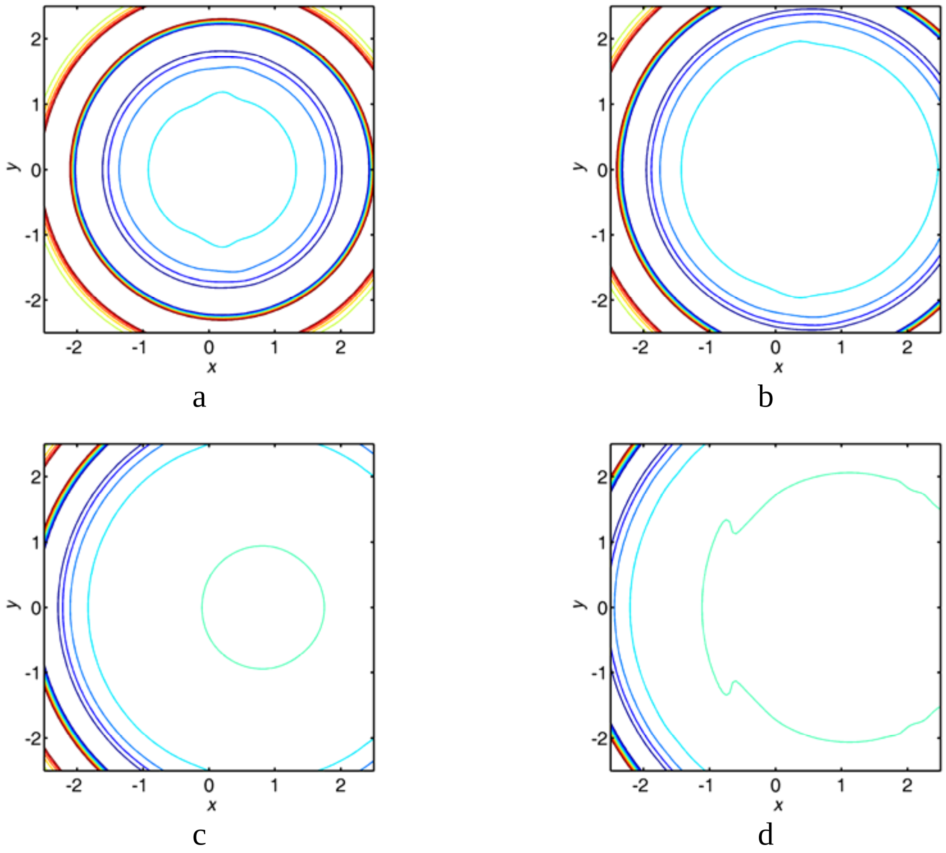

a

b

c

d

Figure 3.6 (PML) Pressure contours when time *t* is equal to 1.2, 1.5, 1.8 and 2.1.

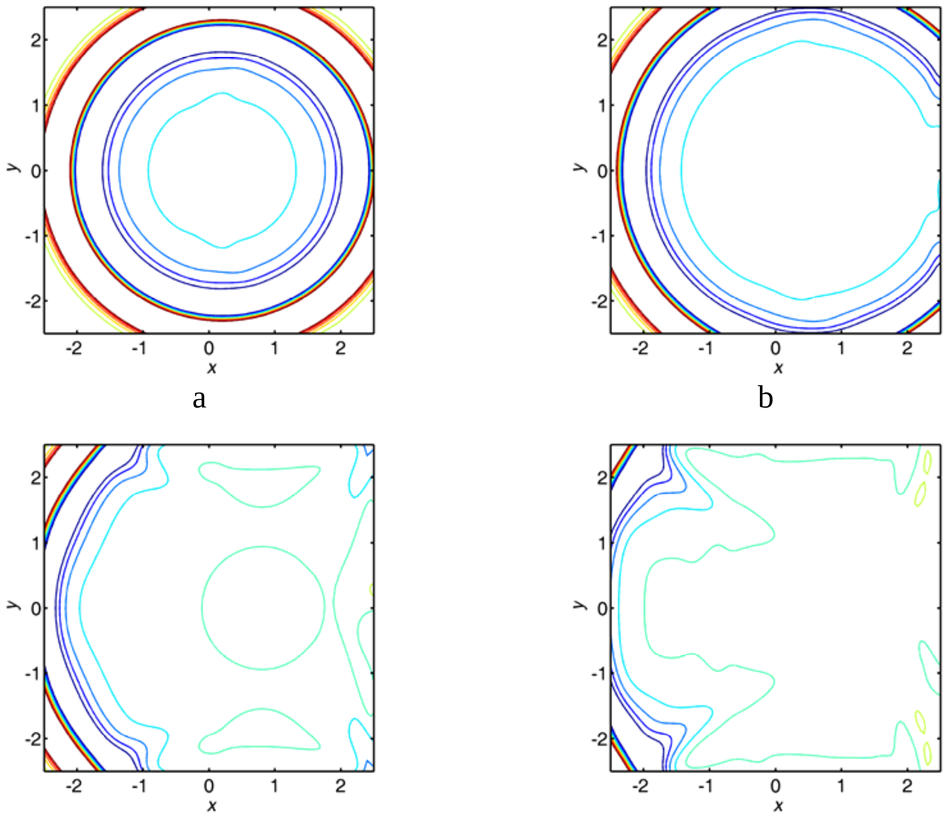

a b

c d

Figure 3.7 (Freund) Pressure contours when time *t* is equal to 1.2, 1.5, 1.8 and 2.1.

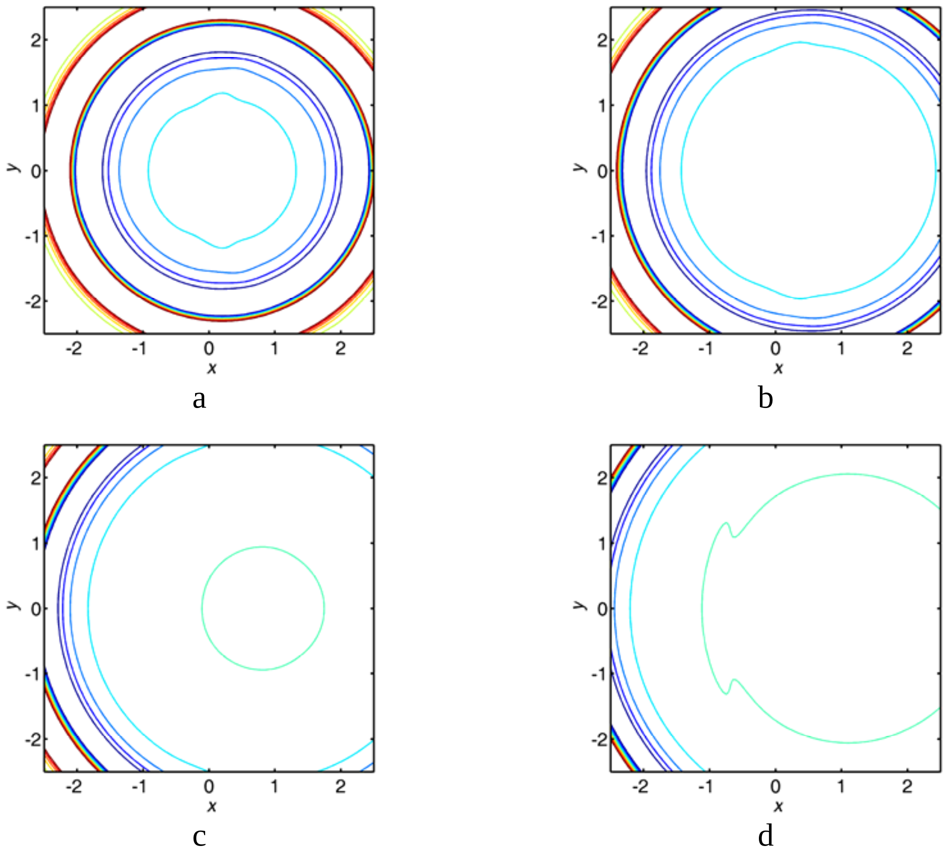

Figure 3.8 (Reference) Pressure contours when time *t* is equal to 1.2, 1.5, 1.8 and 2.1.

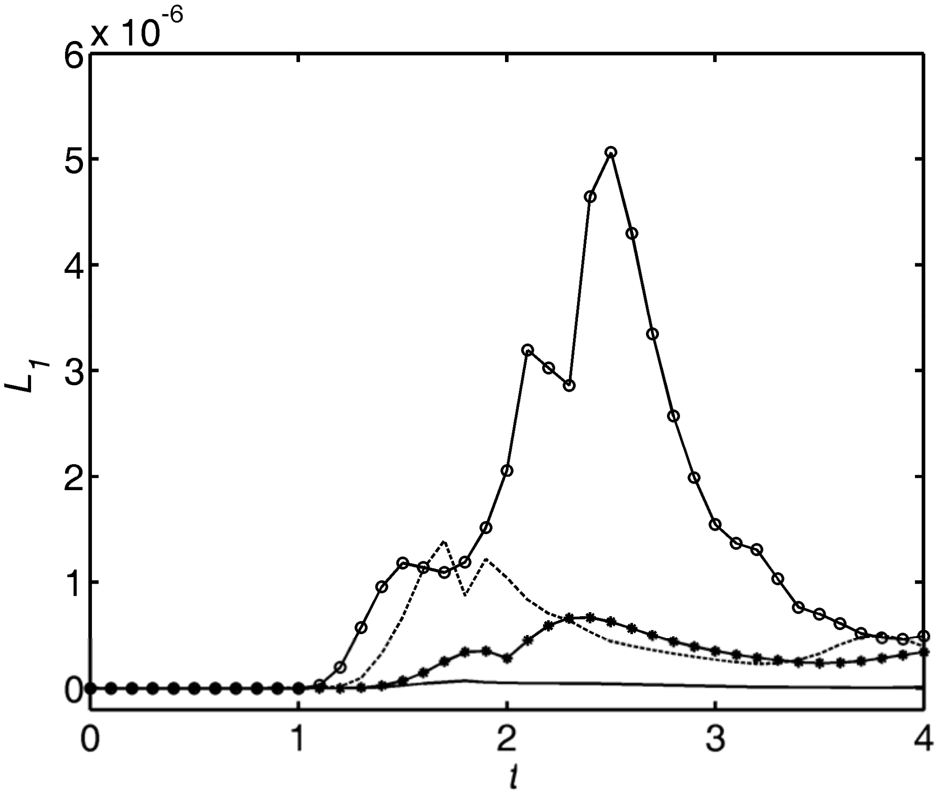

Figure 3.9 Pressure error L_1 histories for different boundary schemes: -o NSCBC; -- Freund’s absorbing BC; — PML; —* Freund’s absorbing BC with D=2.

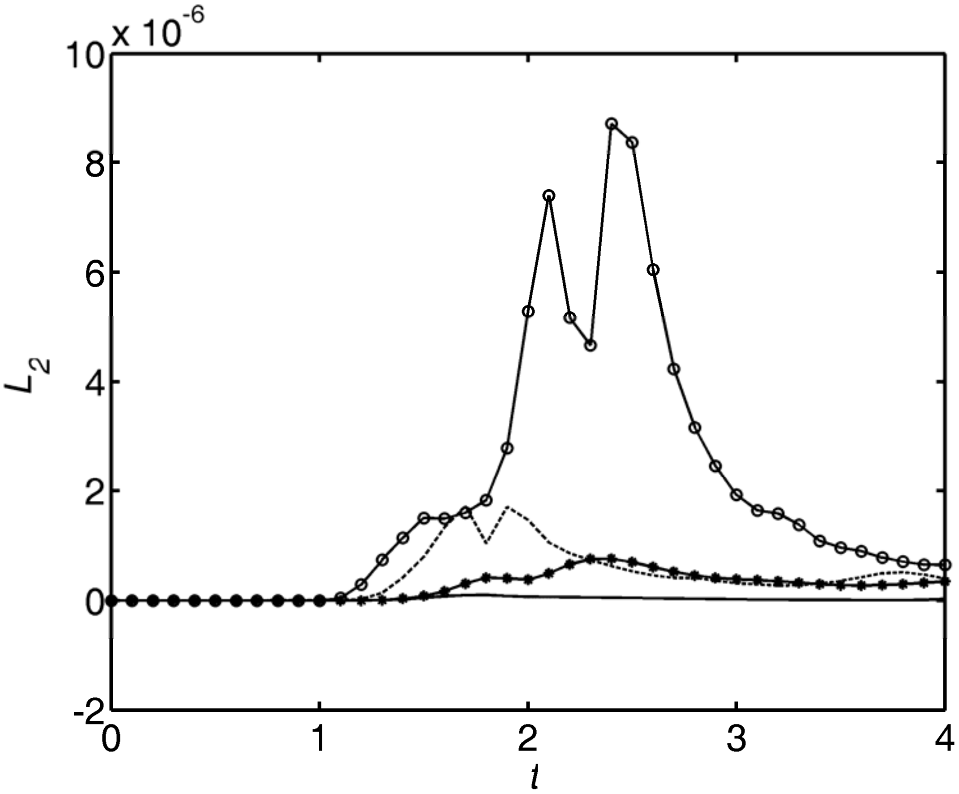

Figure 3.10 Pressure error L_2 histories for different boundary schemes: -o NSCBC; -- Freund's absorbing BC; — PML; —* Freund's absorbing BC with D=2.

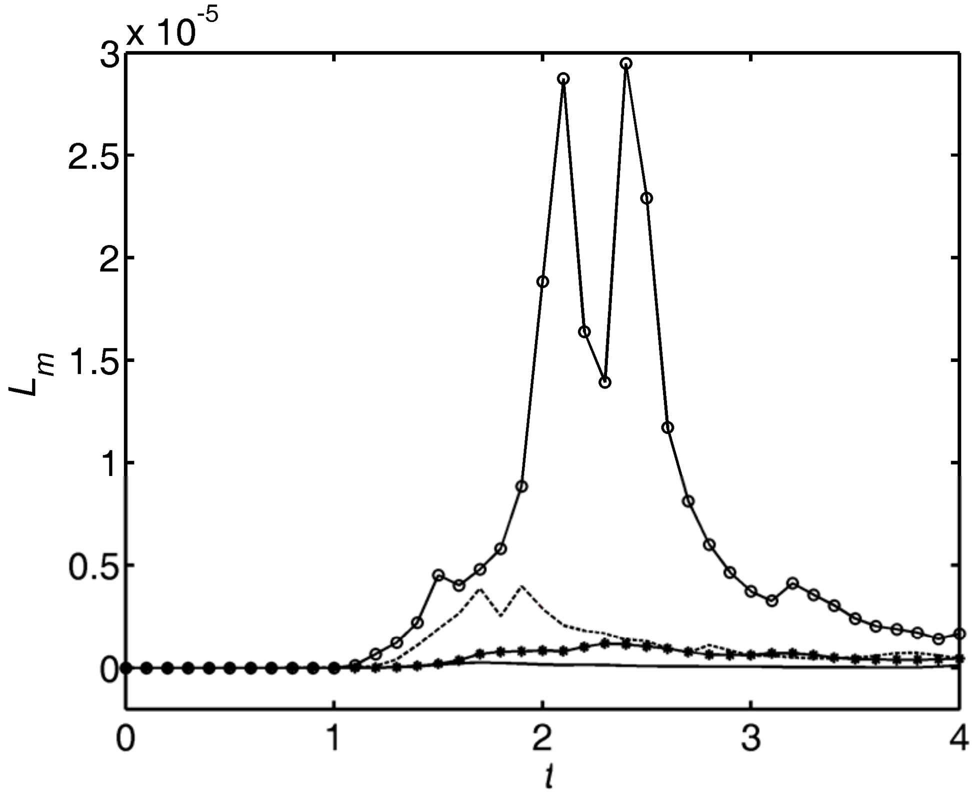

Figure 3.11 Pressure error L_m histories for different boundary schemes: -o NSCBC; -- Freund’s absorbing BC; — PML; —* Freund’s absorbing BC with D=2.

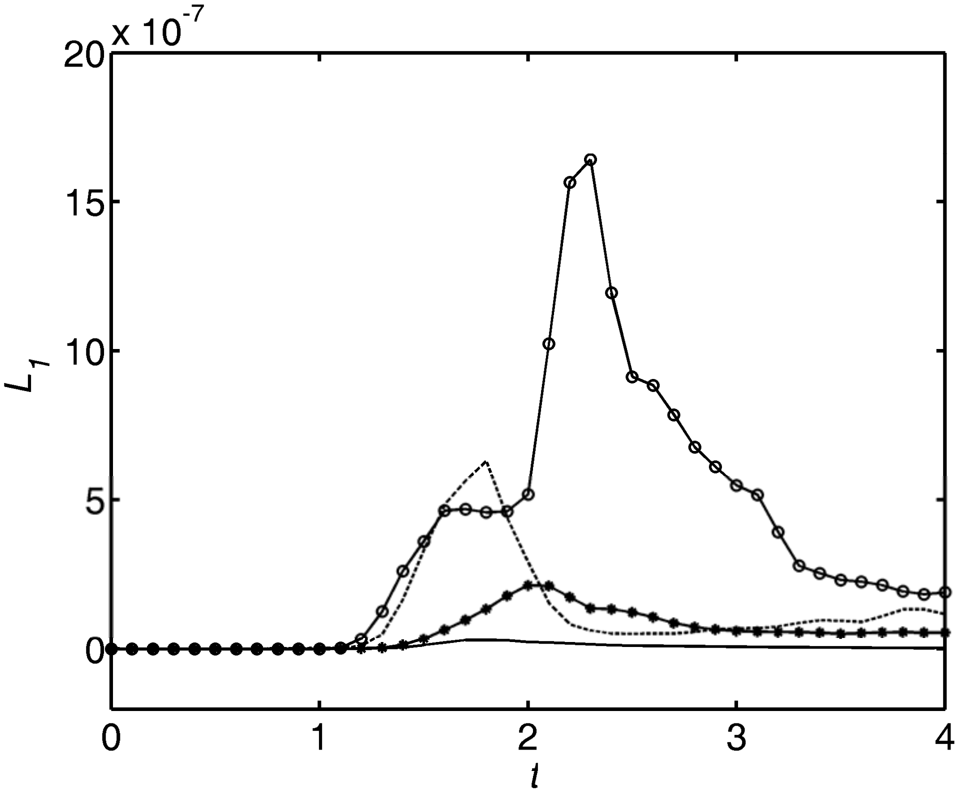

Figure 3.12 “u” error L_1 histories for different boundary schemes: -o NSCBC; -- Freund’s absorbing BC; — PML; —* Freund’s absorbing BC with D=2.

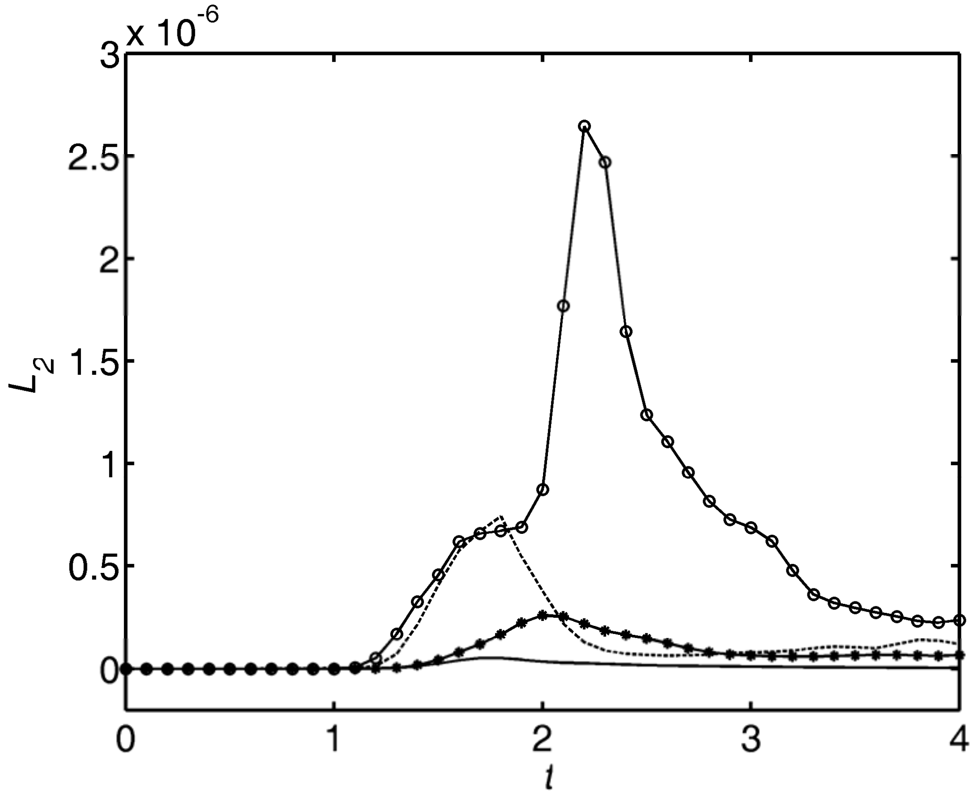

Figure 3.13 “u” error L_2 histories for different boundary schemes: -o NSCBC; -- Freund’s absorbing BC; — PML; —* Freund’s absorbing BC with D=2.

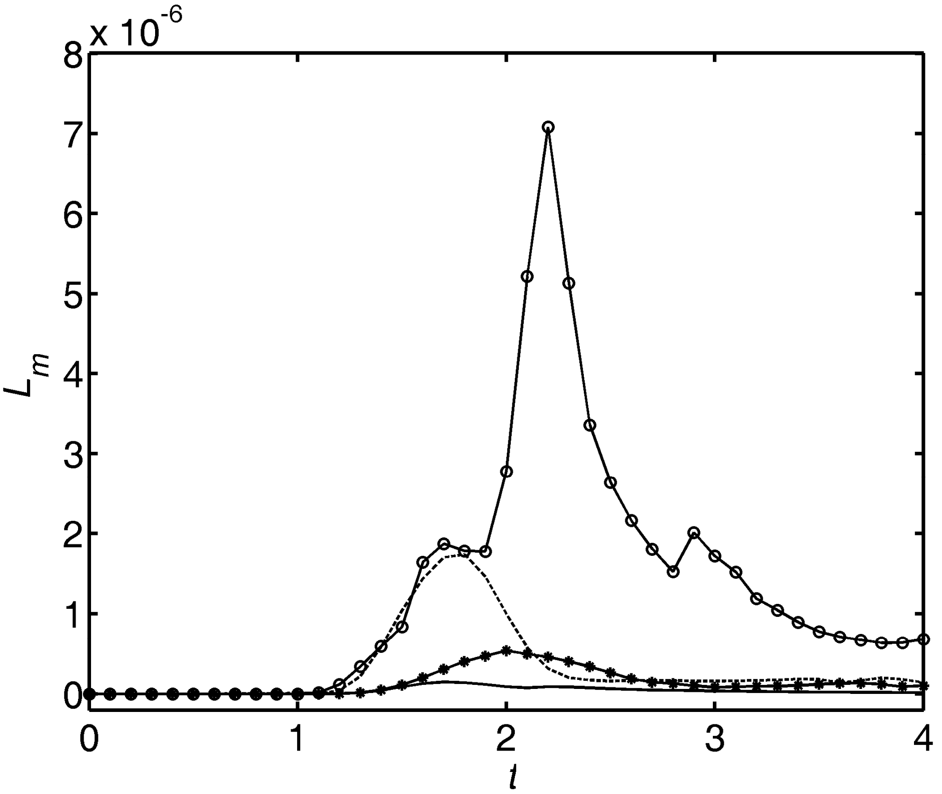

Figure 3.14 "u" error L_m histories for different boundary schemes: -o NSCBC; -- Freund's absorbing BC; — PML; —* Freund's absorbing BC with D=2.

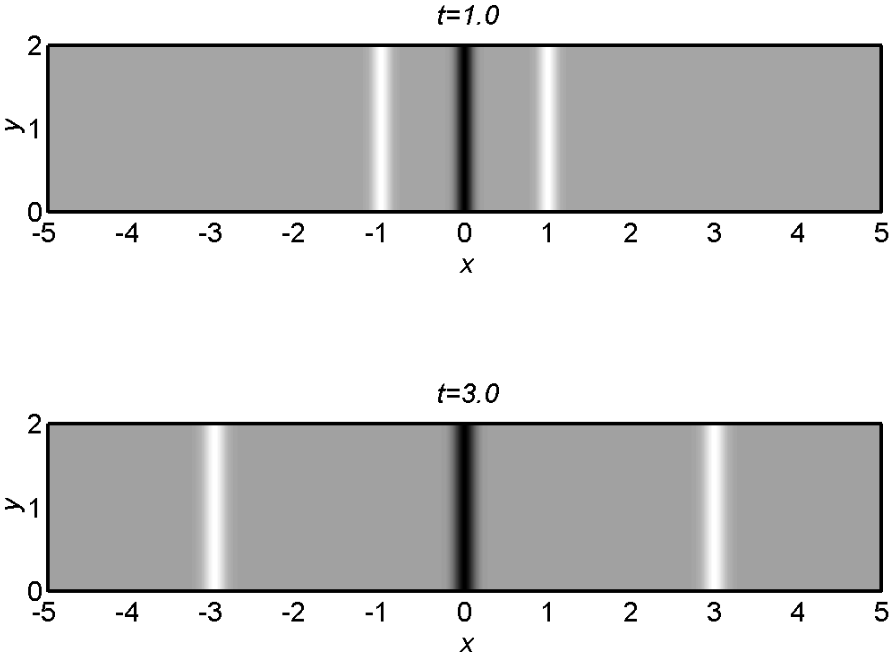

Figure 3.15 Density fluctuations contours of a plane pressure pulse (*t*=1.0 and *t*=3.0).

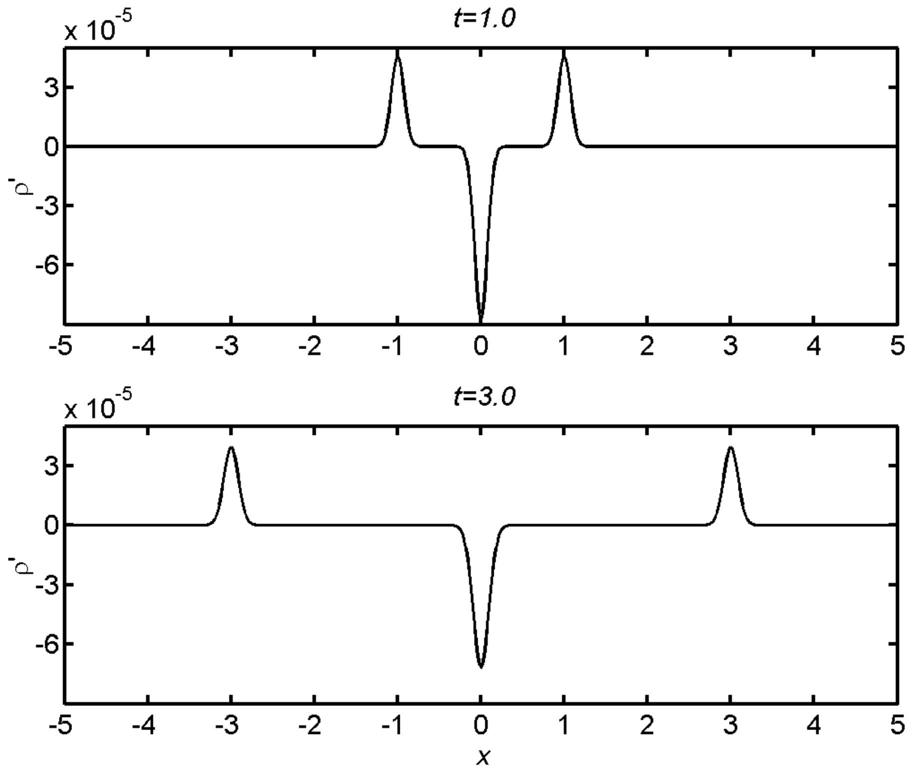

Figure 3.16 Density fluctuations along the center of tube for a plane pressure pulse (t=1.0 and t=3.0).

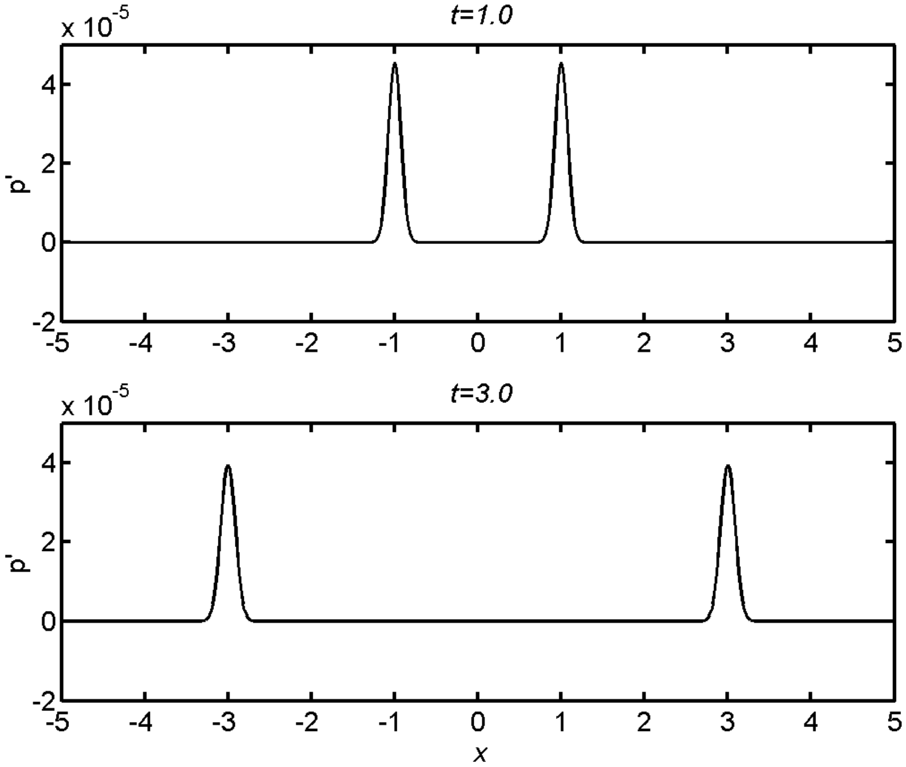

Figure 3.17 Pressure fluctuations along the center of tube for a plane pressure pulse (t=1.0 and t=3.0).

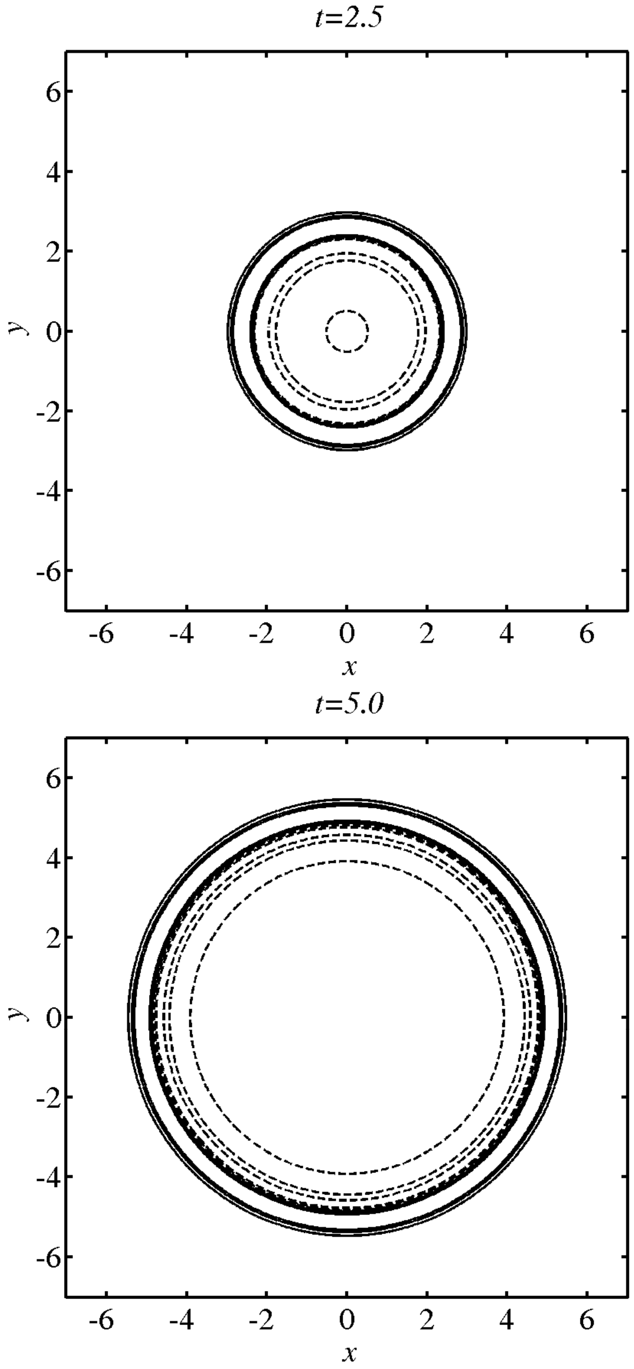

Figure 3.18 Pressure contours for a circular pressure pulse (*t*=2.5 and *t*=5.0).

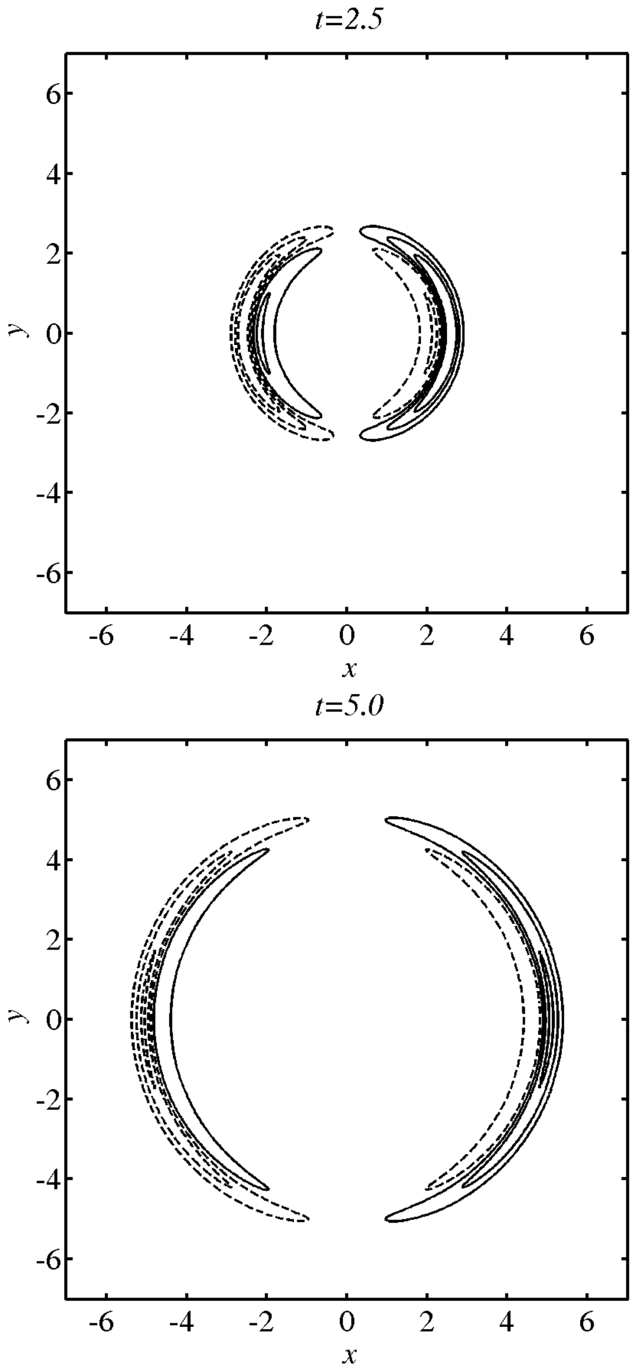

Figure 3.19 Velocity “u” contours for a circular pressure pulse (*t*=2.5 and *t*=5.0).

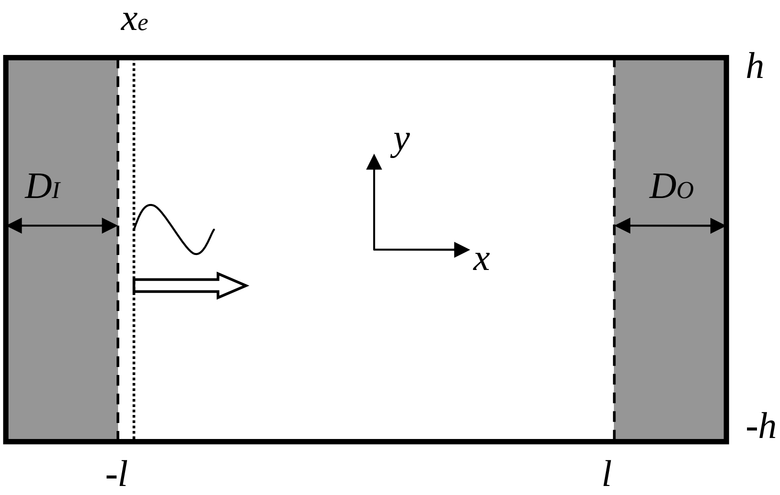

Figure 3.20 Specification of computation plane sinusoidal wave propagation in quiescent fluid.

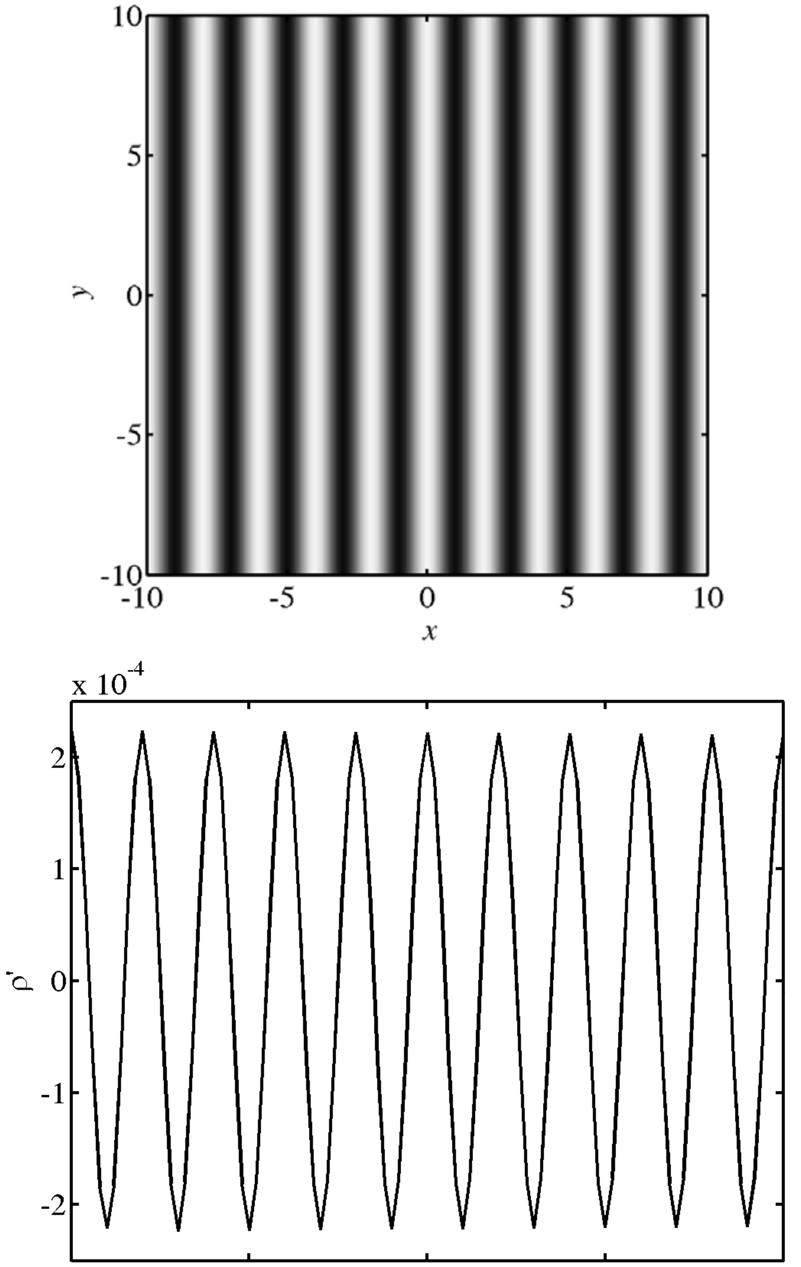

Figure 3.21 Propagation of sound wave in the x-direction: (a) density fluctuation contours; (b) distributions along the center-tube for continuous waves ($\lambda = 2$).

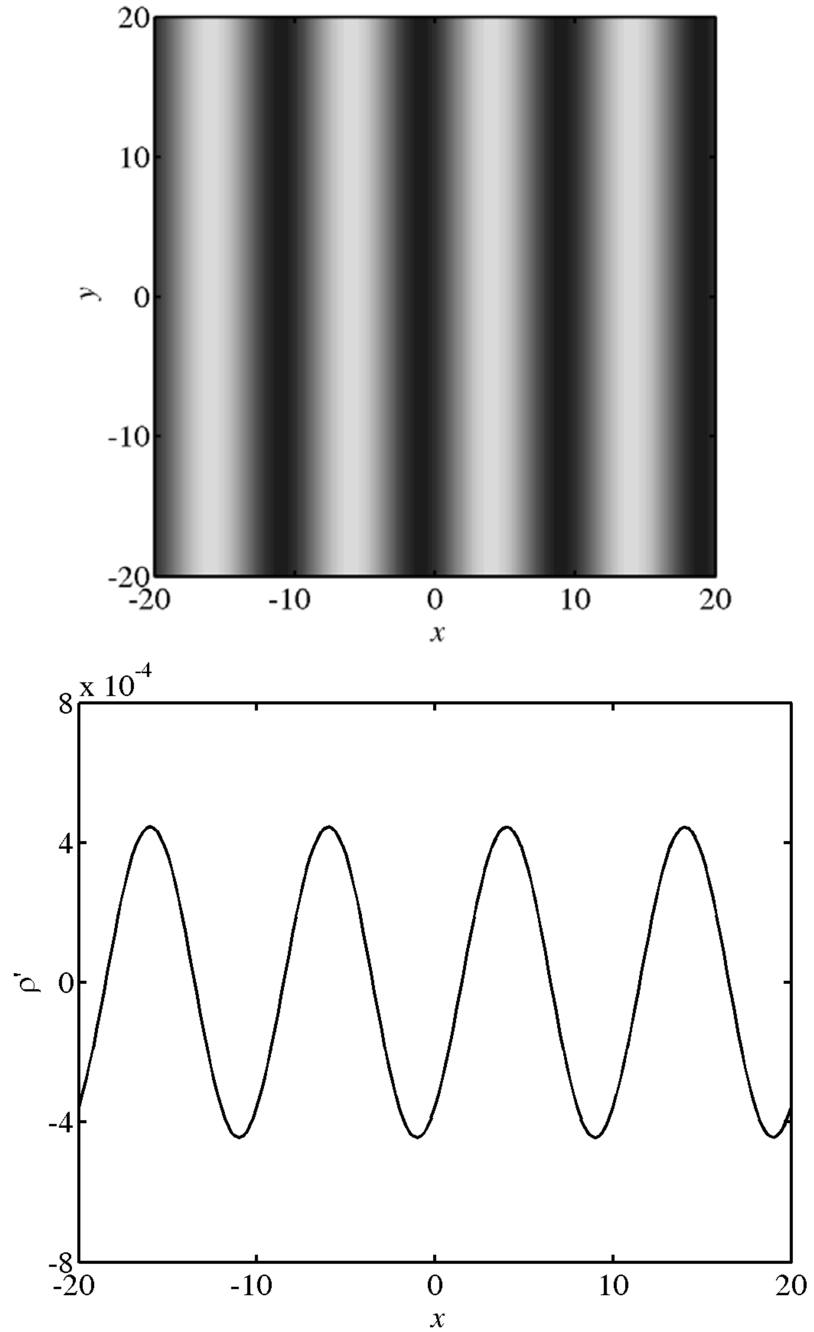

Figure 3.22 Propagation of sound wave in the x-direction: (a) density fluctuation contours; (b) distributions along the center-tube for continuous waves ($\lambda = 10$).

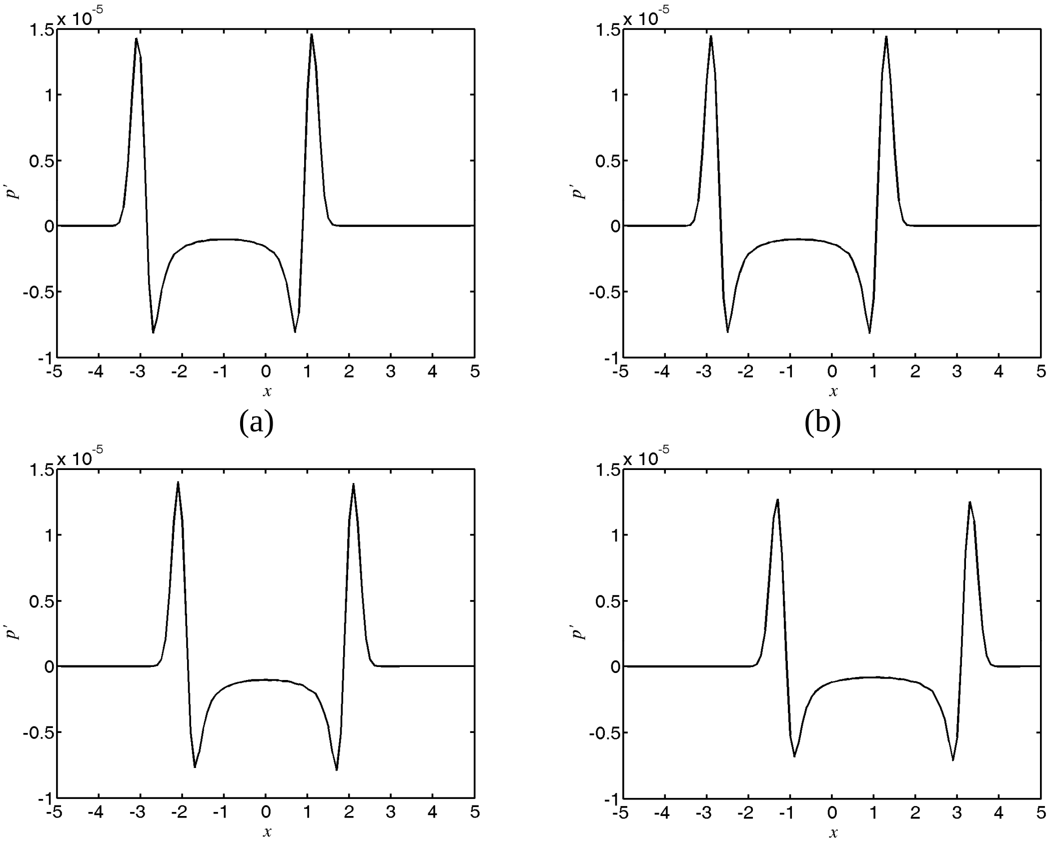

(a) (b)

(c) (d)

Figure 3.23 Instantaneous pressure fluctuations along the x-axis: (a) M = 0.01, *t* = 0.02; (b) M = 0.1, *t* = 0.2; (c) M = 0.5, *t* = 1.0; (d) M = 0.9, *t* = 1.8.

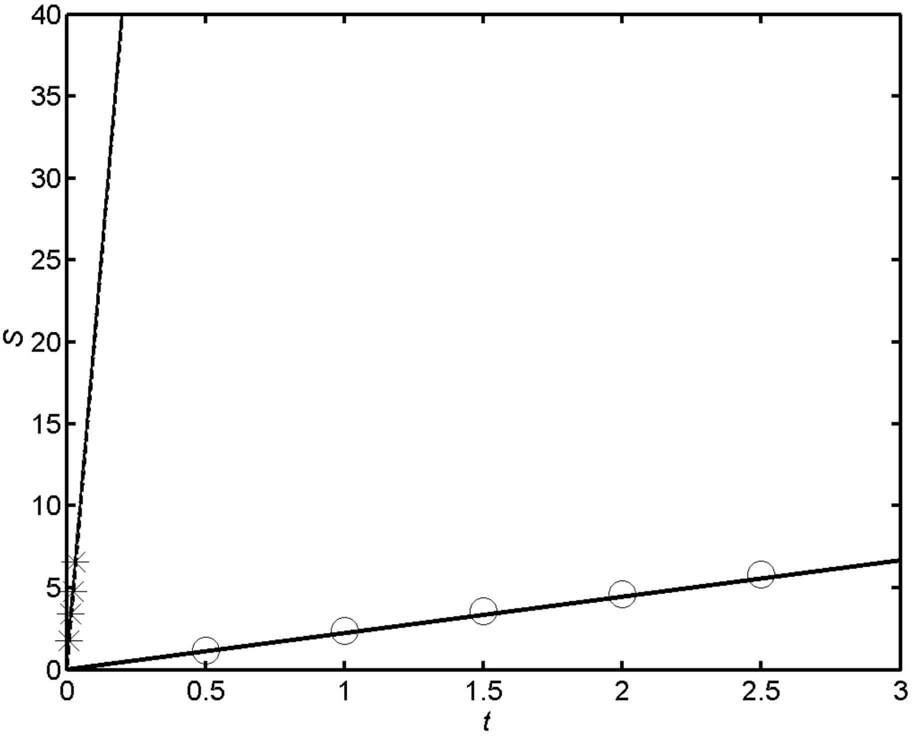

Figure 3.24 A plot of the distance S between two maximum peaks versus time *t*.

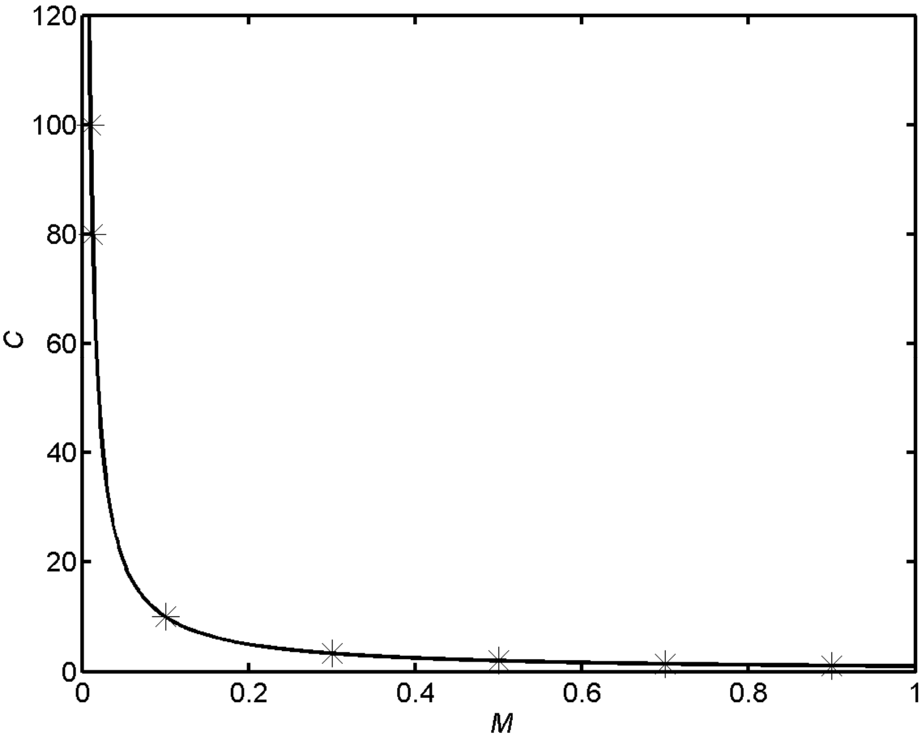

Figure 3.25 A plot of the propagation speed of sound c versus Mach number M.

4 Introduction to Lattice Boltzmann Method

In Chapter 2 and Chapter 3, an effective one-step CAA method has been used to calculate some basic acoustic pulse cases and some classical aeroacoustic problems. In all cases studied, the 2-D fully unsteady compressible Navier-Stokes equations are solved. These equations are derived based on the continuum assumption for the fluid. The higher-order transport terms such as the viscous stress and heat flux terms are derived by invoking the Stokes stress hypothesis and the Fourier law. As a result, second-order spatial derivatives appear in the governing equations. These inherent features cause certain difficulties in solving these governing equations numerically; such as stability considerations when these second-order terms are evaluated numerically. At the same time, it is not easy to build parallel algorithm codes to fully utilize the efficiency of the computers; this consideration is especially important in CAA because the computational time is an important issue to consider. In view of this, a numerical simulation scheme for CAA that is most amenable to parallel computation should be developed. The Boltzmann equation is a scalar equation (Cercignani 1975) and is quite amenable to parallel computation if it is used for CAA. Therefore, in this chapter, a one-step CAA method using LBM will be introduced. The Chapter begins with a brief discussion of the Navier-Stokes equations, because if the LBM is used to simulate aeroacoustic problems it is necessary to show that the LBM should recover the fully unsteady compressible Navier-Stokes equations and the equation of state correctly.

4.1 Navier-Stokes Equations

The Navier-Stokes equations are derived by invoking the continuum hypothesis, where the various fluid properties such as the density, velocity and temperature (or the internal energy) are assumed to be continuous functions of position with characteristic volume scale of 10^{-9} cm^3 (Batchelor 1970). In other words, the particle nature of the material is already smoothed in this scale, small though this volume is, it contains about 3×10^{10} molecules of air at normal temperature and pressure. Therefore, when given a specified volume, the fluid should follow the conservation of mass, momentum and energy equations since all the scale quantities should be continuous. These conservation equations can be expressed as

$$\frac{\partial\rho}{\partial t}+\frac{\partial(\rho u_\alpha)}{\partial x_\alpha}=0 \quad , \tag{4.1}$$

$$\frac{\partial(\rho u_\alpha)}{\partial t}+\frac{\partial(\rho u_\alpha u_\beta)}{\partial x_\beta}=-\frac{\partial p}{\partial x_\alpha}+\frac{\partial\tau_{\alpha\beta}}{\partial x_\beta} \quad , \tag{4.2}$$

$$\frac{\partial}{\partial t}\left(\rho e+\frac{1}{2}\rho \mathrm{u}^2\right)+\frac{\partial}{\partial x_\alpha}\left[\left(\rho e+\frac{1}{2}\rho \mathrm{u}^2+p\right)u_\alpha\right]=-\frac{\partial q_\alpha}{\partial x_\alpha}+\frac{\partial}{\partial x_\alpha}\left(u_\beta\tau_{\alpha\beta}\right). \tag{4.3}$$

Summation over repeated indices α and β is assumed. The viscous stress and the heat flux are derived from the Stokes stress hypothesis and the Fourier law, respectively, and are given by

$$\tau_{\alpha\beta}=2\mu\left(S_{\alpha\beta}+\frac{1}{3}\delta_{\alpha\beta}S_{\chi\chi}\right),\quad S_{\alpha\beta}=\frac{1}{2}\left(\frac{\partial u_\alpha}{\partial x_\beta}+\frac{\partial u_\beta}{\partial x_\alpha}\right) \quad , \tag{4.4a}$$

$$q_\alpha=-k\frac{\partial T}{\partial x_\alpha} \quad . \tag{4.4b}$$

They are related to the fluid transport coefficients μ and k, the first coefficient of viscosity of the fluid and the fluid thermal conductivity, respectively. These fluid properties are regarded as functions of temperature. Equations (4.1) - (4.3) are closed with the thermodynamic coupling of the internal energy, the pressure and the density through the equation of state for a perfect gas, i.e.

$$p = \rho RT \quad , \tag{4.5}$$

where the gas constant is given by $R = c_p - c_v$. Conventional approaches for direct aeroacoustic simulations proceed by truncating Eqs. (4.1) to (4.5), or their linearized forms, in the spatial domain and then resolve their temporal evolution by means of finite difference or finite volume techniques.

It should be pointed out that for certain fluids, such as non-Newtonian fluid, Eqs. (4.1) – (4.3) can still be derived by invoking the continuum assumption, but the high-order transport terms are not necessarily given by Eqs. (4.4a, b). In fact, these two hypotheses for the transport terms can be derived, with certain simplification, from particle collision theory. As will be shown later, the viscosity and the thermal conductivity could be obtained from the basic particle collision theory. This means that in order to deduce the conventional Navier-Stokes equations, some particle theories have to be invoked to evaluate the high-order transport terms. Since particle motion is considered, the governing equation for particle theory, namely the Boltzmann equation, should be considered.

4.2 Boltzmann Equation and the Conservation Law for Particles

Boltzmann equation (BE) considers the kinetic energy of discrete particles. If there is no external force, this equation can be simply expressed as the evolution of the single-particle distribution function based on a linear convection operator (steaming term) and a nonlinear collision (Harris 1999, Wolf-Gladrow 2000) term. The collision term should satisfy the conservation law for the particles, where the macroscopic quantities for the fluid, such as density, momentum, internal energy and energy flux, can be derived via moment integrations of this distribution function. It should be stressed that, using a multiscale Chapman-Enskog expansion about the

Knudsen number, the Navier-Stokes equations can be derived from the modeled BE (Harris 1999).

The lattice Boltzmann method (LBM) is originated from the lattice gas automata and is a numerical method used to solve the modeled BE. The LBM is discretized in phase (or velocity) space. It was proposed as an alternative to conventional computational fluid dynamics techniques (Chen et al 1992, Qian et al 1992) more than a decade ago. A variety of lattice Boltzmann methods have been established for different hydrodynamic systems (Chen & Doolen 1998), such as single component hydrodynamics (Michael and Dani 2003), multiphase and multicomponent flows (Gunstensen and Rothman 1993, Grunau et al 1993), particulate suspensions in fluid (Ladd 1993 and 1997, Behrend 1995, Aidun and Lu 1995), reaction-diffusion systems (Dawson et al 1993, Chen et al 1995), flows through porous media (Guo and Zhao 2002), etc. In kinetic theory of gases, the evolution of a fluid is described by the solutions to the continuous BE. Development of LBM for single-phase compressible flow, such as air, has received particular attention because they all recover the macrosopic Navier-Stokes equations in asymptotic limit of the Knudsen number (Chen et al 1992, Qian 1992, Frisch et al 1986, Frisch et al 1987). Due to the symmetry of the lattice, the conventional LBM was only able to simulate low Mach number flows in the incompressible limit. Here, the term conventional LBM is used to designate the lattice method used to solved the BE modeled by the (Bhatnagar, Gross and Krook 1954) BGK model. Using a fully discrete particle velocity model, where space and time are also discretized on a square lattice, internal energy of the particle is fixed; therefore, only isothermal flows can be simulated. This represents a limitation of the conventional LBM and remedies have been sought in the past.

There have been attempts to incorporate the effects of temperature variations in LBM for simulations of compressible flows and wave propagation. Sun (1998) introduced a particle potential energy term with arbitrarily adjusted specific heat ratio into conventional LBM on hexagonal lattice for shock wave simulations. Palmer and Rector (2000) modeled the internal energy as a secondary scalar distribution driven by the isothermal velocity distribution function and obtained good agreement in several thermal convection cases. However, the application of their model to aeroacoustic simulations is questionable because the equation of state is not explicitly recovered. Tsutahara et al. (2002) and Kang et al. (2003) attempted to include a particle rotational degree of freedom into the conventional LBM. Their approach was to define a new distribution function which was given by the product of the velocity distribution and a rotational energy term. They used the method to calculate shock reflection and the Aeolian tone of a circular cylinder and obtained qualitative agreement with DNS results. However, they have to use 21 discrete velocities at each lattice location for their computations.

In kinetic theory, a simple dilute gas, such as air, is represented as a cloud of particles and is fully described by a continuous particle distribution function $f(\boldsymbol{x},\xi,t)$, which is the probability of finding a particle at location $\boldsymbol{x}$ moving with microscopic velocity ξ. This function describes the distribution of the number of particles with speed ξ per unit volume. Thus *f* has the dimension of $(m/s)^{-3}m^{-3}$ for the three-dimensional speed space. Therefore, the total number of particles *N* per unit volume can be calculated by $N=\int f d\boldsymbol{\xi}$. It is a mesoscopic description of the fluid, which is intermediate between the macroscopic continuum model and the microscopic description. In this formulation, the fluid is treated as an avalanche of discrete interacting gas molecules. For a dilute gas in which only binary collisions between particles occur, the evolution of the distribution function is governed by the continuous Boltzmann equation (BE),

$$\frac{\partial f}{\partial t}+\boldsymbol{\xi}\cdot\nabla_{\boldsymbol{x}} f+\boldsymbol{F}_{ex}\cdot\nabla_{\xi} f=\int d^3\xi\int d\Omega\sigma(\Omega)\left|\xi-\xi_1\right|\left\{f(\xi')f(\xi_1')-f(\xi)f(\xi_1)\right\}=Q(f,f) \tag{4.6}$$

The left-hand side of Eq. (4.6) describes the streaming of particle motions. The variable $\boldsymbol{F}_{ex}$ indicates external body force due to gravity or electromagnetic origin. Since the rate of particle collision is unaffected by external body forces, $\boldsymbol{F}_{ex}=0$ is assumed in the present study. The operator Q accounts for the binary particle collision occurring within a differential collision cross section $\sigma(\Omega)$ which transforms the velocities from $\{\xi,\xi_1\}$ (incoming) to $\{\xi',\xi_1''\}$ (outgoing). In elastic collisions, the mass, momentum and kinetic energy of the particles are conserved. In other words, before the collision and after the collision, the total number of particles, their momentum and their translational energy would remain the same. Consequently, Q must possess exactly five collision invariants $\psi_s(\boldsymbol{\xi})$ $(s=0,1,2,3,4)$ in the sense that $\int Q(f,f)\psi_s(\boldsymbol{\xi})d^3\boldsymbol{\xi}=0$. The elementary collision invariants are $\psi_0=1$, $(\psi_1,\psi_2,\psi_3)=\xi$ and $\psi_4=|\boldsymbol{\xi}|^2$ which are proportional to mass, momentum and kinetic energy, respectively. These are the fundamental conservation laws for the particles. It would be demonstrated later in this chapter that these conservation laws can be used to recover the macroscopic properties and that the macroscopic Navier-Stokes equations for unsteady compressible flows are recovered correctly.

4.3 Density, Momentum and Internal Energy of Fluid

From the definition of the particle distribution function $f(\boldsymbol{x},\xi,t)$, which is the probability of finding a particle at location **x** moving with microscopic velocity ξ. If the particle mass *m* is included in both sides of the formula $N = \int f d\boldsymbol{\xi}$, it can be seen that $Nm = \int fmd\boldsymbol{\xi}$. Since *m* is a constant for a single component gas, the left hand side of this equation could be interpreted as the physical definition of density for the fluid. Because *m* is a constant for a single component gas, this constant is absorbed into the physical meaning of *f* in the following derivations and equations. Thus defined, *f* has the dimension of $kg(m/s)^{-3}m^{-3}$. Therefore the macroscopic fluid density and momentum can be easily derived as the zero-order and first-order integration of *f* over the whole velocity space. They are then given by

$$\rho = \int f d\xi \quad , \tag{4.7}$$

$$\rho \boldsymbol{u} = \int \xi f d\xi \quad . \tag{4.8}$$

The definition of fluid internal energy *e* needs consideration of the molecular nature of the fluid. As indicated in the following arguments, the realization of the diatomic nature of the fluid molecules is key to the successful recovery of the ideal gas equation of state, which is instrumental in a correct aeroacoustic simulation.

Monoatomic gas model is commonly adopted in most previous LBM. In this model each gas particle supports only translational motions with D_T degrees of freedom. This appears not appropriate to aeroacoustics since the fluid medium of interest is mostly air, which is mainly composed of diatomic nitrogen and oxygen gases. Generally, a polyatomic gas particle can undergo rotational motions with additional D_R degrees of freedom. This indicates that both translational and rotational kinetic energies of the polyatomic gas particles should be taken fully into account for a correct definition of the macroscopic internal energy. For diatomic gas like air, the total number of degrees of freedom is $D_T + D_R = 5$. From statistical mechanics theory, the kinetic energy should be equally distributed on each degree of freedom. It should be noticed that the term, $\int \frac{1}{2} f \left|\xi\right|^2 d\xi$, represents the summation of *translational energies* of D_T degrees. The kinetic energy on each degree of freedom may be defined as $\frac{1}{D_T} \int \frac{1}{2} f \left|\xi\right|^2 d\xi$. Therefore, with the total number of degrees of freedom given by $D_T + D_R$, the internal energy of the particles can be defined $\frac{D_T + D_R}{D_T} \int \frac{1}{2} f \left|\xi\right|^2 d\xi$, and the second order velocity moment integration would give the macroscopic internal energy for the fluid as

$$\rho e + \frac{1}{2} \rho \left|\mathbf{u}\right|^2 = \frac{D_T + D_R}{D_T} \int \frac{1}{2} f \left|\xi\right|^2 d\xi \quad . \tag{4.9}$$

The fluid energy flux can be defined via the second and third velocity moments as follows,

$$\left(\rho e + p + \frac{1}{2} \rho \left|\mathbf{u}\right|^2 \right) \mathbf{u} = \frac{D_T + D_R}{D_T} \int \frac{1}{2} f \left|\xi\right|^2 \xi d\xi \quad . \tag{4.10}$$

Integration of Eq. (4.9) suggests an explicit internal energy definition $e = \left(D_T + D_R\right) RT / 2$ for diatomic gas (Appendix A). Actually, it can be shown that, with the definitions of macroscopic fluid variables described in Eqs. (4.7) - (4.10), the unsteady compressible Navier-Stokes equations and the ideal gas equation of state can be completely recovered from the BE with a certain microscopic collision model and the Chapman-Enskog expansion assumed (Chapman & Cowling 1970).

4.4 Recovery of Navier-Stokes Equations

The collision operator *Q* contains all the details of the binary particle interactions but it is very difficult to evaluate due to the complicated structure of the integral.

Simpler models for Q have been proposed. The idea behind modeling is that the vast amount of details of the particle interactions is not likely to influence significantly the values of many experimentally measured macroscopic quantities (Cercignani 1990). It is expected that the fine structure of $Q(f,f)$ can be replaced by a blurred image based on a simpler operator $J(f)$ which retains only the qualitative and average properties of the true operator. Furthermore, the H-theorem shows that the average effect of collisions is to modify f by an amount proportional to the departure from the local Maxwellian-Boltzmann equilibrium distribution f^{eq} which is expressed in D spatial dimensions as,

$$f^{eq} = \frac{\rho}{(2\pi RT)^{D/2}} \exp\left(-\frac{|\boldsymbol{\xi} - \mathbf{u}|^2}{2RT} \right) \quad . \tag{4.11}$$

Therefore, the collision operator is approximated as $J(f) = -\omega\left(f - f^{eq}\right)$. In case of a fixed collision interval, i.e. $\omega = 1/\tau$, the well-known BGK, or single-relaxation-time (SRT) model for monoatomic gas (Bhatnagar et al. 1954) is recovered and Eq. (4.6) is expressed as the modeled BE as,

$$\frac{\partial f}{\partial t} + \boldsymbol{\xi} \cdot \nabla_{\mathrm{x}} f = -\frac{1}{\tau}\left(f - f^{eq} \right) \quad , \tag{4.12}$$

where τ corresponds to the time taken for a non-equilibrium f to approach f^{eq}.

The relaxation time τ is the basic time scale in the BE. In real gas the relaxation time scales are of the order of $10^{-8} \sim 10^{-9}$ seconds for most application range of the pressure and temperature (Hirschfelder et al. 1964). On the other hand, macroscopic properties of the fluid such as density, velocity, etc., usually possess a time-scale of about 10^{-4} seconds. The disparity in the Boltzmann and macroscopic time scales indicates that all the macroscopic quantities have converged to local equilibrium states at a very fast rate and it is practically valid to replace *f* by f^{eq} in Eqs. (4.7) - (4.10). The two disparate time scales, in fact, facilitate the derivation of the macroscopic unsteady compressible Navier-Stokes equation and its transport coefficients from the kinetic model given in Eq. (4.11) by means of a Chapman-Enskog expansion about the Knudsen number (Chapman and Cowling 1970). The Knudsen number ε is the ratio of the mean free path between two successive particle collisions and the characteristic spatial scale of the fluid system. In essence, it is a standard multi-scale expansion (Frisch et al. 1987) in which time and spatial dimensions are rescaled with ε as a small expansion parameter as follows

$$t_1 = \varepsilon t,\ t_2 = \varepsilon^2 t,\ x_1 = \varepsilon x \quad , \tag{4.13a}$$

$$\frac{\partial}{\partial t} = \varepsilon \frac{\partial}{\partial t_1} + \varepsilon^2 \frac{\partial}{\partial t_2}, \quad \frac{\partial}{\partial x} = \varepsilon \frac{\partial}{\partial x_1} \quad , \tag{4.13b}$$

and the distribution function *f* is expanded as

$$f = f^{eq} + f^{neq} = f^{(0)} + \varepsilon f^{(1)} + \varepsilon^2 f^{(2)} + \mathrm{O}\left(\varepsilon^3\right) \quad . \tag{4.14}$$

When $\varepsilon \sim \mathrm{O}(1)$ or larger, the gas in the system under consideration can no longer be considered as a fluid.

Inserting Eq. (4.13) into Eq. (4.12), balancing ε order by order, multiplying the resulting equation with $\psi_S(\xi)$ and performing subsequent integration over $d\xi^3$ in velocity space (Appendix B), the following conservation laws are deduced

$$\frac{\partial \rho}{\partial t} + \frac{\partial(\rho u_\alpha)}{\partial x_\alpha} = 0 \quad , \tag{4.15}$$

$$\frac{\partial(\rho u_\alpha)}{\partial t} + \frac{\partial(\rho u_\alpha u_\beta)}{\partial x_\beta}$$

$$= -\frac{\partial}{\partial x_\alpha}\left(\frac{2}{D_T + D_R}\rho e\right) + \frac{\partial}{\partial x_\alpha}\left\{\mu'\left(\frac{\partial u_\beta}{\partial x_\alpha} + \frac{\partial u_\alpha}{\partial x_\beta}\right)\right\} + \frac{\partial}{\partial x_\alpha}\left(\lambda' \frac{\partial u_\gamma}{\partial x_\gamma}\right), \tag{4.16}$$

$$\frac{\partial}{\partial t}\left(\rho e+\frac{1}{2}\rho \mathrm{u}^2\right)+\frac{\partial}{\partial x_\alpha}\left[\left(\rho e+\frac{2\rho e}{D_T+D_R}+\frac{1}{2}\rho \mathrm{u}^2\right)u_\alpha\right]$$

$$=\frac{\partial}{\partial x_\alpha}\left(\kappa'\frac{\partial T}{\partial x_\alpha}\right)+\frac{\partial}{\partial x_\alpha}\left\{\mu' u_\beta\left(\frac{\partial u_\beta}{\partial x_\alpha}+\frac{\partial u_\alpha}{\partial x_\beta}\right)\right\}+\frac{\partial}{\partial x_\alpha}\left(\lambda'\frac{\partial u_\gamma}{\partial x_\gamma}u_\alpha\right) \quad . \tag{4.17}$$

If the definition of pressure is given by $p=2\rho e/(D_T+D_R)$ and the gas constant (the ratio of the specific heats) is defined as $\gamma=(D_T+D_R+2)/(D_T+D_R)$, then the ideal gas equation of equation (Eq. (4)) naturally follows,

$$p=(\gamma-1)\rho e=\rho RT \quad . \tag{4.18}$$

Evidently, Eqs. (4.15) to (4.18) are the macroscopic conservation equations needed for an unsteady compressible Navier-Stokes flow with the first coefficient of viscosity, second coefficient of viscosity, and the thermal diffusivity defined as follows,

$$\mu'=(\gamma-1)\rho e\tau \quad , \tag{4.19}$$

$$\lambda'=(\gamma-1)\rho e\tau \quad , \tag{4.20}$$

$$\kappa'=\gamma(\gamma-1)\rho e\tau=\gamma\mu' \quad . \tag{4.21}$$

The thermal conductivity term in eq. (4.17) can be derived as

$$\frac{\partial}{\partial x_\alpha}\left(\kappa'\frac{\partial e}{\partial x_a}\right)=\frac{\partial}{\partial x_\alpha}\left(\gamma\mu'\frac{D_R+D_T}{2}R\frac{\partial T}{\partial x_a}\right)=\frac{\partial}{\partial x_\alpha}\left(c_p\mu'\frac{\partial T}{\partial x_a}\right) \quad . \tag{4.22}$$

Comparing this expression with the macroscopic energy conservation Eq. (4.3), it leads to $c_p\mu'=k$ and consequently a unity Prandtl number in the present formulation. A different Prandtl number could be deduced by scaling the value $(D_T+D_R)/D_T$ in Eqs. (4.9) and (4.10) or derived in an alternative way. As will be seen from the discussion given below on the correct recovery of the first coefficient of viscosity, Sutherland law has to be invoked. If the thermal conductivity were to be recovered correctly, Fourier law has to be used as a constraint also. Therefore, in principle, correct recovery of the Prandtl number could be sought from a proper recovery of the Fourier law of heat conduction in the derivation of the macroscopic Navier-Stokes equation. However, this is not the main objective of the present thesis; it will not be discussed further.

4.5 Recovery of First Coefficient of Viscosity

In Eqs. (4.16) and (4.17), the terms associated with the second viscosity, i.e., $\lambda'\left(\partial u_\gamma / \partial x_\gamma\right)$, is generally small compared to the other terms in practical flows (White 1991), therefore, it could be neglected in the following analysis. Therefore, the only viscosity coefficient that needs to be recovered is $\mu' = \mu$ (from this point on, following convention, μ is used to denote the first coefficient of viscosity). In most numerical simulations of aerodynamics and aeroacoustics based on macroscopic conservation laws, the value of μ is usually estimated from the Sutherland law. For the sake of completeness the proposed kinetic model is required to recover μ correctly, otherwise, the Reynolds number effect of unsteady flows would be incorrectly captured. The law of viscosity based on Sutherland's model of intermolecular force potential takes the following form (Ferziger and Kaper 1975),

$$\mu = \frac{5}{16\sqrt{\pi}} \frac{1}{\sigma_m^2} \frac{\sqrt{m k_B T}}{1+\frac{S}{T}} \approx \left(\frac{T}{T_{ref}} \right)^{3/2} \frac{T_{ref} + S}{T + S} \quad , \tag{4.23}$$

where S is an effective temperature, called the Sutherland constant, equal to 111K, 107K and 139K for air, nitrogen and oxygen, respectively (White 1991). The error associated with the approximation is within 2 - 4% over a temperature range of 210K - 1900K.

Physically, the relaxation phenomenon depends on the temperature. For instance, assuming a 'rigid sphere' collision, the kinetic model admits a relaxation time for particle velocity expressed as (Cercignani 1975),

$$\tau \approx \frac{5}{4}\bar{\tau} = \frac{5}{4}\frac{\bar{\lambda}}{\overline{|\xi|}} = \frac{5}{4}\frac{1}{\sqrt{2}\pi n\sigma_m^2\overline{|\xi|}} = \frac{5}{4\sqrt{2}}\frac{1}{\pi n\sigma_m^2\sqrt{\frac{8k_BT}{\pi M_n}}} \quad , \tag{4.24}$$

where $\bar{\tau}$ is the mean collision time of the particles and $\overline{|\xi|} = \sqrt{8k_BT/\pi M_n}$ is the magnitude of mean particle velocity. Substituting the relaxation time given in Eq. (4.24) into Eq.(4.19), $\mu' = \mu = (\gamma - 1)\rho e\tau = p\tau = \rho RT\tau$, the following expression can be deduced for μ,

$$\mu \approx \frac{5}{16\sqrt{\pi}}\frac{1}{\sigma_m^2}\sqrt{M_nk_BT} \quad . \tag{4.25}$$

Eq. (4.25) clearly shows that the first coefficient of viscosity has a different temperature dependence compared to the Sutherland law, Eq. (4.23). This means that real gas effects on viscosity cannot be correctly deduced from the microscopic single relaxation time model.

The phenomenon of fluid viscosity could be attributed to momentum transfer between gas particles before and after collisions. The distributions of momenta of the particles depend on the momentum of each particle when they are far separated, as well as the interactions of intermolecular potentials when two particles are in close encounter. The intermolecular potential represents the contributions of intermolecular attraction and repulsion to the potential function. According to Ferziger and Kaper (1975), from the kinetic theory point of view, single relaxation time is equivalent to the adoption of a ‘rigid sphere’ model in which the short range force potential behaves as if a Dirac-delta function with finite repulsion at the separation when two rigid particles are in contact $(r_m = \sigma_m)$. The model yields an exaggerated potential change at $r_m \approx \sigma_m$ and predicts poorly the temperature dependence of the macroscopic fluid properties. Sutherland (Ferziger and Kaper 1975) then suggests to include a weak but rapidly decaying repulsive potential, $\sim (\sigma_m / r_m)^{\nu}$, in the interaction and successfully provides a more realistic description of the dependence of the first coefficient of viscosity on temperature, such as given by Eq. (4.23). The effects of this weak potential might be more pronounced in the relaxation of a diatomic gas due to its more complicated molecular structure.

It is evident that the effects of the weak repulsive potential should be included in the present LBM if correct viscosity prediction is to be achieved. In the present formulation, a proper account of the effects is mainly carried out through the modification of the collision term in Eq. (4.12). The 'rigid sphere' gives a relaxation time τ_1 for momentum transport and this can be derived from Eq. (4.24) as

$$\tau_1 \approx \frac{5}{4}\tau_0 \propto T^{-1/2} \quad . \tag{4.26}$$

The determination of another relaxation time τ_2 for the weak potential is much more complicated because it depends on the particle velocity as well as on the physical nature of the gas under consideration. It could be argued that since the weak potential is a long range potential, its effects can be felt at a reasonably not-too-close separation and τ_2 could be postulated to be proportional to the average approach velocity of the particles, i.e.,

$$\tau_2 \propto \left|\bar{\xi}\right| \propto T^{1/2} \quad . \tag{4.27}$$

Consequently, the simplified collision operator *J* could be expressed as

$$J(f) = -\left(\frac{1}{\tau_1} + \frac{1}{\tau_2}\right)\left(f - f^{eq}\right) = -\left(\frac{1}{\tau_1\tau_2/(\tau_1+\tau_2)}\right)\left(f - f^{eq}\right) = -\frac{1}{\tau_{eff}}\left(f - f^{eq}\right) \quad , \tag{4.28}$$

for the improved BE based on Eq. (4.12) and the first coefficient of viscosity can be expressed as

$$\mu = \rho RT\tau_{eff} = \rho RT\,\frac{\tau_1\tau_2}{\tau_1+\tau_2} = \frac{5}{16\sqrt{\pi}}\,\frac{1}{\sigma_m^2}\,\frac{\sqrt{mk_BT}}{1+\dfrac{\tau_1}{\tau_2}} \quad . \tag{4.29}$$

From Eqs. (4.26) and (4.27), the temperature dependence of the ratio of the two relaxation times can be expressed as $\tau_1/\tau_2 = S_0/T$, where S_0 is a constant depending on the physical properties of the gas. Eventually, by choosing S_0 equal to *S*, Eq. (4.29) is recovered for the correct prediction of μ. If the two relaxation times τ_1 and τ_2 are known, it is straightforward to calculate the effective relaxation time τ_{eff} for Eq. (4.29) to get a correct estimate of μ. The calculated τ_{eff} can then be used to replace τ in Eq. (4.12) for the improved LBM simulation. Fig. 4.1 illustrates the difference in the variation of μ for two common diatomic gases, nitrogen and oxygen, depicted using Eqs. (4.25) and (4.29). It is evident that the single relaxation time model over predicts the values of μ for a wide range of temperature with errors ranging from 28% at high temperature to 70% at low temperature.

Theoretical analysis (Lallemand and Luo 2003) shows that the acoustic properties of a fluid can be fully resolved by a multiple-relaxation-time (MRT) model in which τ for each velocity moment can be adjusted separately. However, adopting the proposed MRT model would require complicated programming and higher computational cost. Furthermore, the proposed MRT model has different τ for each velocity moment; these relaxation times are empirically determined and could not be generalized easily for problems different from those treated in Lallemand and Luo (2003). From the above analysis, the modified SRT model (as given by Eqs. (4.12) and (4.28)) has the ability to recover the viscosity correctly after considering the weak potential force in the physical relaxation time τ . This implies that temperature dependence of μ could be recovered according to Sutherland law. In other words, viscous effect can be correctly recovered in any LBM simulations. Therefore, the improved BE is preferred over other proposed multiple relaxation time models for Eq. (4.12). Further discussion of this is given in the next chapter.

4.6 Numerical Scheme for Finite Difference Lattice Boltzmann Method

4.6.1 Lattice Models and Coefficients

Instead of tracking the evolutions of the primitive variables in the flow solutions in conventional numerical flow simulations, the method of LBM solves only the evolution of f as prescribed in Eq. (4.12) with τ replaced by τ_{eff}. This equation is first discretized in a velocity space using a finite set of velocity vectors $\{\xi_i\}$ in the context of the conservation laws (Chen and Doolen 1998) such that,

$$\frac{\partial f_i}{\partial t} = -\xi_i \cdot \nabla f_i - \frac{1}{\tau_{eff}}\left(f_i - f_i^{eq}\right) \quad , \tag{4.30}$$

where $f_i(\boldsymbol{x},t) = f(\boldsymbol{x},\xi_i,t)$ is the distribution function associated with the ι-th discrete velocity ξ_i, and f_i^{eq} is the corresponding equilibrium distribution function in the discrete velocity space. The continuous local Maxwellian f^{eq} may be rewritten up to the third order of the velocity after a Taylor expansion in u and can be expressed in the discrete velocity space as,

$$f_i^{eq} = \rho A_i\left[1 + \frac{\boldsymbol{\xi_i} \cdot \boldsymbol{u}}{\theta} + \frac{(\boldsymbol{\xi_i} \cdot \boldsymbol{u})^2}{2\theta^2} - \frac{\boldsymbol{u^2}}{2\theta} - \frac{(\boldsymbol{\xi_i} \cdot \boldsymbol{u})\boldsymbol{u^2}}{2\theta^2} + O\left(\frac{(\boldsymbol{\xi_i} \cdot \boldsymbol{u})^3}{\theta^3}\right)\right] \quad , \tag{4.31}$$

where $\theta = RT$. The weighting factors A_i are dependent on the lattice model selected to represent the discrete velocity space. They are evaluated from the constraints of local macroscopic variables, Eqs. (7) – (10), in the lattice with N discrete velocity sets, as

$$\rho = \sum_{i=1}^{N} f_i^{eq}, \quad \rho e + \frac{1}{2}\rho|\mathbf{u}|^2 = \frac{1}{\gamma - 1}\sum_{i=1}^{N}\frac{1}{2} f_i^{eq}|\boldsymbol{\xi}_\alpha|^2 \quad , \tag{4.32}$$

$$\rho\mathbf{u} = \sum_{i=1}^{N} \boldsymbol{\xi}_i f_i^{eq}, \quad \left(\rho e + p + \frac{1}{2}\rho|\mathbf{u}|^2\right)\mathbf{u} = \frac{1}{\gamma - 1}\sum_{i=1}^{N}\frac{1}{2} f_i^{eq}|\boldsymbol{\xi}_i|^2 \boldsymbol{\xi}_i \quad . \tag{4.33}$$

For the two-dimensional lattice with a diatomic gas flow considered in the present study, $D_T = 2$ and $D_R = 3$ are given (two-dimensional lattice speed is considered and the total degree of freedom should be equal to 5), so the specific heat ratio is given by $\gamma = 1.4$. Two discrete velocity sets are attempted for the lattice, namely a two-dimensional nine-velocity (D2Q9) model and a two-dimensional thirteen-velocity (D2Q13) model. Their definitions and the associated weighting factors are illustrated in Fig. 4.2. Since the Sutherland law can be correctly recovered from Eq. (4.29) with the definition of the effective relaxation time τ_{eff} given in Eq. (4.28), the viscosity can be determined from $\mu \approx \left(T/T_{ref}\right)^{3/2}\left[\left(T_{ref} + S\right)/\left(T + S\right)\right]$, once the local temperature is known. Alternatively, τ_{eff} in the present formulation can be obtained from $\tau_{eff} = \mu/\left[\left(\gamma - 1\right)\rho e\right]$.

4.6.2 Finite Difference Scheme and Time Marching

In conventional methods, Eq. (4.30) is solved by first evaluating the collision process while the streaming process is calculated at every time step. In the present study, these processes are replaced by a combination of finite difference method in which the convective derivatives of f_i on the right hand side of Eq. (4.30) are evaluated by a sixth-order finite difference scheme (Chapter 2), followed by a time advancement using a second-order Runge-Kutta scheme. This high-order spatial difference scheme provides a very low dispersive and low dissipative numerical solution to approximate the modeled BE. These efforts could minimize the numerical viscosity for the small quantity disturbances, so one-step numerical simulations with the Boltzmann model could predict the aeroacoustic problems with the solutions essentially the same as those obtained by solving the Navier-Stokes equations using DNS.

4.7 Non-Reflection Boundary Conditions for Open Boundaries

The coherence feature of the Boltzmann equation already implies different orders of conservations (mass, momentum, energy and energy flux) for the particles. Physically, if all these conservation laws were satisfied at the computational boundaries, the artificial boundaries would be non-reflecting for mass, momentum, energy and energy flux. This may give a simple non-reflecting boundary condition for the CAA problems. In the following two chapters, a simple zero and first order continuity conditions, and buffer zone technique are tested for different aeroacoustic problems using LBM. For the DNS method solving the Navier-Stokes equations, it has been explained in Chapter 2 that the characteristic-based boundary conditions (NSCBC), the absorbing technique (ABC) and the perfectly matched layer method (PML) are suitable nonreflecting boundary methods for aeroacoustic computations. Sometimes, the conservation element (CE) boundary method could also be used. It should be noted that most of these DNS nonreflecting boundary methods are derived from the Euler equations and maybe not stable for shear layers, where the second order partial derivatives inside the Navier-Stokes equations would dominate the flux terms. These linear analyses could not deal with the viscous terms. Using a simple absorbing region, the computations could be made stable for shear flows. However, a large number of nonphysical grids have to be added inside the buffer; therefore, it would cause the computational cost to increase. On the other hand, as it has been mentioned before, the simple form of the Boltzmann equation already implied viscosity for the flow (Eq. (4.29)); only first order derivatives appear in the convection terms for the particles. This allows the use of a very simple linear analysis to deduce the proper nonreflecting boundary conditions. If a suitable nonreflecting boundary technique with no buffer region is found for one-step CAA using LBM, the computational domain could be reduced to a much smaller size and the associated reduction in computational cost of the LBM makes it a very attractive alternative to the DNS.

Three simple methods were used in the following cases. The first one is zero-order continuity of the particle velocity distribution function. For the solutions f_i, $i \in \{1,2,...,N-1,N\}$, where *i=1* and *i=N* are the boundary points. In the computations, after using the 6th-order finite difference scheme and second-order time marching, the whole solutions for new time-step could be valued. After that, the boundary solutions f_1 and f_N would be corrected by nearby inner points values, thus $f_1 = f_2$ and $f_N = f_{N-1}$. If there were no pulses passing through the boundaries, this boundary condition is proved to be stable for the improved LBM (in §5.1). There are no spurious waves appeared near the boundaries.

The second method is using the first-order continuity. Similar to the first method, for the boundary points, the gradients normal to the boundary were set equal to the nearby inner value, such as $(\partial f / \partial n)_1 = (\partial f / \partial n)_2$ and $(\partial f / \partial n)_N = (\partial f / \partial n)_{N-1}$, where *n* is along the normal direction of the boundaries. This technique is applied to the upper and lower boundaries of the plane pulse interacting with a zero circulation vortex case treated in chapter 6 where 1-D continuous waves are transmitted through boundaries. Therefore, the upper and lower boundaries should keep the wave front normal to the boundaries at all time. Simultaneously, this technique should be non-reflecting for the disturbances passing through the boundaries. It was shown that this simple first order technique could be extended as an appropriate non-reflecting boundary condition for the improved LBM.

The third method is using the buffer technique. Similar to the absorbing BC for Navier-Stokes equations, this absorbing is adopted to the particle distribution function. A damping term is added into the governing equation, thus the governing equation is revised to:

$$\frac{\partial f}{\partial t}+\boldsymbol{\xi}\cdot\nabla_{\mathbf{x}} f+\sigma\left(f-\bar{f}\right)=-\frac{1}{\tau}\left(f-f^{eq}\right) \quad . \tag{4.34}$$

where $\bar{f}$ is the particle distribution value when the flow quantities are in homogenous mean state, σ is the absorption coefficient that varies smoothly from zero at the edge of the buffer to a constant value near the boundaries. The buffer is used to absorb the disturbances from the inner field and when close to boundaries, the solutions are forced to become equal to the mean state solutions so there are no reflections from boundaries. This method is applied in §5.3 and scattering cases. In these cases, continuous 1-D waves were excited inside domains, these buffer regions lie in the opposite direction of the waves. All disturbances energy would be absorbed before they touch the boundaries. Otherwise, if there are any small reflections, the continuous waves would generate more and more spurious waves inside and could drive the computation to attain a wrong state. This buffer technique provides good results for these cases.

4.8 Advantages of One-Step CAA Using the Improved LBM

The simple structure of the improved LBM code is most suitable for parallel computation, which means a significant saving in computational time. Because of the complexity of the Navier-Stokes equations, the code is very complicated and parallel computation could not be fully made used of. Therefore, computational time becomes an important issue in one-step CAA using the DNS method. Furthermore, the structure of the improved LBM code is quite simple and is about 400 lines, whereas the DNS code for the solution of the Navier-Stokes equations will involve at least 1400 lines.

The high-order solutions of the Boltzmann equation could also help the understanding of the physics of particle transport. As mentioned in the beginning of this chapter, the Stokes hypothesis and the Fourier law have to be specified in the solution of the Navier-Stokes equations if the high-order transport, such as viscous stress and heat flux, were to be determined. Consequently, the Navier-Stokes equations cannot be used to explore the mechanism of these high-order transports. On the other hand, the Boltzmann equation studies particles, so these high-order transports can be evaluated directly from the conservation laws. An example is the recovery of the first coefficient of viscosity. A two-relaxation time model is postulated so that Sutherland law can be recovered correctly. A following work for LBM is the recovery of the Prandtl number, which is related to energy flux. This could be achieved by stipulating that the analysis should lead to the recovery of the Fourier law of conduction.

4.9 Summary

In this chapter, a lattice Boltzmann method is proposed for computational aeroacoustics. The basic Boltzmann equation is the governing equation for a single particle velocity distribution function by translation and collision motions (§4.2). The macroscale fluid properties such as density, momentum, energy and energy flux can be assumed as different orders integrations of this function on the whole velocity space (§4.3). A new description on the internal energy is suggested in §4.3 after considering the rotational energy of particles (especially for the diatomic gases such as air). Using a multiscale “Chapman-Enskog” expansion about the Knudsen number, the full set of unsteady compressible Navier-Stokes equations are recovered (§4.4). Following the suggestion of §4.3, the gas equation of state is recovered correctly with the gas specific heat ratio for diatomic gases given by 1.4. In the process of deriving the Navier-Stokes equations, the viscosity of the fluid is shown to be related to the collision time $\mu = (\gamma - 1)\rho e \tau$. If τ in this equation is assumed to be given by the rigid sphere model of collision, the viscosity would have a wrong dependence on temperature (Eq.(4.25)), the resultant error can be as large as 70% (Fig. 4.1). By considering an additional “weak force” for the collision process (§4.5), the relation between viscosity and temperature can be shown to have the same form as Sutherland law. It can be shown that in numerical simulation using the improved BE, the viscosity is recovered correctly and so is the Reynolds number. The detailed numerical scheme used to solve the improved LBM is described in §4.6. Some benchmark aeroacoustic problems used to validate this LBM are discussed in Chapter 6 and Chapter 7. Finally, §4.7 lists some advantages of the improved LBM scheme. Comparing with the DNS method, the improved LBM code has a very simple structure and is more efficient on parallel machine; therefore, the computational time can be deduced.

However, the disadvantages of LBM can not be ignored. Which would be described in following chapter, the major disadvantage is that the time step for LBM is very small, compared with DNS computations. According to the LBM stability criterion of Tsutahara et al. (2002), $\Delta t < \tau/2$, the time step is proportional to the collision time. If realized Eq. (4-19), the collision time is proportional to the viscosity of fluid, so, if the viscosity is smaller, the time step is smaller. This would result that the LBM time-step is related to the Reynolds number after the normalization. For a higher Reynolds number flow, a smaller time-step should be used. As it would be shown in the next chapter, for the same problem, LBM used a much smaller time-step than DNS.

Appendix A: Internal Energy and Temperature

The internal energy e is defined by the following relation,

$$\rho e + \frac{1}{2}\rho|\boldsymbol{u}|^2 = \frac{D_T + D_R}{D_T}\int \frac{1}{2} f\,|\xi|^2\, d\xi \quad . \tag{A.1}$$

In general, the particle distribution function f can be decomposed into an equilibrium part and a non-equilibrium part, i.e., $f = f^{eq} + f^{neq}$. The non-equilibrium part f^{neq} is required to satisfied the nullity requirement for moments of different velocity orders, i.e.,

$$\int f^{neq} d\boldsymbol{\xi} = \int f^{neq}\boldsymbol{\xi} d\boldsymbol{\xi} = \int f^{neq}\boldsymbol{\xi}^2 d\boldsymbol{\xi} = 0 \quad . \tag{A.2}$$

Therefore, making use of Eq. (11) for f^{eq}, Eq. (A.1) can be expressed as:

$$\rho e + \frac{1}{2}\rho|\boldsymbol{u}|^2 = \frac{D_T + D_R}{D_T}\int \frac{1}{2} f^{eq}|\xi|^2 d\xi = \frac{D_T + D_R}{D_T}\int \frac{1}{2}\frac{\rho}{(2\pi RT)^{D_T/2}} \exp\left[-\frac{|\boldsymbol{\xi}\text{-}\boldsymbol{u}|^2}{2RT}\right]|\xi|^2 d\xi \tag{A.3}$$

The total number of degrees of freedom for diatomic gas motions is always $D_T + D_R$ = 5 (where $D_T = 3$ and $D_R = 2$). Therefore, the right hand side of Eq. (A.3) is a function of temperature alone. The sole temperature effect on e is realized in the redistribution of the particle momentum due to particle collision and should be independent of the 'mean' flow velocity carrying the particles (Tsutahara et al 2002). Therefore, e should be the same irrespective of whether $\boldsymbol{u} = 0$. Integration of Eq. (A-3) in 3-D simulations (D = 3) leads to

$$e = \frac{D_T + D_R}{3}\int_0^\infty 4\pi r^2 \frac{1}{2}\frac{1}{(2\pi RT)^{3/2}} \exp\left(-\frac{|\mathbf{r}|^2}{2RT}\right)|\mathbf{r}|^2 d\mathbf{r}$$

$$= \frac{D_T + D_R}{3}\left(\frac{3}{2}RT\right) = \frac{D_T + D_R}{2}RT \quad , \tag{A.4}$$

where $\boldsymbol{r} = \boldsymbol{\xi} - \boldsymbol{u}$.

In a 2-D simulation, only two planar translational motions are allowed, thus giving $D_T = 2$. If similar arguments for the temperature dependence in the 3-D case is applied, then, with $\boldsymbol{r} = \boldsymbol{\xi} - \boldsymbol{u}$ in 2-D,

$$e = \frac{D_T + D_R}{2} \int_0^\infty 2\pi r \frac{1}{2} \frac{\rho}{(2\pi RT)} \exp\left(-\frac{|\boldsymbol{r}|^2}{2RT} \right) |\boldsymbol{r}|^2 d\boldsymbol{r} = \frac{D_T + D_R}{2} RT \quad . \tag{A.5}$$

Evidently the definition of e in the present LBM holds for both 2- and 3-D flows. It is interesting to note that the integration results of Eqs. (A.3) and (A.5) perfectly match the classical equipartition theorem of the kinetic theory of gases, which states that, for a polyatomic gas, each degree of freedom equally contributes $RT/2$ to the total amount of internal energy.

Appendix B: Derivation of Navier-Stokes Equations

The Chapman-Enskog expansion is a multi-scale expansion in which time and spatial dimensions are rescaled with a very small parameter ε (Knudsen number) as follows:

$$t_1 = \varepsilon t,\ t_2 = \varepsilon^2 t,\ x_1 = \varepsilon x \quad , \tag{B.1a}$$

$$\frac{\partial}{\partial t} = \varepsilon \frac{\partial}{\partial t_1} + \varepsilon^2 \frac{\partial}{\partial t_2}, \quad \frac{\partial}{\partial x} = \varepsilon \frac{\partial}{\partial x_1} \quad , \tag{B.1b}$$

and the distribution function *f* is expanded as

$$f = f^{eq} + f^{neq} = f^{(0)} + \varepsilon f^{(1)} + \varepsilon^2 f^{(2)} + \mathrm{O}\left(\varepsilon^3\right) \quad . \tag{B.2}$$

Here, the Knudsen number ε is defined as the ratio of the mean free path between two successive particle collisions and the characteristic spatial scale of the fluid system. Substituting Eq. (B.2) into the modeled Boltzmann equation (4.12) gives

$$\varepsilon \frac{\partial\left(f^{(0)} + \varepsilon f^{(1)} + \varepsilon^2 f^{(2)}\right)}{\partial t_1} + \varepsilon^2 \frac{\partial\left(f^{(0)} + \varepsilon f^{(1)} + \varepsilon^2 f^{(2)}\right)}{\partial t_2}$$

$$+ \varepsilon \boldsymbol{\xi} \cdot \nabla\left(f^{(0)} + \varepsilon f^{(1)} + \varepsilon^2 f^{(2)}\right) = -\frac{\varepsilon f^{(1)} + \varepsilon^2 f^{(2)}}{\tau} \quad . \tag{B.3}$$

Collecting terms with the same order of ε, the following results up to $f^{(1)}$ are obtained,

$$\frac{\partial f^{(0)}}{\partial t_1} + \boldsymbol{\xi} \cdot \nabla f^{(0)} = -\frac{f^{(1)}}{\tau} \quad , \tag{B.4a}$$

$$\frac{\partial f^{(1)}}{\partial t_1} + \boldsymbol{\xi} \cdot \nabla f^{(1)} + \frac{\partial f^{(0)}}{\partial t_2} = -\frac{f^{(2)}}{\tau} \quad . \tag{B.4a}$$

(i) The mass conservation equation

Integrating equation (B.4a) over the particle velocity space, and realizing that the integration of the non-equilibrium term $\int f^{(1)} d\xi$ should be zero, this would give the mass conservation law as

$$\frac{\partial}{\partial t_1}\left(\int f^{(0)} d\xi\right)+\frac{\partial}{\partial x_\alpha}\left(\int \xi_\alpha f^{(0)} d\xi\right)=0 \quad , \tag{B.5}$$

where ξ_α is the particle speed along α-axis. It should be noted that, for simple expressions, the second term represents the summation along all axes of the coordinate; in the following, if not specified, this would not be noted again. Using the macro-scale definition of density and momentum Eqs. (4.7) and (4.8) gives,

$$\frac{\partial \rho}{\partial t_1}+\frac{\partial(\rho u_\alpha)}{\partial x_\alpha}=0 \quad , \tag{B.6}$$

If Eq. (B.4b) is also integrated over the particle velocity space, the following is obtained,

$$\frac{\partial \rho}{\partial t_2}+\frac{\partial\left(\int f^1 d\xi\right)}{\partial t_1}+(-\tau)\frac{\partial}{\partial x_\alpha}\left[\frac{\partial\left(\int f^0 \xi_\alpha d\xi\right)}{\partial t_1}+\frac{\partial\left(\int f^0 \xi_\alpha^2 d\xi\right)}{\partial x_\alpha}+\frac{\partial\left(\int f^0 \xi_\alpha \xi_\beta d\xi\right)}{\partial x_\beta}\right]=0 \quad , \tag{B.7}$$

with $\beta \neq \alpha$ replacing all other terms that do not align with the α-axis. The second term is zero because it is the integration of a non-equilibrium function. The term inside the square bracket is also zero because they are equivalent to the integration of Eq. (B.4a) times ξ_α. Thus the result is obtained,

$$\frac{\partial \rho}{\partial t_2}=0, \tag{B.8}$$

Combine Eq. (B.6) and Eq. (B.8) together, the mass conservation equation is obtained as

$$\frac{\partial \rho}{\partial t}+\frac{\partial(\rho u_\alpha)}{\partial x_\alpha}=0 \quad . \tag{B.9}$$

(ii) The momentum conservation equation

Multiplying both sides of Eq. (B.4a) and Eq. (B.4b) by ξ_α and integrating over the velocity space leads to

$$\frac{\partial(\rho u_\alpha)}{\partial t_1}+\frac{\partial}{\partial x_\alpha}\left(\int f\xi_\alpha^2 d\xi\right)+\frac{\partial}{\partial x_\beta}\left(\int f\xi_\alpha\xi_\beta d\xi\right)=0 \quad , \tag{B.10}$$

$$\frac{\partial(\rho u_\alpha)}{\partial t_2}+\frac{\partial}{\partial t_1}\left(\int f^1\xi_\alpha d\xi\right)+\frac{\partial}{\partial x_\alpha}\left(\int f^1\xi_\alpha^2 d\xi\right)+\frac{\partial}{\partial x_\beta}\left(\int f^1\xi_\alpha\xi_\beta d\xi\right)=0 \quad . \tag{B.11}$$

The second term of Eq. (B.11) is zero because it integrates the non-equilibrium function over the whole velocity space. Substituting Eq. (B.4a) into Eq. (B.11) gives rise to

$$\begin{aligned}\frac{\partial(\rho u_\alpha)}{\partial t_2}&=\frac{\partial}{\partial x_\alpha}\left[\tau\frac{\partial}{\partial t_1}\left(\int f^0\xi_\alpha^2 d\xi\right)+\tau\frac{\partial}{\partial x_\alpha}\left(\int f^0\xi_\alpha^3 d\xi\right)+\tau\frac{\partial}{\partial x_\beta}\left(\int f^0\xi_\alpha^2\xi_\beta d\xi\right)\right]\\&+\frac{\partial}{\partial x_\beta}\left[\tau\frac{\partial}{\partial t_1}\left(\int f^0\xi_\alpha^2 d\xi\right)+\tau\frac{\partial}{\partial x_\alpha}\left(\int f^0\xi_\alpha^2\xi_\beta d\xi\right)+\tau\frac{\partial}{\partial x_\beta}\left(\int f^0\xi_\alpha\xi_\beta d\xi\right)\right] \quad .\end{aligned} \tag{B.12}$$

Compare the time scale t_1 and t_2, leads to the realization that $\partial/\partial t_1 \approx \varepsilon\,\partial/\partial t_2$. Substituting this relation into Eq. (B.12) and resetting all ε order terms to zero (because a very small ε is assumed here), the following result is obtained,

$$\begin{aligned}\frac{\partial(\rho u_\alpha)}{\partial t_2}&=\frac{\partial}{\partial x_\alpha}\left[\tau\frac{\partial}{\partial x_\alpha}\left(\int f^0\xi_\alpha^3 d\xi\right)+\tau\frac{\partial}{\partial x_\beta}\left(\int f^0\xi_\alpha^2\xi_\beta d\xi\right)\right]\\&\qquad+\frac{\partial}{\partial x_\beta}\left[\tau\frac{\partial}{\partial x_\alpha}\left(\int f^0\xi_\alpha^2\xi_\beta d\xi\right)+\tau\frac{\partial}{\partial x_\beta}\left(\int f^0\xi_\alpha\xi_\beta^2 d\xi\right)\right] \quad .\end{aligned} \tag{B.13}$$

In order to simplify Eqs. (B.10) and (B.13) the integrals in Eq. (B.13) should be evaluated as functions of macroscopic fluid quantities first; these integrals are: $\int f^0\xi_\alpha^2 d\xi$, $\int f^0\xi_\alpha\xi_\beta d\xi$, $\int f^0\xi_\alpha^3 d\xi$ and $\int f^0\xi_\alpha^2\xi_\beta d\xi$.

To generalize the derivation, a 3-D approach is adopted. A Cartesian coordinate (*x*, *y*, *z*) is defined with (*u*, *v*, *w*) taken to be the macro-scale fluid velocity along the *x*-

axis, the *y*-axis and the *z*-axis, respectively. The conservation laws for density and momentum can be expressed as

$$\rho = \int f^0 d\xi \quad , \tag{B.14}$$

$$\rho u = \int f^0 \xi_x d\xi \Rightarrow \int f^0 (\xi_x - u) d\xi = 0 \quad , \tag{B.15}$$

where $\xi_x - u$ is defined as the *hot speed* of the particles along the *x*-axis. For the *y*-axis and the *z*-axis, similar formulations can be made but would not be repeated here. Because the equilibrium function $f^0 = \frac{\rho}{(2\pi RT)^{3/2}} \exp\left(-\frac{|\xi - \boldsymbol{u}|^2}{2RT}\right)$ is symmetrically distributed around the hot speed, it can be shown that,

$$\int f^0 (\xi_x - u)(\xi_y - v) d\xi = 0 \quad ,$$

$$\Rightarrow \int f^0 \xi_x \xi_y d\xi - v \int f^0 \xi_x d\xi - u \int f^0 \xi_y d\xi + uv \int f^0 d\xi = 0 \quad ,$$

$$\Rightarrow \int f^0 \xi_x \xi_y d\xi = \rho uv \quad . \tag{B.16}$$

Similarly, it can be shown that $\int f^0 \xi_x \xi_z d\xi = \rho uw$ and $\int f^0 \xi_y \xi_z d\xi = \rho vw$. Realizing that the internal energy should be only related to the *hot speed* of the particles, the internal energy conservation could be expressed as,

$$\rho e = \frac{D_T + D_R}{D_T} \int \frac{1}{2} f^0 \left[(\xi_x - u)^2 + (\xi_y - v)^2 + (\xi_z - w)^2 \right] d\xi \quad , \tag{B.17}$$

where $D_T = 3$ and $D_R = 2$ are defined for the diatomic gases. Thus, Eq. (B.17) can also be expressed as,

$$(\gamma - 1)\rho e = \frac{1}{3} \int f^0 \left[(\xi_x - u)^2 + (\xi_y - v)^2 + (\xi_z - w)^2 \right] d\xi \quad , \tag{B.18}$$

where γ=1.4. On the other hand, since the internal energy is also equally distributed along the *x*-, *y*- and *z*-directions, it can be easily shown that,

$$\int f^0 (\xi_x - u)^2 d\xi = \frac{1}{3} \int f^0 \left[(\xi_x - u)^2 + (\xi_y - v)^2 + (\xi_z - w)^2 \right] d\xi = (\gamma - 1)\rho e \quad ,$$

$$\Rightarrow \int f^0 \xi_x^2 d\xi = (\gamma - 1)\rho e + \rho u^2 \quad . \tag{B.19}$$

Since the equilibrium function is symmetrically distributed for the hot speed, it leads to

$$\int f^0 (\xi_x - u)^2 (\xi_y - v) d\xi = 0 \quad , \tag{B.20}$$

$$\int f^0 (\xi_x - u)^3 d\xi = 0 \quad , \tag{B.21}$$

Similar expressions could also be derived but not be repeated here. Eqs. (B.20) and (B.21) would give the following useful expressions,

$$\int f^0 \xi_x^2 \xi_y d\xi = v(\Phi + \rho u^2) \quad , \tag{B.22}$$

$$\int f^0 \xi_x^3 d\xi = u(3\Phi + \rho u^2) \quad , \tag{B.23}$$

where $\Phi = (\gamma - 1)\rho e$ is used to simplify the writings. Substituting the expressions (B.16), (B.19), (B.22) and (B.23) into Eqs. (B.10) and (B.13), the following results are obtained

$$\frac{\partial(\rho u)}{\partial t_1} + \frac{\partial(\Phi + \rho u^2)}{\partial x} + \frac{\partial(\rho uv)}{\partial y} + \frac{\partial(\rho uw)}{\partial z} = 0 \quad , \tag{B.24}$$

$$\begin{aligned}\frac{\partial(\rho u)}{\partial t_2} = & \frac{\partial}{\partial x}\left\{\tau \frac{\partial}{\partial x}\left[u(3\Phi + \rho u^2)\right] + \tau \frac{\partial}{\partial y}\left[v(\Phi + \rho u^2)\right] + \frac{\partial}{\partial z}\left[w(\Phi + \rho u^2)\right]\right\} \\ & + \frac{\partial}{\partial y}\left\{\tau \frac{\partial}{\partial x}\left[v(\Phi + \rho u^2)\right] + \tau \frac{\partial}{\partial y}\left[u(\Phi + \rho v^2)\right] + \tau \frac{\partial}{\partial z}(\rho uvw)\right\} \\ & + \frac{\partial}{\partial z}\left\{\tau \frac{\partial}{\partial x}\left[w(\Phi + \rho u^2)\right] + \tau \frac{\partial}{\partial y}(\rho uvw) + \tau \frac{\partial}{\partial z}\left[u(\Phi + \rho u^2)\right]\right\}\end{aligned} \tag{B.25}$$

It should be noted here, in the expansion of Eq. (4.31) for Eq. (4.11), a condition has been assumed that ***u*** should be small, otherwise, if the macro-speed ***u*** is large, Eq. (4.31) can not be used to replace the physical formulation of Eq. (4.11). Therefore the expression $\Phi = (\gamma - 1)\rho e >> \rho u^2$ could be written. Then it follows that

$$3\Phi + \rho u^2 \approx 3\Phi, \;\; \Phi + \rho u^2 \approx \Phi \quad . \tag{B.26}$$

Substituting these relations into the right hand side of Eq. (B.25) and also eliminating the other terms, it gives

$$\frac{\partial(\rho u)}{\partial t_2} = \frac{\partial}{\partial x}\left[\tau\frac{\partial}{\partial x}(u3\Phi) + \tau\frac{\partial}{\partial y}(v\Phi) + \frac{\partial}{\partial z}(w\Phi)\right] + \frac{\partial}{\partial y}\left[\tau\frac{\partial}{\partial x}(v\Phi) + \tau\frac{\partial}{\partial y}(u\Phi)\right]$$
$$+\frac{\partial}{\partial z}\left[\tau\frac{\partial}{\partial x}(w\Phi) + \tau\frac{\partial}{\partial z}(u\Phi)\right] \quad . \qquad (B.27)$$

For each term inside the squared brackets on the right hand side of Eq. (B.27) such as $\partial(u3\Phi)/\partial x$, it can be calculated as follow

$$\frac{\partial}{\partial x}(u3\Phi) = 3u\frac{\partial \Phi}{\partial x} + 3\Phi\frac{\partial u}{\partial x} \quad . \qquad (B.27a)$$

If $\Phi = (\gamma - 1)\rho e = \rho c^2/\gamma$ is substituted into Eq. (B.28), the following result is obtained,

$$\frac{\partial}{\partial x}(u3\Phi) = 3u\frac{\partial}{\partial x}\left(\rho c^2/\gamma\right) + 3\Phi\frac{\partial u}{\partial x} = (6u\rho c/\gamma)\frac{\partial c}{\partial x} + 3\Phi\frac{\partial u}{\partial x} = 3\Phi\left[(2u/c)\frac{\partial c}{\partial x} + \frac{\partial u}{\partial x}\right] \quad , \qquad (B.27b)$$

Obviously, the first term inside the squared brackets in Eq. (B.27b) can be neglected when compared with the second term. Thus, Eq. (B.27b) is reduced to

$$\frac{\partial(u3\Phi)}{\partial x} \approx 3\Phi\frac{\partial u}{\partial x} \quad . \qquad (B.28)$$

Using the same consideration as Eq. (B.28) to simplify Eq. (B.27) leads to

$$\frac{\partial(\rho u)}{\partial t_2} = \left(3\Phi\tau\frac{\partial u}{\partial x} + \Phi\tau\frac{\partial v}{\partial y} + \Phi\tau\frac{\partial w}{\partial y}\right) + \frac{\partial}{\partial y}\left(\Phi\tau\frac{\partial v}{\partial x} + \Phi\tau\frac{\partial u}{\partial y}\right) + \frac{\partial}{\partial z}\left(\Phi\tau\frac{\partial w}{\partial x} + \Phi\tau\frac{\partial u}{\partial z}\right)$$

$$= \frac{\partial}{\partial x}\left[\Phi\tau\left(2\frac{\partial u}{\partial x} + \Lambda\right)\right] + \frac{\partial}{\partial y}\left[\Phi\tau\left(\frac{\partial v}{\partial x} + \frac{\partial u}{\partial y}\right)\right] + \frac{\partial}{\partial z}\left[\Phi\tau\left(\frac{\partial w}{\partial x} + \frac{\partial u}{\partial z}\right)\right] \quad , \qquad (B.29)$$

where $\Lambda = \frac{\partial u}{\partial x} + \frac{\partial v}{\partial y} + \frac{\partial w}{\partial z}$ is the fractional rate of change of the volume of a material element, or called the local rate of expansion or rate of dilatation.

Rearranging Eq. (B.29) and combining with Eq. (B.24), it would give the momentum equation along the *x*-axis as

$$\frac{\partial(\rho u)}{\partial t}+\frac{\partial\left(\Phi+\rho u^{2}\right)}{\partial x}+\frac{\partial(\rho uv)}{\partial y}+\frac{\partial(\rho uw)}{\partial z}$$

$$=\frac{\partial}{\partial x}\left(2\mu'\frac{\partial u}{\partial x}\right)+\frac{\partial}{\partial y}\left[\mu'\left(\frac{\partial v}{\partial x}+\frac{\partial u}{\partial y}\right)\right]+\frac{\partial}{\partial z}\left[\mu'\left(\frac{\partial w}{\partial x}+\frac{\partial u}{\partial z}\right)\right]+\frac{\partial}{\partial x}\left(\lambda'\Lambda\right) \quad , \tag{B.30}$$

where the first coefficient of viscosity inside this equation is defined as $\mu=\mu'=\Phi\,\tau=(\gamma-1)\rho e\,\tau$, the second coefficient of viscosity is $\lambda=\lambda'=\Phi\,\tau=(\gamma-1)\rho e\,\tau$. It is not difficult to derive similar expressions for the *y*-axis and the *z*-axis. Together, these expressions constitute the *x*-, *y*- and *z*-component momentum equation of the Navier-Stokes equations. At the same time, the thermodynamic pressure *p* is given by $p=\Phi=(\gamma-1)\rho e=\rho RT$, which is the correct gas equation of state of a perfect gas.

(iii) The energy conservation equation

Multiplying both sides of Eq. (B.4a) by $\frac{1}{2}|\boldsymbol{\xi}|^{2}=\frac{1}{2}\left(\xi_x^2+\xi_y^2+\xi_z^2\right)$ and integrating over the whole velocity space gives rise to

$$\frac{\partial}{\partial t_1}\left(\frac{3}{2}\Phi+\frac{1}{2}\rho|\boldsymbol{u}|^2\right)+\frac{\partial}{\partial x}\left[\left(\frac{5}{2}\Phi+\frac{1}{2}\rho|\boldsymbol{u}|^2\right)u\right]+\frac{\partial}{\partial y}\left[\left(\frac{5}{2}\Phi+\frac{1}{2}\rho|\boldsymbol{u}|^2\right)v\right]+\frac{\partial}{\partial z}\left[\left(\frac{5}{2}\Phi+\frac{1}{2}\rho|\boldsymbol{u}|^2\right)w\right]=0 \quad . \tag{B.31}$$

In this derivation, higher order terms have been neglected. The first term on the left side of Eq. (B.31) can be expressed as $\frac{1}{2}\int f^{0}|\xi|^{2}d\xi=\frac{3}{2}\Phi+\frac{1}{2}\rho|\boldsymbol{u}|^{2}$. In the present formulation, two rotational degrees of freedom are assumed. They would contribute to the fluid kinetic energy but would not appear explicitly as transport and collision terms in the Boltzmann equation. Each degree of freedom would have an energy contribution of $\frac{1}{2}\Phi$, thus the kinetic energy of the fluid should be governed by,

$$\frac{\partial}{\partial t_1}\left(E_k\right)+\frac{\partial}{\partial x}\left[\left(E_k+\Phi\right)u\right]+\frac{\partial}{\partial y}\left[\left(E_k+\Phi\right)v\right]+\frac{\partial}{\partial z}\left[\left(E_k+\Phi\right)w\right]=0 \quad , \qquad \text{(B.32)}$$

where $E_k=\frac{5}{2}\Phi+\frac{1}{2}\rho|\boldsymbol{u}|^2=\rho e+\frac{1}{2}\rho|\boldsymbol{u}|^2$ is just the definition of kinetic energy for the fluid element.

Similarly, multiplying both sides of Eq. (B.4b) by $\frac{1}{2}|\xi|^2=\frac{1}{2}\left(\xi_x^2+\xi_y^2+\xi_z^2\right)$ and integrating over the whole velocity space leads to

$$\begin{aligned}\frac{\partial}{\partial t_2}\left(E_k\right)=\tau\frac{\partial}{\partial x}&\left[\frac{\partial}{\partial x}\left(\frac{1}{2}\int f^0|\xi|^2\xi_x^2 d\xi\right)+\frac{\partial}{\partial y}\left(\frac{1}{2}\int f^0|\xi|^2\xi_x\xi_y d\xi\right)+\frac{\partial}{\partial z}\left(\frac{1}{2}\int f^0|\xi|^2\xi_x\xi_z d\xi\right)\right]\\ +\tau\frac{\partial}{\partial y}&\left[\frac{\partial}{\partial x}\left(\frac{1}{2}\int f^0|\xi|^2\xi_x\xi_y d\xi\right)+\frac{\partial}{\partial y}\left(\frac{1}{2}\int f^0|\xi|^2\xi_y^2 d\xi\right)+\frac{\partial}{\partial z}\left(\frac{1}{2}\int f^0|\xi|^2\xi_y\xi_z d\xi\right)\right]\\ +\tau\frac{\partial}{\partial z}&\left[\frac{\partial}{\partial x}\left(\frac{1}{2}\int f^0|\xi|^2\xi_x\xi_z d\xi\right)+\frac{\partial}{\partial y}\left(\frac{1}{2}\int f^0|\xi|^2\xi_y\xi_z d\xi\right)+\frac{\partial}{\partial z}\left(\frac{1}{2}\int f^0|\xi|^2\xi_z^2 d\xi\right)\right]\end{aligned} \quad , \qquad \text{(B.33)}$$

Since $\int\frac{1}{2}f^0|\xi|^2 d\boldsymbol{\xi}=(\gamma-1)E_k$, the energy flux terms on the right hand side, such as $\int f^0|\xi|^2\xi_x\xi_y d\boldsymbol{\xi}$ could be written as $\int(\gamma-1)E_k\xi_x\xi_y d\xi$, which can be eventually simplified as $(\gamma-1)E_k uv$. Thus Eq. (B.33) can be simplified as,

$$\begin{aligned}\frac{\partial}{\partial t_2}\left(E_k\right)=\tau(\gamma-1)\frac{\partial}{\partial x}&\left[\frac{\partial}{\partial x}\left(\int E_k\xi_x^2 d\xi\right)+\frac{\partial}{\partial y}\left(E_k uv\right)+\frac{\partial}{\partial z}\left(E_k uw\right)\right]\\ +\tau(\gamma-1)\frac{\partial}{\partial y}&\left[\frac{\partial}{\partial x}\left(E_k uv\right)+\frac{\partial}{\partial y}\left(\int E_k\xi_y^2 d\xi\right)+\frac{\partial}{\partial z}\left(E_k vw\right)\right]\\ +\tau(\gamma-1)\frac{\partial}{\partial z}&\left[\frac{\partial}{\partial x}\left(E_k uw\right)+\frac{\partial}{\partial y}\left(E_k vw\right)+\frac{\partial}{\partial z}\left(\int E_k\xi_z^2 d\xi\right)\right]\end{aligned} \quad , \qquad \text{(B.34)}$$

Since the lowest order integration of f^0 gives $\int f^0 d\xi=\rho$, the first order integration yields $\int f^0\xi_x d\boldsymbol{\xi}=\rho u$, the second order integration gives $\int f^0\xi_x^2 d\boldsymbol{\xi}=u(\rho u)+\Phi$, and the third order integration leads to $\int f^0\xi_x^3 d\boldsymbol{\xi}=u\left(\Phi+\rho u^2\right)+2\Phi u$, then the fourth order integration can be defined as $\int f^0 \xi_x^4 d\xi = u^2 \int f^0 \xi_x^2 d\xi + W = u^2\left(\Phi + \rho u^2\right) + W$. If Φ is used to represent the second order energy from the particle point of view, then *W* is the forth order energy from the particle point of view. Checking the dimensions of this formulation leads to *W* having the same dimension as ρe^2. This is a very important parameter that could relate to the heat flux within energy conservation.

From the forth order integration expression, it can be shown that $\int E_k \xi_x^2 d|\xi| = u^2 E_k + W$. Substituting this into Eq. (B.34) yields

$$
\begin{aligned}
\frac{\partial}{\partial t_2}(E_k) = {} & \frac{\partial}{\partial x}\left[\tau(\gamma-1)\frac{\partial W}{\partial x}\right] + \frac{\partial}{\partial y}\left[\tau(\gamma-1)\frac{\partial W}{\partial y}\right] + \frac{\partial}{\partial x}\left[\tau(\gamma-1)\frac{\partial W}{\partial z}\right] \\
& + \frac{\partial}{\partial x}\left[\tau(\gamma-1)\frac{\partial}{\partial x}\left(E_k u^2\right) + \tau(\gamma-1)\frac{\partial}{\partial y}\left(E_k uv\right) + \tau(\gamma-1)\frac{\partial}{\partial z}\left(E_k uw\right)\right] \\
& + \frac{\partial}{\partial y}\left[\tau(\gamma-1)\frac{\partial}{\partial x}\left(E_k uv\right) + \tau(\gamma-1)\frac{\partial}{\partial y}\left(E_k v^2\right) + \tau(\gamma-1)\frac{\partial}{\partial z}\left(E_k vw\right)\right] \\
& + \frac{\partial}{\partial z}\left[\tau(\gamma-1)\frac{\partial}{\partial x}\left(E_k uw\right) + \tau(\gamma-1)\frac{\partial}{\partial y}\left(E_k vw\right) + \tau(\gamma-1)\frac{\partial}{\partial z}\left(E_k w^2\right)\right]
\end{aligned}
$$

$$
\begin{aligned}
= {} & \frac{\partial}{\partial x}\left[\tau(\gamma-1)\frac{\partial W}{\partial x}\right] + \frac{\partial}{\partial y}\left[\tau(\gamma-1)\frac{\partial W}{\partial y}\right] + \frac{\partial}{\partial z}\left[\tau(\gamma-1)\frac{\partial W}{\partial z}\right] \\
& + \frac{\partial}{\partial x}\left\{\mu'\left[u\frac{\partial u}{\partial x} + v\frac{\partial u}{\partial y} + w\frac{\partial u}{\partial z}\right]\right\} + \frac{\partial}{\partial x}\left[\lambda'(u\Lambda)\right] \\
& + \frac{\partial}{\partial y}\left\{\mu'\left[u\frac{\partial v}{\partial x} + v\frac{\partial v}{\partial y} + w\frac{\partial v}{\partial z}\right]\right\} + \frac{\partial}{\partial y}\left[\lambda'(v\Lambda)\right] \\
& + \frac{\partial}{\partial z}\left\{\mu'\left[u\frac{\partial w}{\partial x} + v\frac{\partial w}{\partial y} + w\frac{\partial w}{\partial z}\right]\right\} + \frac{\partial}{\partial z}\left[\lambda'(w\Lambda)\right] \qquad . \qquad \text{(B.39)}
\end{aligned}
$$

where $\mu'(\mu) = \lambda'(\lambda) = (\gamma-1)E_k\tau \approx (\gamma-1)\rho e\tau$ and $\Lambda = \frac{\partial u}{\partial x} + \frac{\partial v}{\partial y} + \frac{\partial w}{\partial z}$. For the first three terms in the right hand side, because we know Since *W* should have the same dimension as ρe^2, an approximate formulation for *W* could be defined here as $W = k\rho e^2$, where *k* is a constant. Therefore, the first three terms on the right hand side of Eq. (B.39) could be simplified and the result for the first term is reduced to

$$\frac{\partial}{\partial x}\left[\tau(\gamma-1)\frac{\partial W}{\partial x}\right]=\frac{\partial}{\partial x}\left[2k\tau(\gamma-1)\rho e\frac{\partial e}{\partial x}\right]=\frac{\partial}{\partial x}\left[2k\tau(\gamma-1)\rho e\frac{R}{(\gamma-1)}\frac{\partial T}{\partial x}\right]=\frac{\partial}{\partial x}\left[2k\tau\rho eR\frac{\partial T}{\partial x}\right] \quad .$$

This means that thermal conductivity is defined as $\kappa=2k\tau\rho eR$, so the Prandtl number is derived as,

$$\Pr=\frac{\mu C_p}{\kappa}=\frac{(\gamma-1)\rho e\tau C_p}{2k\rho e\tau R}=\frac{\gamma}{2k} \quad . \tag{B.40}$$

Finally, combining Eqs. (B.32) and (B.39) together, it would give the right formulation for the kinetic energy of the fluid as,

$$\begin{aligned}
&\frac{\partial}{\partial t}(E_k)+\frac{\partial}{\partial x}\left[(E_k+\Phi)u\right]+\frac{\partial}{\partial y}\left[(E_k+\Phi)v\right]+\frac{\partial}{\partial z}\left[(E_k+\Phi)w\right]\\
&=\frac{\partial}{\partial x}\left(\kappa\frac{\partial T}{\partial x}\right)+\frac{\partial}{\partial y}\left(\kappa\frac{\partial T}{\partial x}\right)+\frac{\partial}{\partial z}\left(\kappa\frac{\partial T}{\partial x}\right)\\
&+\frac{\partial}{\partial x}\left\{\mu\left[u\frac{\partial u}{\partial x}+v\frac{\partial u}{\partial y}+w\frac{\partial u}{\partial z}\right]\right\}+\frac{\partial}{\partial x}\left[\lambda(u\Lambda)\right]\\
&+\frac{\partial}{\partial y}\left\{\mu\left[u\frac{\partial v}{\partial x}+v\frac{\partial v}{\partial y}+w\frac{\partial v}{\partial z}\right]\right\}+\frac{\partial}{\partial y}\left[\lambda(v\Lambda)\right]\\
&+\frac{\partial}{\partial z}\left\{\mu\left[u\frac{\partial w}{\partial x}+v\frac{\partial w}{\partial y}+w\frac{\partial w}{\partial z}\right]\right\}+\frac{\partial}{\partial z}\left[\lambda(w\Lambda)\right] \quad ,
\end{aligned} \tag{B.41}$$

where $E_k=\rho e+\frac{1}{2}\rho|\mathbf{u}|^2$, $\kappa=2k\tau\rho eR$ and $\mu=\lambda=(\gamma-1)E_k\tau\approx(\gamma-1)\rho e\tau$. Therefore, starting from the basic Boltzmann equation and the BGK model, the mass, momentum and kinetic energy equations for the fluid can be derived. The full set of unsteady compressible Navier-Stokes equations and the gas equation of state for diatomic gases are correctly recovered. The only assumption is that the Knudsen number should be very small.

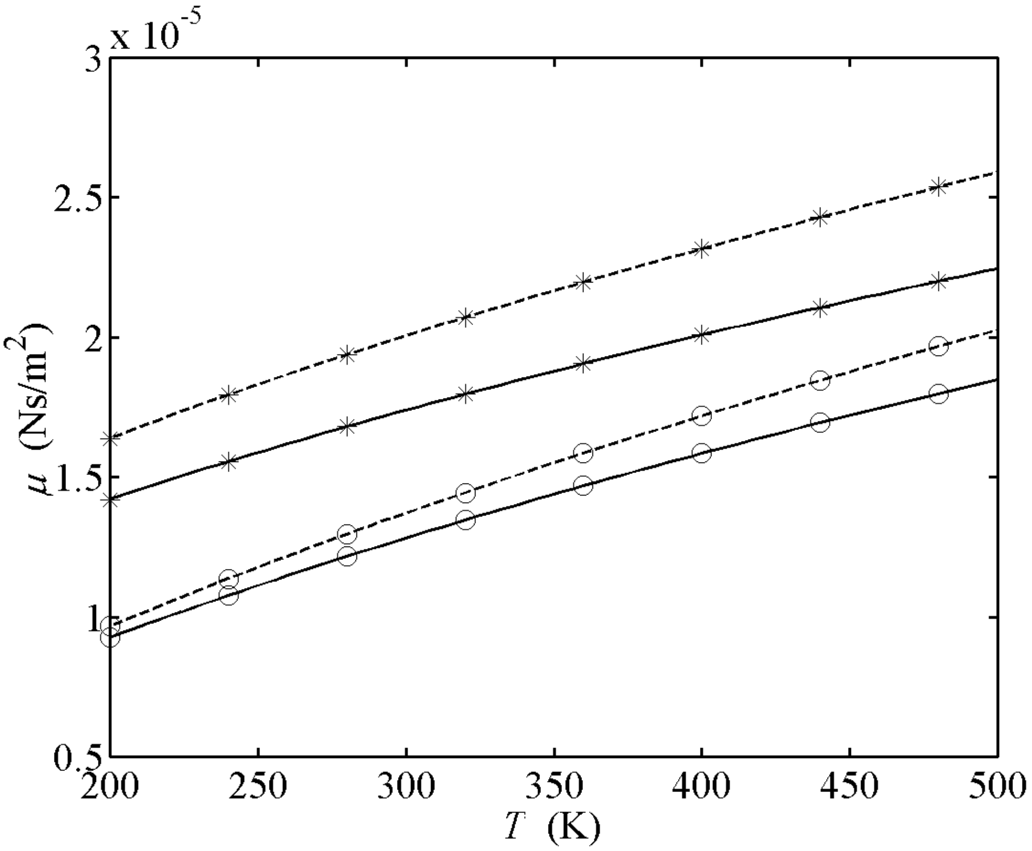

Figure 4.1 Variations of the first coefficient of viscosity with temperature: ———, oxygen; – – – – – , nitrogen; *, single relaxation time model, Eq. (4.25); o, two relaxation time model, Eq. (4.29).

(a)

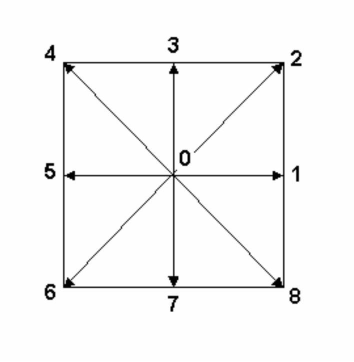

$$\xi_0 = 0,$$

$$\xi_i = c\left(\cos\left(\frac{\pi(i-1)}{4}\right), \sin\left(\frac{\pi(i-1)}{4}\right)\right), i = 1, 3, 5, 7$$

$$\xi_i = \sqrt{2}c\left(\cos\left(\frac{\pi(i-1)}{4}\right), \sin\left(\frac{\pi(i-1)}{4}\right)\right), i = 2, 4, 6, 8$$

$$\begin{cases} A_0 = 1 + 2\gamma\theta^2 - 3\theta \\ A_1 = A_3 = A_5 = A_7 = -\gamma\theta^2 + \theta \\ A_2 = A_4 = A_6 = A_8 = \frac{\gamma}{2}\theta^2 - \frac{1}{4}\theta \end{cases}$$

(b)

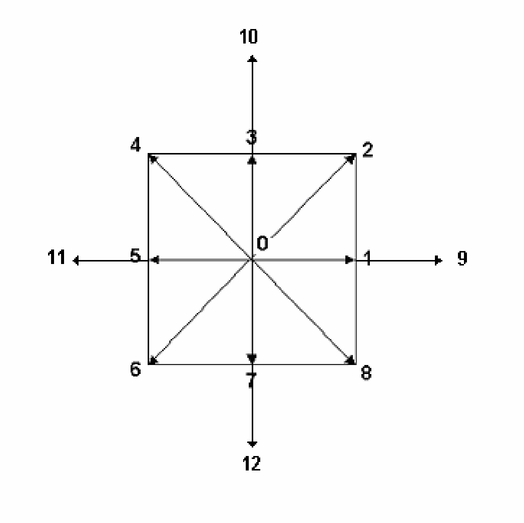

$$\xi_0 = 0,$$

$$\xi_i = c\left(\cos\left(\frac{\pi(i-1)}{4}\right), \sin\left(\frac{\pi(i-1)}{4}\right)\right), i = 1, 3, 5, 7$$

$$\xi_i = \sqrt{2}c\left(\cos\left(\frac{\pi(i-1)}{4}\right), \sin\left(\frac{\pi(i-1)}{4}\right)\right), i = 2, 4, 6, 8$$

$$\xi_i = 2c\left(\cos\left(\frac{\pi(i-1)}{2}\right), \sin\left(\frac{\pi(i-1)}{2}\right)\right), i = 9, 10, 11, 12$$

$$\begin{cases} A_0 = 1 - \frac{5}{2}\theta + (-\frac{3}{2} + 2\gamma)\theta^2 \\ A_1 = A_3 = A_5 = A_7 = \frac{2}{3}\theta + (1-\gamma)\theta^2 \\ A_2 = A_4 = A_6 = A_8 = (-\frac{3}{4} + \frac{1}{2}\gamma)\theta^2 \\ A_9 = A_{10} = A_{11} = A_{12} = -\frac{1}{24}\theta + \frac{1}{8}\theta^2 \end{cases}$$

Figure 4.2 Definitions of the lattice velocity models: (a) D2Q9; (b) D2Q13.

5 Application of the Lattice Boltzmann Method to Aeroacoustic Problems

In Chapter 4, a full description of a one-step CAA method using LBM has been given. It is shown that the improved LBM can recover the Navier-Stokes equations, the gas equation of state for diatomic gases, and the viscosity-temperature relation (Sutherland law) correctly. The lattice models and the numerical scheme have been introduced. The purpose of this chapter is to validate this technique against standard DNS calculations of some benchmark aeroacoustic problems. Many practical aeroacoustic simulations aim to predict sound radiation created by unsteady flows and their interactions with solid boundaries. Correct simulation of wave propagation is an important measure of the success of a numerical model for aeroacoustic simulation. With all viscous terms neglected, the Navier-Stokes equations reduce to the Euler equations which support three modes of waves, namely acoustic, vorticity and entropy waves. The acoustic waves are isotropic, non-dispersive, non-dissipative and propagate with the speed of sound, $c = \sqrt{\gamma RT}$. The vorticity and entropy waves are non-dispersive, non-dissipative and propagate in the same direction of the mean flow with the same velocity of the flow. Propagations of these three different types of waves are selected for the validation of the improved LBM in this chapter.

The accuracy of the improved LBM aeroacoustic simulation is assessed by comparing the LBM calculations with the results obtained using a convectional one-step DNS to carry out CAA by solving the Navier-Stokes equations (in Chapter 2). In the following, “LBM” would be used to denote the one-step CAA method solving the improved BE and "DNS" would be used to signify the other one-step method using DNS to solve the Navier-Stokes equations. Generally, a measure of the difference between the LBM and DNS results of a macroscopic variable ***b*** is expressed in terms of the L_p integral norm, i.e.

$$\left\| L_p(\mathbf{b}) \right\| = \left[\frac{1}{M} \sum_{j=1}^{M} \left| \mathbf{b}_{\mathrm{LBM},j} - \mathbf{b}_{\mathrm{DNS},j} \right|^p \right]^{\frac{1}{p}} \quad , \tag{5.1}$$

$$\left\| L_\infty(\boldsymbol{b}) \right\| = \max_j \left| \boldsymbol{b}_{\mathrm{LBM},\,j} - \boldsymbol{b}_{\mathrm{DNS},\,j} \right| \quad . \tag{5.2}$$

for any integer p and for the maximum norm, respectively.

Five test cases are carried out to validate the proposed LBM. These are: (i) the propagation of a plane pressure pulse in a stationary fluid, (ii) the propagation of a circular pulse in a stationary fluid, (iii) a plane sinusoidal wave propagation in quiescent fluid, (iv) simulations of an acoustic, an entropy and a vortex pulse convected with subsonic plug flow with a velocity u_∞ and (v) the propagation speed of sound under different Mach number conditions.

In the first three cases the non-dimensional parameters for the length, time, density, velocity, pressure and temperature are specified as $L_0,\ L_0/c_0,\ \rho_0,\ c_0,\ \rho c_0^2,\ T_0$ and the Reynolds number is defined by $Re = \rho_0 L_0 c_0 / \mu$. For the LBM, the pressure is implied in the kinetic equation and can be deduced from the state equation $p = (\gamma - 1)\rho e$. The normalized internal energy and sound speed are given by $e = T / \left[\gamma \left(\gamma - 1 \right) \right]$ and $c = \sqrt{T}$. In the third and forth cases, the non-dimensional parameters for time, density, velocity, pressure and temperature are $L_0/u_0,\ \rho_0,\ u_0,\ \rho u_0^2,\ T_0$, respectively, and $M = u_0/c_0$ is the Mach number. The LBM and DNS solutions are compared in all these cases.

Mostly when we defined an initial condition for ρ, u, v and p, the equilibrium distribution of f_i^{eq} can be calculated by Eq. (4.31) with the given weights and coefficients given in Fig. 4.2, then, the initial particle distribution f_i was set equal to the corresponding f_i^{eq}. In case (iii), analytical solutions are also available; these too will be shown for comparisons with the LBM and DNS solutions. All physical quantities in the following discussion are dimensionless, except where specified.

5.1 Propagation of a Plane Pressure Pulse

This 1-D problem aims to validate the accuracy and robustness of the proposed LBM and, at the same time, to assess the efficiency of the proposed lattice models. The distribution function $f_i(\boldsymbol{x},t)=f(\boldsymbol{x},\xi_i,t)$ is developing with the collision function and the streaming function of Eq. (5-30). The initial fluid state is specified with the same conditions as the DNS case § 3.2: a small plane pressure fluctuation in the center of a tube, such that

$$\rho=\rho_\infty,\ u=0,\ v=0,\ p=p_\infty+\varepsilon\exp(-\ln 2\times\frac{x^2}{0.08^2}) \quad , \tag{5.3}$$

where the mean field density and pressure are given by $\rho_\infty=1$ and $p_\infty=1/\gamma$, the pulse amplitude ε is set to 4×10^{-6}, 16×10^{-6} and 100×10^{-6}, respectively, and $\mathrm{Re}=5000$ is specified in this case. The computational domain size of the tube is $-5\le x\le 5$ by $0\le y\le 2$. A uniform grid of size 0.02x0.02 is adopted. Slip boundary conditions are applied on the upper and lower tube surfaces in the DNS calculation. The stability criterion of the collision term requires that the time step should be $\Delta t<\tau/2$ (Tsutahara et al. 2002); therefore, $\Delta t=0.0001$ is chosen for the present LBM computations. Two buffer zones are specified in the DNS calculation in order to simulate a true non-reflecting inlet and outlet boundary condition. For all

LBM calculations, the gradient of the distribution function *f* on all boundaries are set to zero. When all disturbances are far away from the numerical boundaries, these conditions can ensure that there is essentially no error contribution coming from the boundary treatment.

In this case the initial conditions Eq. (5.3) essentially combine one acoustic wave and one entropy wave. These two waves overcome the density fluctuations with each other only for the initial state. After the acoustic wave leaves the center area, the density fluctuations created by the entropy wave would appear in the center. Fig. 5.1 shows the fluctuations along the centerline of the tube at t = 1.0 and t = 3.0 for the case $\varepsilon = 100 \times 10^{-6}$. The LBM and DNS simulations show a slight difference in the density at the center when the acoustic pulse propagates towards computational boundaries. However, the density distribution in the central region is essentially the same. The two positive density fluctuation peaks are leaving the center with a propagation speed $c = 1$ and the amplitude of this density fluctuation is $\hat{\rho} = 4 \times 10^{-5}$ (t = 3.0). At the same corresponding positions, there are two pressure fluctuation peaks with a value of $\hat{p} = 4 \times 10^{-5}$. Actually these two waves are the exact acoustic waves because the transmission speed is the physical sound speed and the amplitudes follow the acoustic relation, $\hat{p} = c^2 \hat{\rho}$. These results show that the proposed LBM can replicate the correct acoustic waves and the calculated macroscopic quantities are developing correctly, just as the DNS solution indicates.

This is evident from a comparison of the calculated $\left\| L_p(p) \right\|$ (pressure). Fig 5.2 shows the time-dependent difference in the behavior of $\left\| L_1(p) \right\|$, $\left\| L_2(p) \right\|$ and $\left\| L_\infty(p) \right\|$ ($\varepsilon = 4 \times 10^{-6}$). Both lattice (D2Q9 and D2Q13) solutions are reported. The differences between the LBM and DNS solutions using the D2Q13 lattice are much smaller than those using the D2Q9 lattice. For example, consider the $\left\| L_2(p) \right\|$ value, the difference obtained for the D2Q13 lattice is about 10^{-11} while the corresponding value for the D2Q9 lattice is close to 10^{-9}. This shows that the D2Q13 lattice could effect an improvement in $\left\| L_p(p) \right\|$ of 2 orders of magnitude when only 4 more discrete velocities are specified. In view of this, only the D2Q13 lattice model results are presented in the following discussion.

The pulse amplitude effect on the difference $\left\| L_2(p) \right\|$ is compared in Fig. 5.1. The criterion of a Taylor expansion on a Maxwellian distribution requires that the flow speed u to be much smaller than the particle speed $\boldsymbol{\xi}$ and the error of this expansion would occur in the term of $O\left(\boldsymbol{u}^4 / \theta^2\right)$. When the pulse amplitude is smaller, the disturbance $\boldsymbol{u}$ is also smaller. This would lead to a smaller error term $O\left(\boldsymbol{u}^4 / \theta^2\right)$. Therefore, $\left\| L_2(p) \right\|$ would be smaller for $\varepsilon = 4 \times 10^{-6}$ than for $\varepsilon = 16 \times 10^{-6}$ and $\varepsilon = 100 \times 10^{-6}$. This result is clearly demonstrated in Fig. 5.1, which shows that the performance of the LBM is better with smaller fluctuations than those large fluctuations.

5.2 Propagation of a Circular Pressure Pulse

If an initial circular pulse were imparted to a uniform fluid, the fluctuations thus created would propagate equally in all directions. This means that, at any time, the pulse would remain circular in shape. However, the lattice velocity model restricts the particles to move in certain discrete directions, such as $0, \pm\pi/4, \pm\pi/2$ and π. In order to test the ability of the LBM with a D2Q13 lattice model to replicate the symmetry property of the circular pulse, it is used to simulate a circular initial pressure pulse in a uniform flow. The initial conditions are specified as the same as the DNS case in § 3.3, such that

$$\rho = \rho_\infty\,,\ u = 0\,,\ v = 0\,,\ p = p_\infty + \varepsilon \exp(-\ln 2 \times \frac{x^2 + y^2}{0.2^2}) \quad , \tag{5.4}$$

where $\rho_\infty = 1$, $p_\infty = 1/\gamma$, $\varepsilon = 16 \times 10^{-6}$ and $\mathrm{Re} = 5000$. The computational domain is 20x20 and the grid size is 0.05x0.05. Both LBM and DNS are used to simulate this problem.

Since the only disturbance lies in the middle domain, the boundary condition for the LBM is very simple. A zero order continuity of particle distribution function is used for all the boundaries (§4.7). That is, the boundary solutions f_1 and f_N would be corrected by nearby inner point values, or $f_1 = f_2$ and $f_N = f_{N-1}$, etc. This technique proves to be non-reflecting; before the outgoing waves touch the boundaries, the solution on the boundary is stable and no spurious waves are created by the boundaries. Furthermore, this technique is simple in terms of programming.

The contours of the pressure and *u* fluctuations are plotted in Fig. 5.4. The upper half of the computation domain is plotted the LBM solution and the lower half the DNS solution at the same time. It is clear that the contours of the LBM solution have no discernible difference with those of the DNS result. This is despite of the fact that the LBM solution is derived from a D2Q13 velocity lattice model where particle velocities are specified for discrete directions only. This shows that the LBM simulation is just as valid as the DNS result.

5.3 Plane Sinusoidal Wave Propagation in Quiescent Fluid

Similar to previous comparisons, this test aims to validate LBM computations for continuous waves in quiescent fluid. The DNS solutions have been discussed in §3.4, therefore, they will be used as benchmarks for the LBM simulations. In LBM computations, the particle velocity distribution functions are primitive variables, thus the sinusoidal pressure excitation given by Eq. (3.5) (in § 3.4) could be directly defined. Even though the relation between pressure and f_i has not been defined, the sinusoidal excitation method still could be used to drive the particle distribution functions. Using these excitations, the mean velocity at this local area should be zero at all time. This means that, for this line source, the particle distribution should be symmetric about the line source and the particles should have the same change going from the left hand side or from the right hand side. On the other hand, if a point source is considered, the distribution should be equal in all directions. Thus, an *isotropic* consideration should be taken for all distribution functions f_i, such that

$$f_i = \bar{f}_i \left[1 + \varepsilon \sin\left(\frac{2\pi c}{\lambda} t \right) \right] \quad , \tag{5.5}$$

where $\bar{f}_i$ is the particle equilibrium of the *i*-th direction in the mean state.

The boundary conditions for this problem are very important, because continuous waves are excited inside and, if there is any reflection, the continuous waves would generate more and more spurious waves inside. This would drive the whole solution to a wrong state. As mentioned in Chapter 4, for LBM, a first-order continuity of distribution function is used for the upper and lower boundaries, two buffer regions were attached outside the left hand and right hand side boundaries; the absorbing term has already been introduced in §4.7.

Invoking these assumptions for the excitations, the LBM scheme gives proper sinusoidal wave solutions for $\lambda = 2$ and $\lambda = 10$. The excitation amplitudes are then selected ($\varepsilon = 2 \times 10^{-8}$ for $\lambda = 2$, $\varepsilon = 2 \times 10^{-7}$ for $\lambda = 10$) to recover the same density fluctuations as the DNS solutions. The density contours and distributions are plotted in Fig. 5.5 ($\lambda = 2$) and Fig. 5.6 ($\lambda = 10$). Evidently the present LBM scheme is truly isotropic and no distortion in sound propagation is observed.

5.4 Simulations of Acoustic, Entropy and Vortex Pulses

The acoustic, entropy and vorticity pulses are basic fluctuations in aeroacoustics problems. In this case, the pulses are developing in a uniform mean flow. Basically, only the acoustic pulse is propagating with the sound speed, the entropy pulse and the vortex pulse would move with the mean flow. The initial conditions are:

$$\rho = \rho_\infty + \varepsilon_1 \exp\left[-\ln 2 \times \frac{(x+1)^2 + y^2}{0.2^2}\right] + \varepsilon_2 \exp\left[-\ln 2 \times \frac{(x-1)^2 + y^2}{0.4^2}\right] , \tag{5.6a}$$

$$u = u_\infty + \varepsilon_3 y \exp\left[-\ln 2 \times \frac{(x-1)^2 + y^2}{0.4^2}\right] , \tag{5.6b}$$

$$v = u_\infty + \varepsilon_3 (x-1) \exp\left[-\ln 2 \times \frac{(x-1)^2 + y^2}{0.4^2}\right] , \tag{5.6c}$$

$$p = p_\infty + \frac{1}{M^2} \varepsilon_1 \exp\left[-\ln 2 \times \frac{(x+1)^2 + y^2}{0.2^2}\right] , \tag{5.6d}$$

where M = 0.2 and $\varepsilon_1 = 0.0001,\ \varepsilon_2 = 0.001,\ \varepsilon_3 = 0.001$. The mean field has density, speed and pressure given by $\rho_\infty = 1,\ u_\infty = 1,\ v_\infty = 0,\ p_\infty = 1/\left(\gamma M^2\right)$ and Re = 1000. These pulse models follow the definitions of Tam and Webb (1993). The acoustic pulse is initialized at the point x = -1, y = 0. The entropy pulse and the vorticity pulse are initialized at x = 1, y = 0. The computational domain is $-10 \le x \le 10$ by $-10 \le y \le 10$ and the grid size is 0.05x0.05. For this problem with a relatively large mean flow, the mean flow effect could become critical because the symmetry lattice coefficients are based on the assumption that the flow speed is much smaller than the particle speed. An improvement to the proposed LBM model is given in the Appendix to address this problem. For this problem, the only source lies in the middle domain, a zero order continuity of the distribution function *f* (§4.7) is used for all the boundaries of the LBM calculation.

The pressure and the *u* velocity fluctuation contours are shown in Fig. 5.7 at $t = 1.0$ and $t = 1.5$. Both LBM and DNS results are shown together. The initial acoustic pulse causes disturbances. Since the mean flow speed is defined as 1.0, the center of the pulse has moved to $x = 0$, $y = 0$ at $t = 1.0$, and to $x = 0.5$, $y = 0$ at $t = 1.5$. The acoustic pressure fluctuation is propagating with $c = 1/M = 5$ and exhibit circles of radii equal to 5 and 7.5 at the same moment. The *u* velocity fluctuation is symmetric about the *x*-axis. For the vorticity pulse, the center of the vortex would move to $x = 2$, $y = 0$ at $t = 1.0$ and to $x = 2.5$, $y = 0$ at $t = 1.5$. The distribution of the *u* velocity fluctuation from this pulse would give the same absolute fluctuations that propagate along the negative *x*-axis. The pressure and *u* velocity fluctuations are plotted in Fig. 5.8. The LBM and DNS simulations are essentially identical and they agree well with the analytical inviscid solution.

The same case with Re = 100 is also calculated in order to investigate the effect of viscosity on the LBM simulation. The pressure and velocity fluctuations at $t = 1.0$ are compared in Fig. 5.9 where the distributions along $-6 \le x \le 0$ are shown. The star point represents the LBM solution while the DNS result is given by the dotted line. The solid line shows the analytical inviscid solution. Again, LBM and DNS give essentially the same solution and are close to the inviscid result. There is a discernible viscous effect on the acoustic pulse which is essentially a disturbance generated from the viscous effect on the entropy pulse. The $\|L_p\|$ differences for pressure and *u* velocity fluctuations are list in Table 5.1.

There are two macroscopic velocity scales in this case, namely the mean flow velocity and the fluctuation propagation velocity. In order to assess the correctness of the LBM in resolving small fluctuation propagation in a mean flow, it is worthwhile to study the spreading of the acoustic pulse. Fig. 5.10 reports the decay of the acoustic pulse peak in LBM and DNS solutions at Re = 100 and 1000. The analytical result is also illustrated. For an acoustic pulse spreading in two dimensions, the local intensity of the wave I should be proportional to $1/r$ due to conservation of total energy $e = I \cdot 2\pi r$, where r is the radial distance. In the absence of viscosity, the intensity bears a relationship with instantaneous pressure peak amplitude A as $I \propto A^2$. Therefore, the analytical result should be a straight line in Fig. 5.10 with slope equal to –1/2. For Re = 1000, the amplitudes are very close to the inviscid solution, indicating the acoustic propagation is correctly captured with a viscous formulation in the DNS and LBM calculations at this Re. For Re = 100, the LBM and DNS solutions are essentially identical. The difference in peak amplitude is only 6% after the pulse has propagated a distance equal to 19 times the initial pulse-width (r = 7.5). It can be observed that viscosity has a significant effect and gives rise to a difference of about 20% between the Re = 100 and Re = 1000 case at the same distance.

5.5 Speed of Sound in Flows with Different Mach Numbers

In the previous three sections, the plan pulse, the circular pulse and the three pulses are calculated using the LBM scheme. The conversional DNS solutions are used as the reference to validate the LBM calculations. The validity of LBM for a direct aeroacoustic simulation depends on its ability to recover the equation of state of the gas and its first coefficient of viscosity correctly. It has been demonstrated that LBM can replicate these pulses. Furthermore, because of the very small energy of the acoustics field, a low dispersive and low dissipative scheme is required if the wave propagation speed were to be resolved accurately. If the governing equations are normalized with the uniform stream speed, in the non-dimensional equations, the propagation speed of sound should be the inverse of the Mach number, or $c = 1/M$. Therefore, a smaller Mach number would mean a larger sound speed. In this section, calculations were carried out to verify that the LBM could replicate c correctly over the Mach number range $0.01 \le M \le 0.9$ where no shock is present. Furthermore, it is also the objective to show that the theoretical relation between c and e can be recovered exactly over this range of M and a shock free environment. A Gaussian sound pulse in a uniform flow is used as the vehicle to demonstrate the validity and extent of the proposed LBM and the results are calibrated against theoretical results and DNS calculations of the same problem. Zero order continuity of distribution function is used to treat all the boundaries (§4.7).

The low dispersive and low dissipative nature of the scheme is verified by analyzing the power spectral density (PSD) of the wave form of the Gaussian sound pulse. According to Hu et al. (1996), the maximum resolvable wave number $k_c^* \Delta x$ for this scheme is 0.433, where Δx is the spacing of a uniform mesh. This is determined using a criterion $\left| k^* \Delta x - k \Delta x \right| < 0.005$. In other words, the scheme can only resolve long waves with a cut off around 0.433. The PSD of the wave in each of these nine cases are essentially identical. The Δx chosen is independent of M and is taken to be 0.1. On the other hand, Δt varies from 2×10^{-7} to 1×10^{-4} for the range $0.01 \le M \le 0.9$. It is found that this choice of Δx and Δt gives very stable calculations over the range of M calculated. A sample plot of the PSD versus the dimensionless k^* (= $k\Delta x/\pi$) is shown in Fig. 5.11. It can be seen that the PSD is essentially zero beyond k^* = 1/2. Therefore, it can be concluded that the low dispersive and low dissipative Lele scheme (1992) can be used to simulate a

Gaussian sound pulse in a uniform flow. It will be shown later that the c and e thus recovered are in excellent agreement with theoretical results over the M range examined.

The *Re* specified for the range of M investigated is 10^3. Altogether 9 different inlet flows are investigated and these range from M = 0.01 to M = 0.9. The exact choices of M are listed in Table 5.2. The same Gaussian sound pulse is specified and it is defined as

$$\rho = \rho_\infty + \varepsilon \exp\left[-\ln 2 \times \frac{(x+1)^2 + y^2}{0.2^2} \right] \quad , \tag{5.7a}$$

$$u = u_\infty \quad , \tag{5.7b}$$

$$v = v_\infty \quad , \tag{5.7c}$$

$$p = p_\infty + \frac{1}{M^2} \varepsilon \exp\left[-\ln 2 \times \frac{(x+1)^2 + y^2}{0.2^2} \right] \quad , \tag{5.7d}$$

where the inlet conditions are given by $\rho_\infty = 1,\ u_\infty = 1,\ v_\infty = 0,\ p_\infty = 1/\left(\gamma M^2\right)$ and $\varepsilon = 10^{-4}$ is chosen for the present calculations. The accuracy of the numerical scheme used to solve the DNS and LBM equations has already been demonstrated in Fig. 5.11, it will not be repeated.

The objective of this section is to show that c can be recovered correctly using the modified LBM and the theoretical relation between c and e is validated. In order to verify that this is the case, two different ways of estimating c is proposed; one is to determine c by tracking the speed with which the peaks of the pulse move away from each other, a second method is to calculate c from $c = \sqrt{\gamma(\gamma - 1)e}$. Some sample plots of the pressure pulse for four M cases are shown in Fig. 5.12. These plots further show that the DNS and the LBM results are essentially identical. From these plots, the distance S between the peaks can be determined and since the time lapse is known, the speed with which the peaks moved away from each other can be determined. The calculations are carried out for different S and t and sample plots for M = 0.01 and 0.9 are shown in Fig. 5.13. In this figure is also shown the least square fit of all the S and t points chosen for the two M cases presented. These results show little or no error in the determination of c by this method.

From the calculated aerodynamic and acoustic fields, p, ρ and e are known. The p and ρ values can be substituted into $c = \sqrt{\gamma(\gamma - 1)e}$ to determine c and the c thus determined can be plotted against the expression for γ and e. The plots of c versus M for the two different ways of determining c are given in Figs. 5.14 and 5.15. The plot of c versus e for diatomic gas where $\gamma = 1.4$ is shown in Fig. 5.16. In these plots, the DNS and LBM results are shown with symbols while the theoretical analysis is represented by a solid curve. The errors in the determination of c compared to the theoretical values are listed in Table 5.2. It can be seen that a maximum error of 2.7% occurs in the M = 0.9 case; all other cases have errors less than this. The same error is calculated for the DNS and LBM schemes. The agreement between the theoretical, DNS and LBM results shown in Figs. 5.12, 5.12 and 5.14 is excellent. Both the aerodynamic and acoustic fields are resolved correctly within this M range and Re investigated. This shows that the modified LBM scheme is a valid alternative to the DNS scheme in DAS calculations for M varying from 0.01 to 0.9.

5.6 Relative Merits of LBM versus DNS

Having compared the performance of the LBM with the DNS in the simulations of one-step aeroacoustics problems, a word about the programming and computational requirements of the two different methods is in order. In terms of programming, the

LBM is much simpler. The LBM code consists of 420 lines compared to 1350 lines required for the DNS code. As for the computational time required, the CPU time for calculating 1000 time steps using a 100x100 grid differ for the three cases tested. For the plane pressure pulse case (1-D), the LBM is 25% more efficient than the DNS; for the circular pulse case (2-D) the DNS is about 20% more efficient; while for the three pulses case the DNS is about 30% more efficient. These comparisons are made with the D2Q13 velocity lattice model. If the D2Q9 model is used instead, the LBM is more efficient by a margin ranging from 15% to 50% for the 3 cases tested. However, the $\left\|L_p(\boldsymbol{b})\right\|$ accuracy suffers by two orders of magnitude (Fig. 5.2). In view of this, the most suitable lattice to use is the D2Q13 for all aeroacoustic problems tested.

5.7 Summary

The proposed LBM scheme has been validated in Chapter 5. Altogether 5 benchmark aeroacoustic problems were calculated to validate the one-step LBM technique for CAA. They are the 1-D acoustic pulse propagation, the circular acoustic pulse propagation, the plane sinusoidal wave propagation, the propagation of acoustic, vorticity and entropy pulses in a uniform mean flow, and the propagation speed for the Gaussian sound pulse. The accuracy of the method is established by comparing the calculations with analytical solutions and with DNS results. All comparisons show that the LBM aeroacoustic simulation possesses the same accuracy as DNS solutions for CAA and is a simpler numerical method. This is accomplished using a D2Q13 lattice only for all calculations.

Table 5.1 The Lp difference and the effect of Re. Here, $\hat{p} = p - p_\infty$, $\hat{u} = u - u_\infty$ and p_r, u_r are the analytical solutions.

$L_p = \left(\frac{1}{N} \sum_{-6<x<0} (\hat{p} - p_r)^p \right)^{1/p}$	L_1	L_2	L_∞
LBM ($\mathrm{Re} = 1000$)	8.8339e-007	1.8589e-006	8.9069e-006
DNS ($\mathrm{Re} = 1000$)	8.0505e-007	1.6447e-006	7.5991e-006
LBM ($\mathrm{Re} = 100$)	6.8489e-006	1.3173e-005	5.8618e-005
DNS ($\mathrm{Re} = 100$)	6.4574e-006	1.2113e-005	5.1829e-005

$L_p = \left(\frac{1}{N} \sum_{-6<x<0} (\hat{u} - u_r)^p \right)^{1/p}$	L_1	L_2	L_∞
LBM ($\mathrm{Re} = 1000$)	1.8577e-007	3.7268e-007	1.7917e-006
DNS ($\mathrm{Re} = 1000$)	1.6058e-007	3.2878e-007	1.5348e-006
LBM ($\mathrm{Re} = 100$)	1.4394e-006	2.6432e-006	1.1803e-005
DNS ($\mathrm{Re} = 100$)	1.2827e-006	2.4207e-006	1.0477e-005

Table 5.2 Comparison of the numerically calculated c with its theoretical value.

M	0.01	0.0125	0.02	0.05	0.1	0.3	0.5	0.7	0.9
Theoretical *c*	100	80	50	20	10	3.33	2	1.43	1.11
LBM/DNS calculated *c*	100	80	49.75	20.25	10.2	3.33	2	1.45	1.14
Error (%)	0	0	0.5	1.25	2	0	0	1.39	2.7

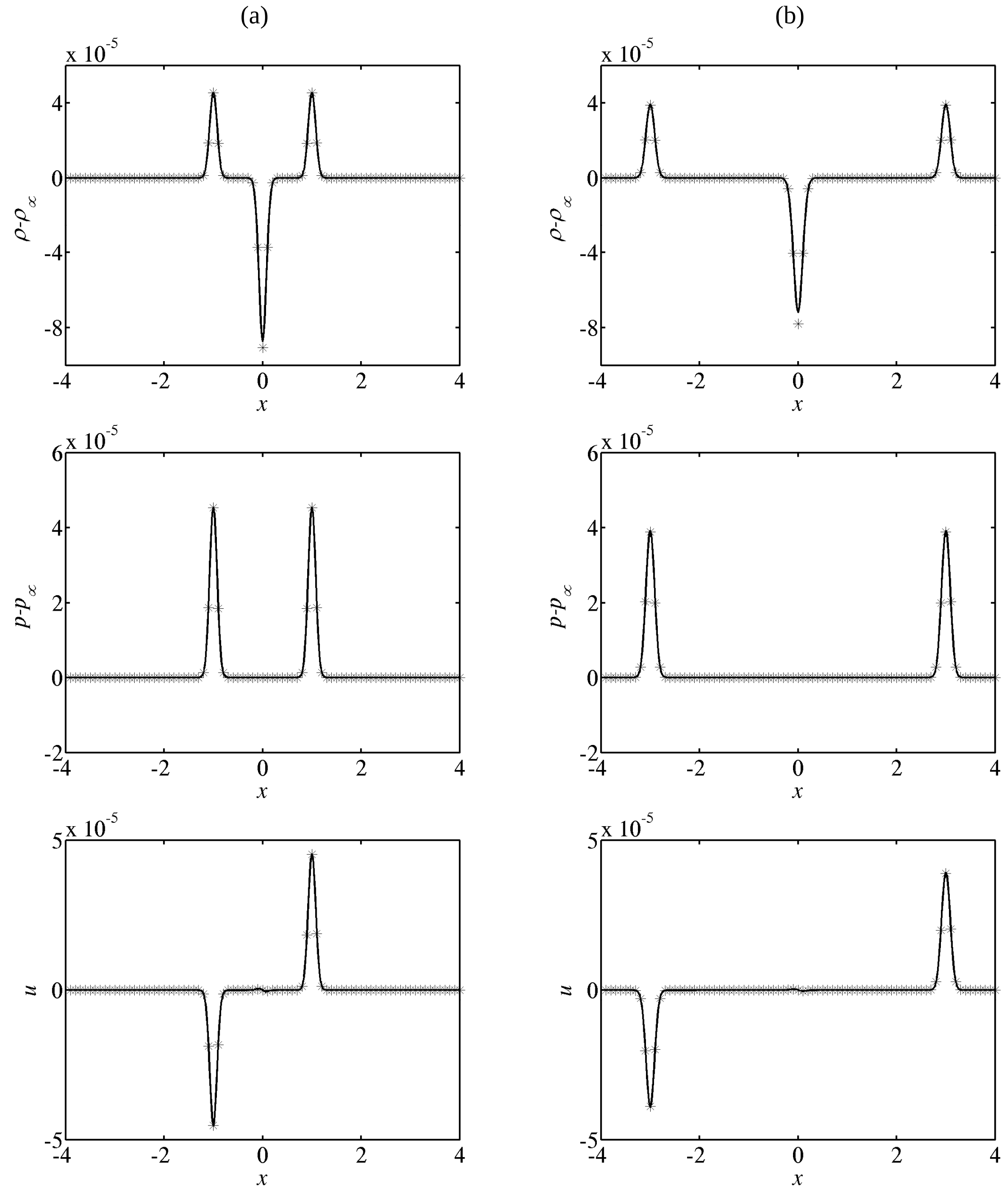

Figure 5.1 The density, pressure and velocity "u" fluctuations along the x-axis at (a) t = 1.0 and (b) t = 3.0 for $\varepsilon = 100 \times 10^{-6}$: *, LBM (D2Q13); ——— ,DNS.

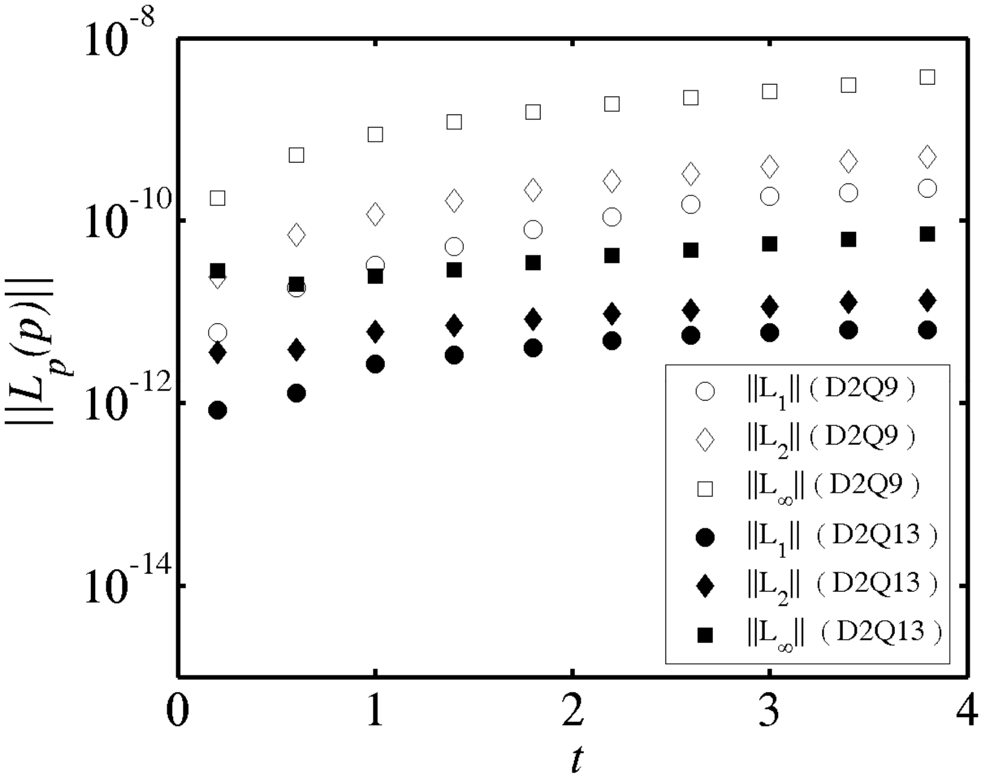

Figure 5.2 Time history of the difference $\left\|L_p(p)\right\|$.

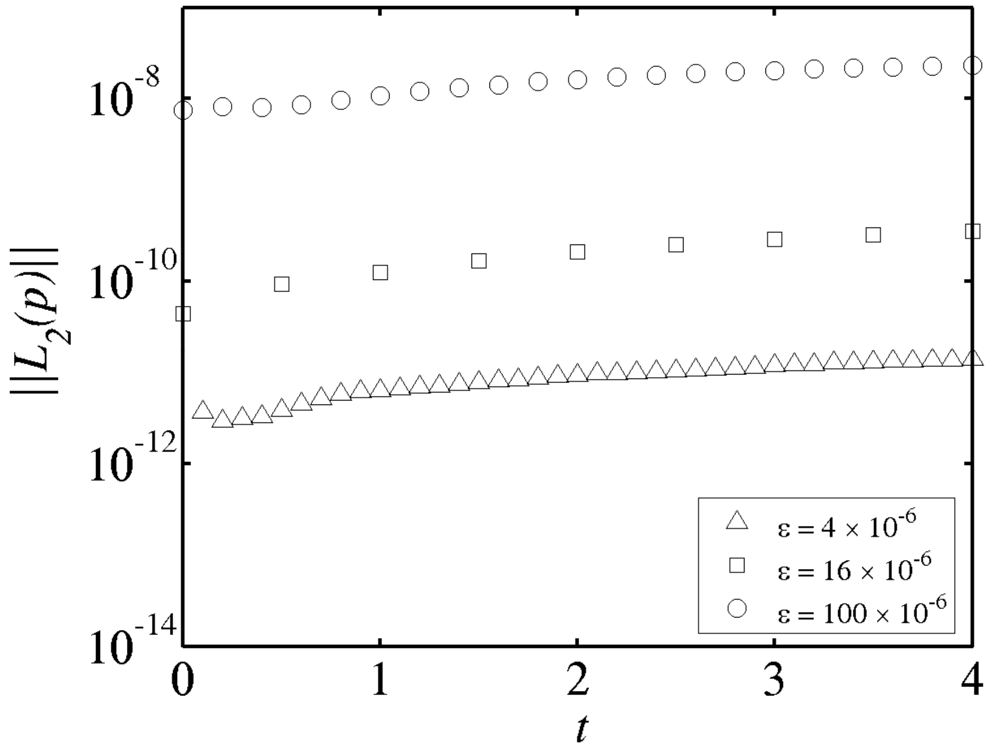

Figure 5.3 Time history of the difference $\|L_2(p)\|$ with D2Q13.

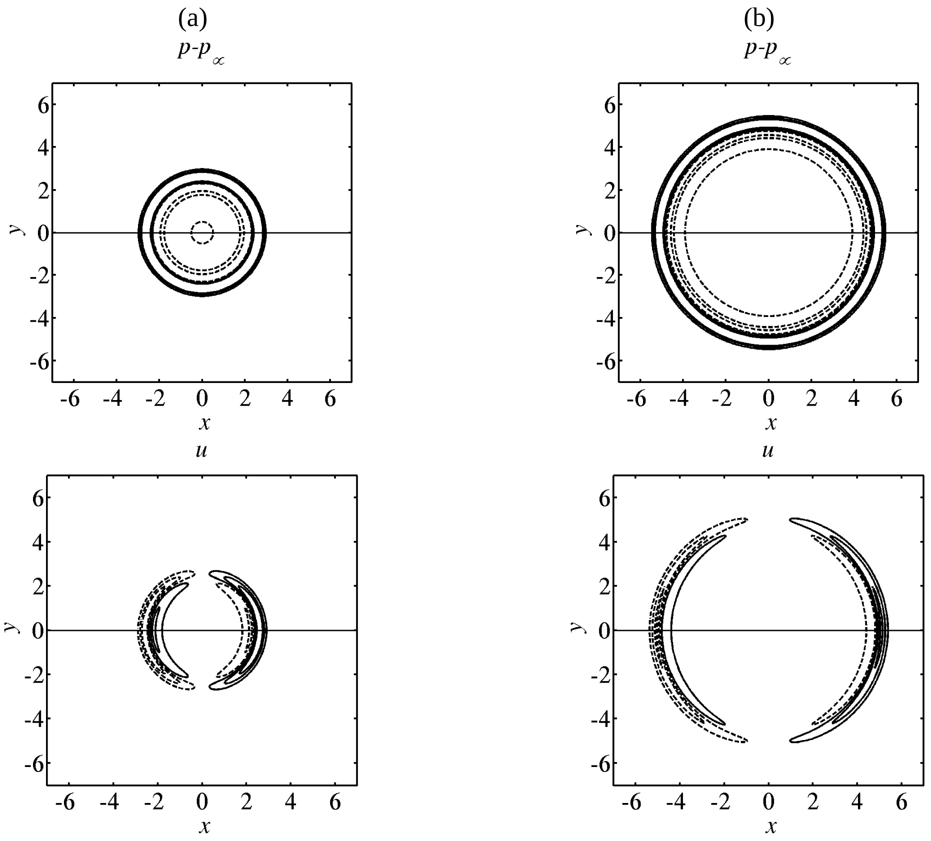

Figure 5.4 Pressure and velocity fluctuations at (a) t = 2.5 and (b) t = 5.0. Upper half of the domain is the LBM solution; lower half the domain is the DNS solution. For pressure fluctuations, 6 contours are equally distributed between -0.4×10^{-6} and 0.4×10^{-6} , for velocity fluctuations, 6 contours are equally distributed between -1×10^{-6} and 1×10^{-6}. ————, positive levels; – – – – – –, negative levels.

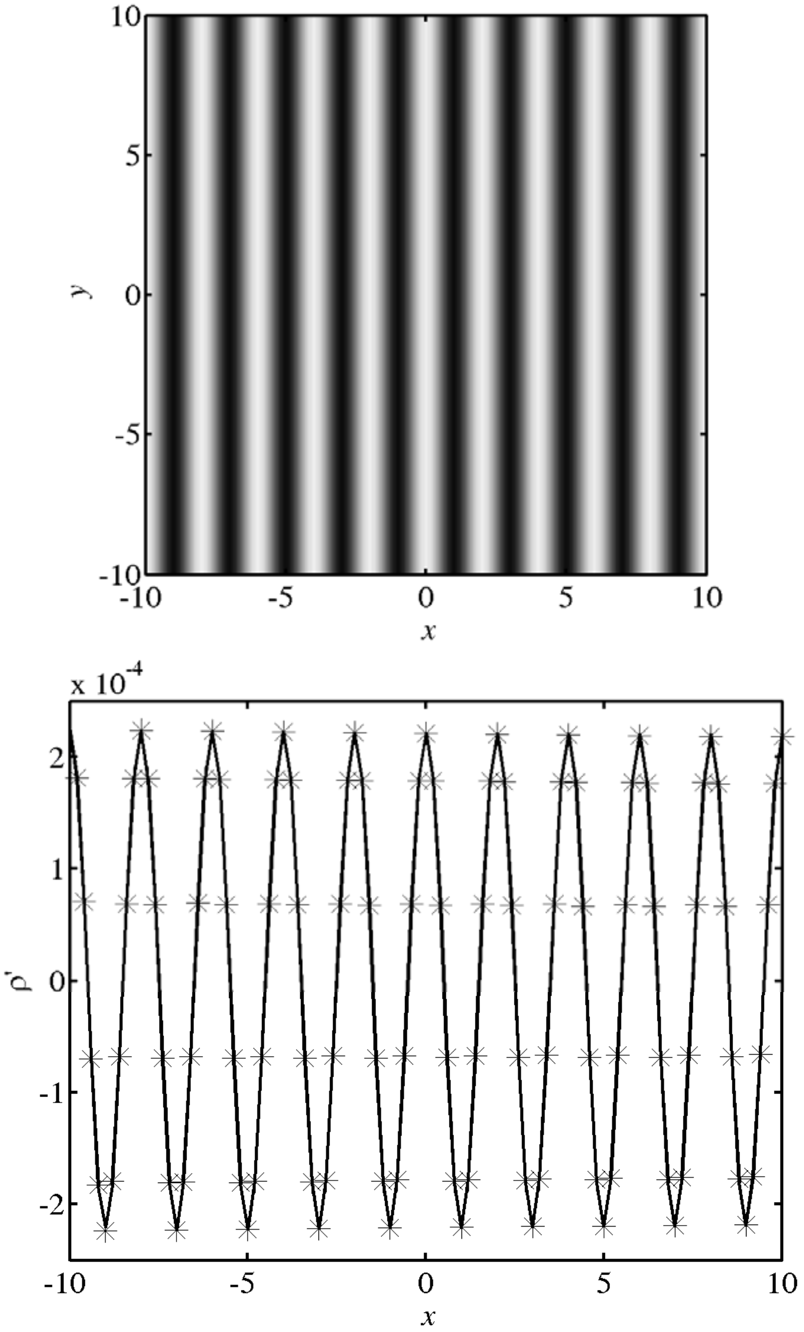

Figure 5.5 Propagation of sound wave in the x-direction: (a) density fluctuations contours; (b) comparison with DNS solutions; *, LBM, —— DNS ($\lambda = 2$).

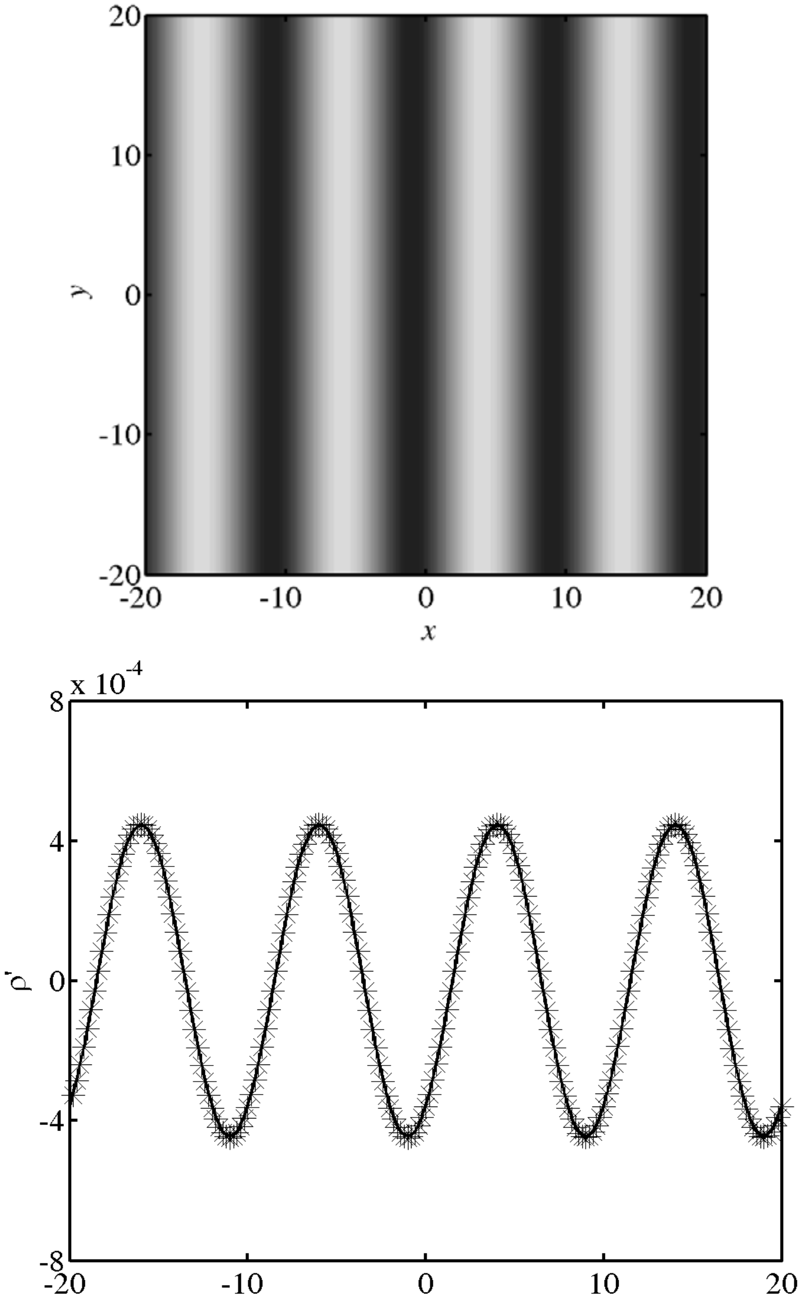

Figure 5.6 Propagation of sound wave in the x-direction: (a) density fluctuations contours; (b) comparison with DNS solutions; *, LBM, —— DNS ($\lambda = 10$).

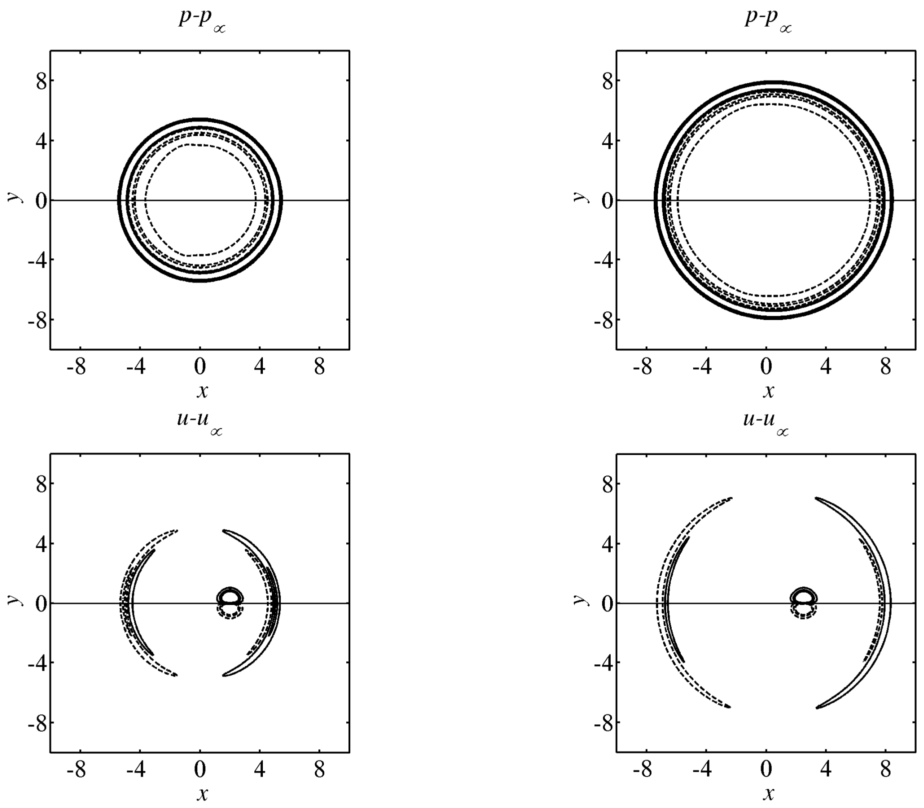

(a) (b)

Figure 5.7 Pressure and velocity fluctuations (a) t = 1.0 and (b) t = 1.5. Upper half of the domain is the LBM solution; lower half the domain is the DNS solution. For pressure fluctuations, 6 contours are equally distributed between -5×10^{-5} and 5×10^{-5}, for velocity fluctuations, 6 contours are equally distributed between -5×10^{-5} and 5×10^{-5}. ————, positive levels; – – – – – –, negative levels.

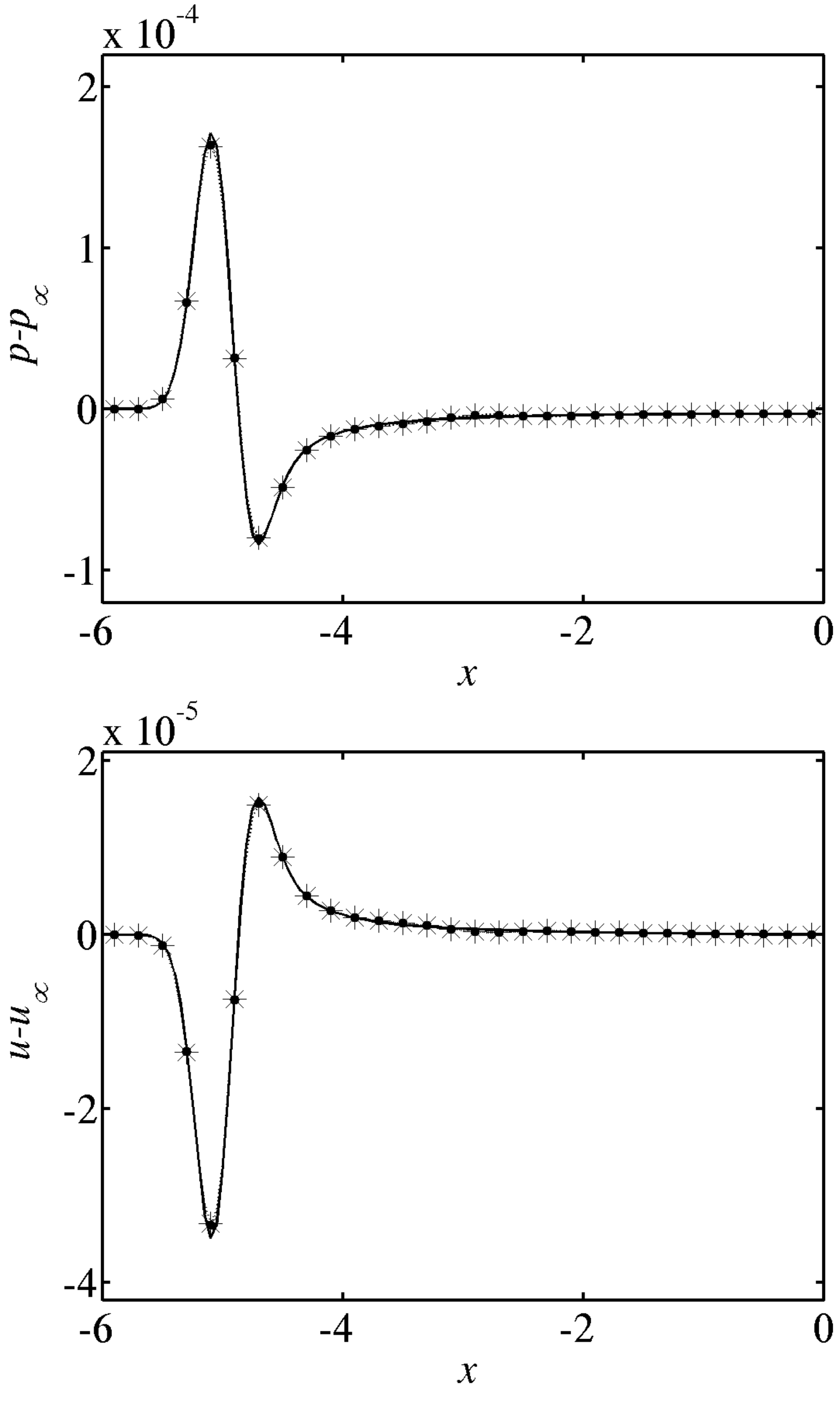

Figure 5.8 Pressure and velocity fluctuation distributions along the x-axis at t = 1.0 and Re = 1000: ——— analytical inviscid solution; *, LBM solution; ● DNS solution.

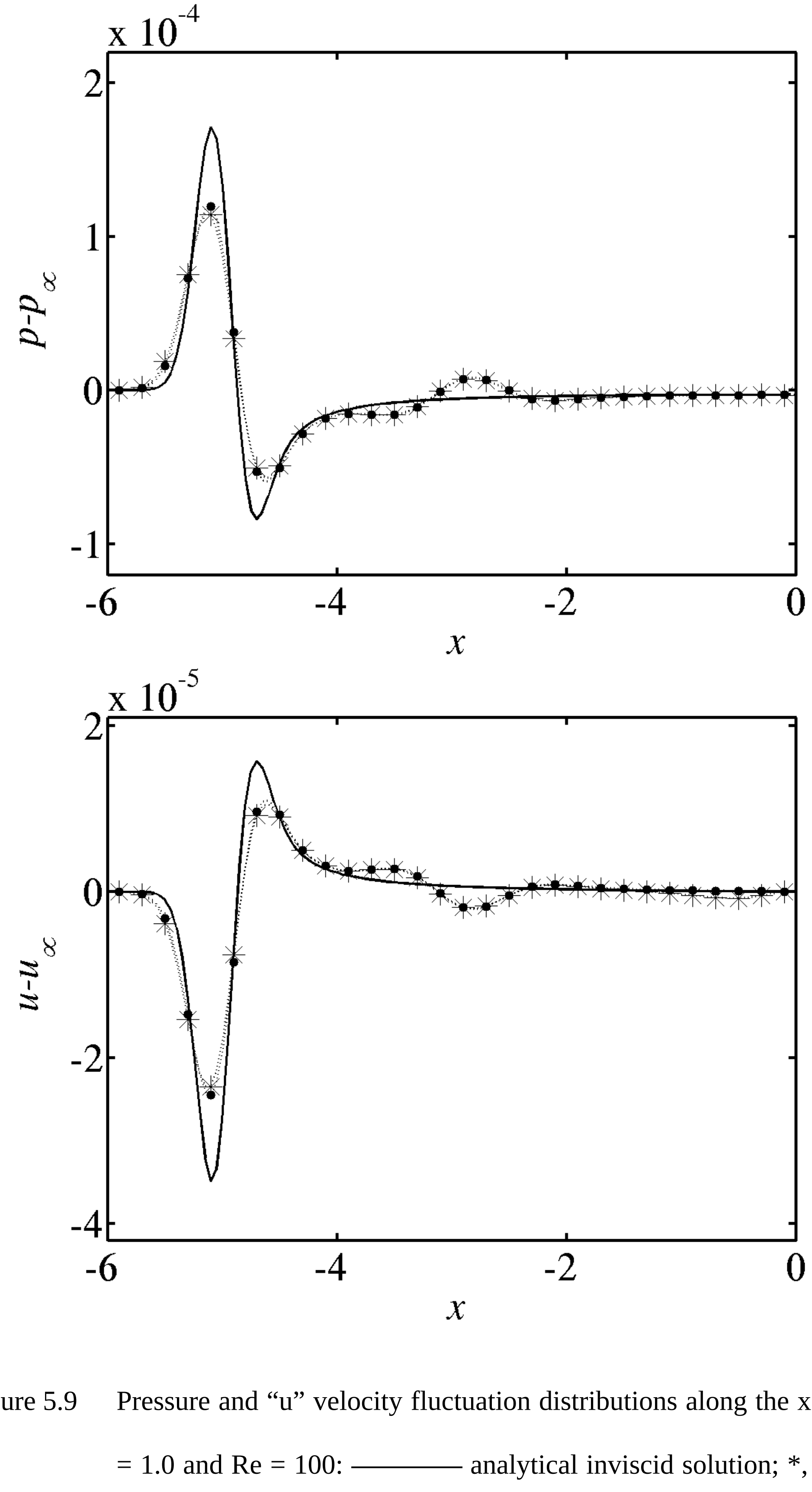

Figure 5.9 Pressure and “u” velocity fluctuation distributions along the x-axis at t = 1.0 and Re = 100: ———— analytical inviscid solution; *, LBM; ● DNS.

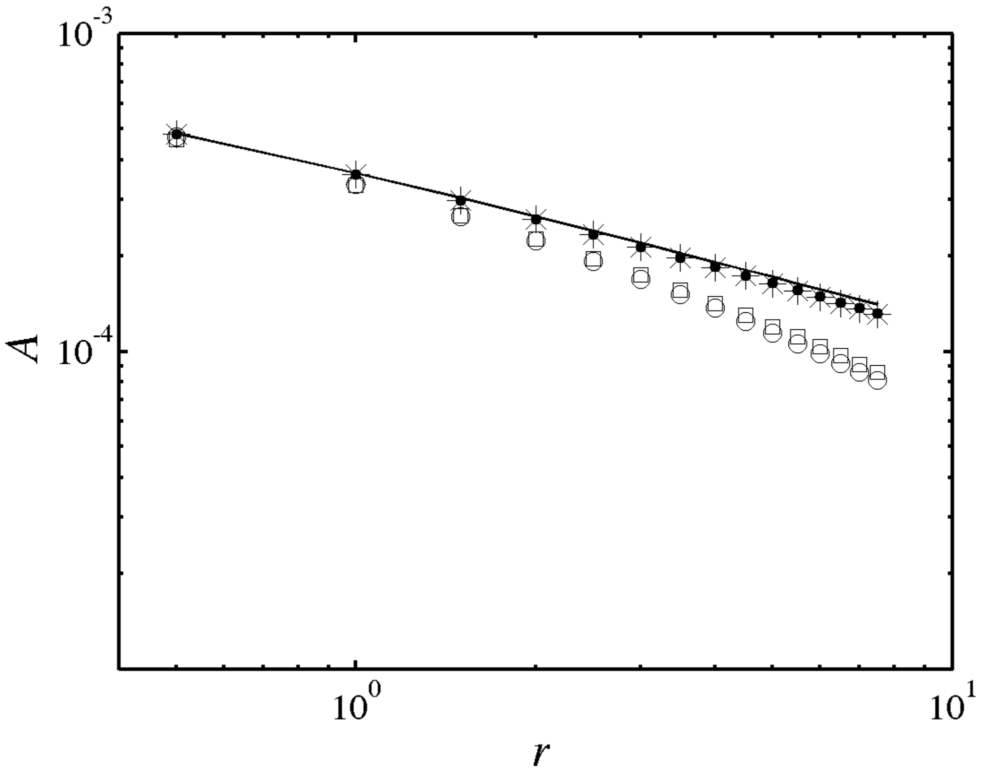

Figure 5.10 The variation of pressure peak amplitude with the radius of acoustic pulse travels. ————, analytical inviscid solution; * LBM (Re = 1000); ● DNS (Re = 1000); ○ LBM (Re = 100); □ DNS (Re = 100).

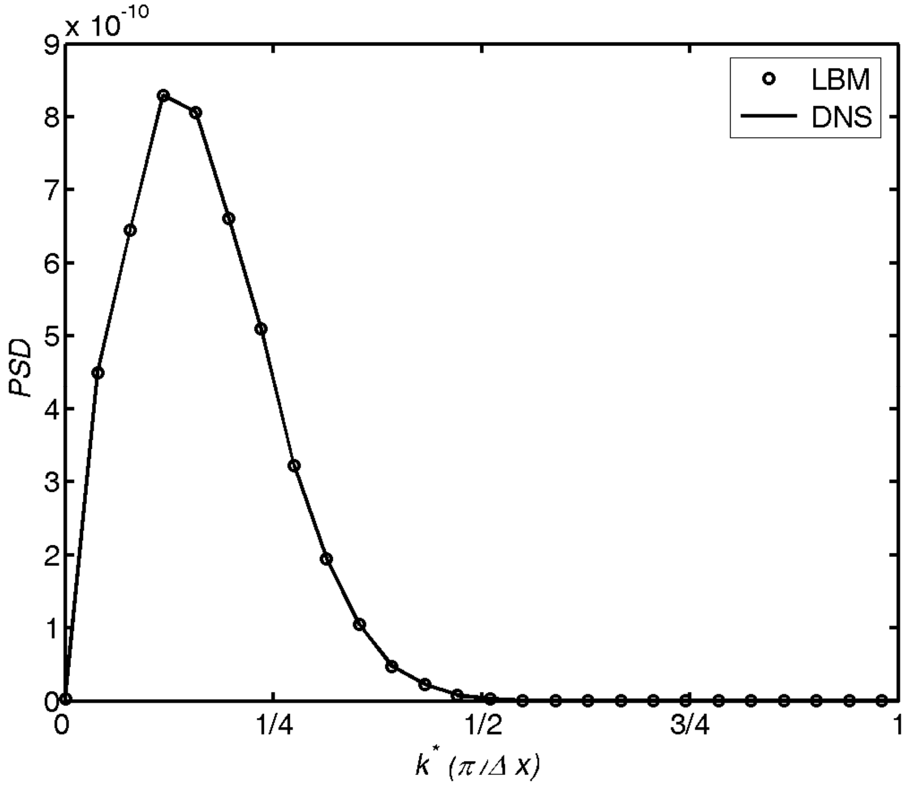

Figure 5.11 Power of spectrum density (PSD) of the effective wave-number k^* (normalized by $k_{\max} = \pi / \Delta x$).

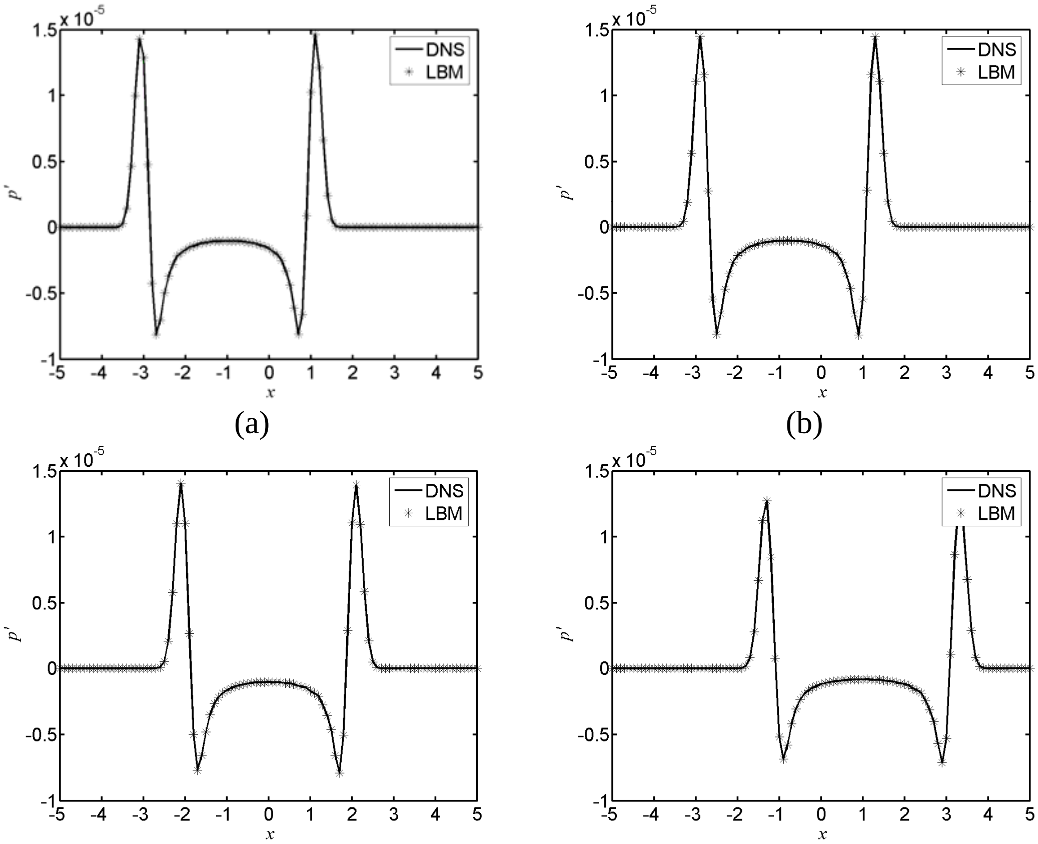

(a) (b)

(c) (d)

Figure 5.12 Instantaneous pressure fluctuations along the y-axis: (a) M = 0.01, *t* = 0.02; (b) M = 0.1, *t* = 0.2; (c) M = 0.5, *t* = 1.0; (d) M = 0.9, *t* = 1.8.

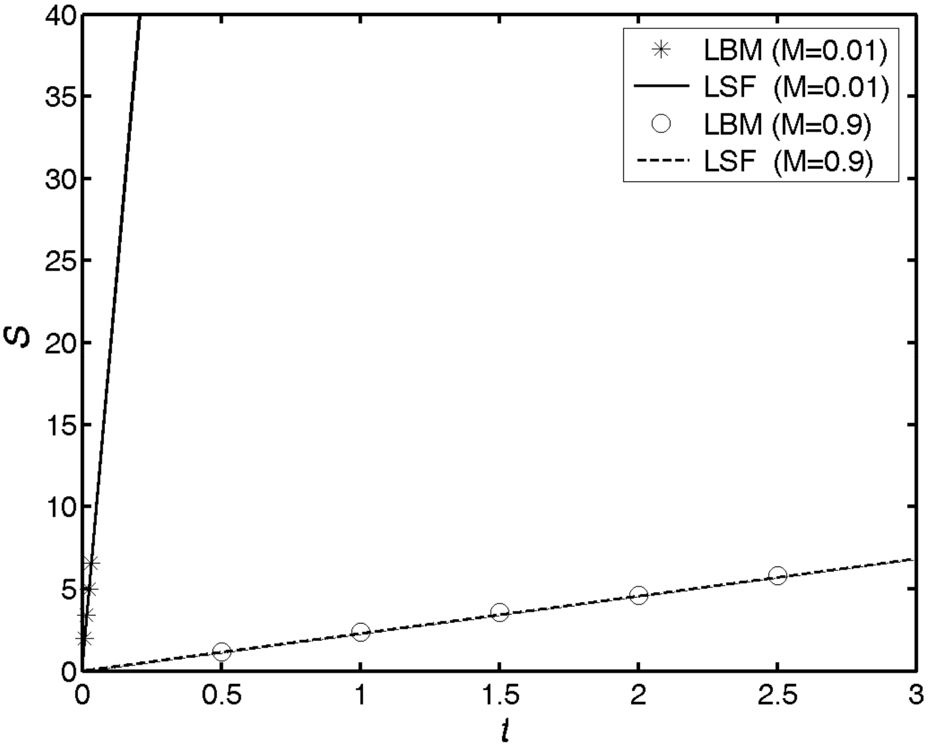

Figure 5.13 A plot of the distance S between two maximum peaks versus time *t*.

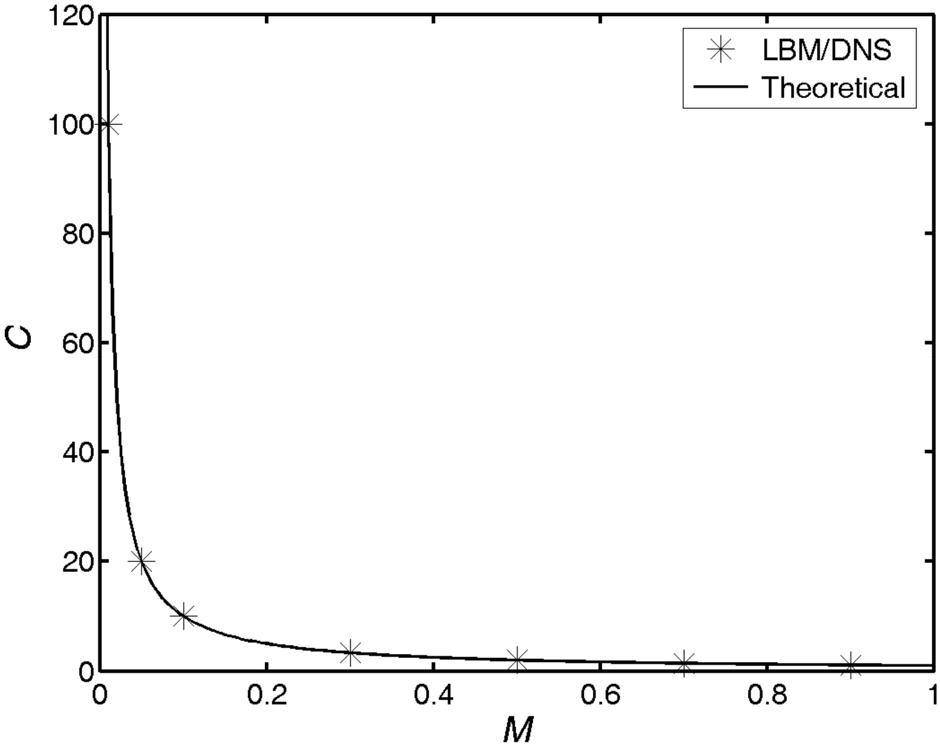

Figure 5.14 A plot of the propagation speed of sound $C = \sqrt{\gamma p / \rho}$ versus Mach number *M* and its comparison with its theoretical value.

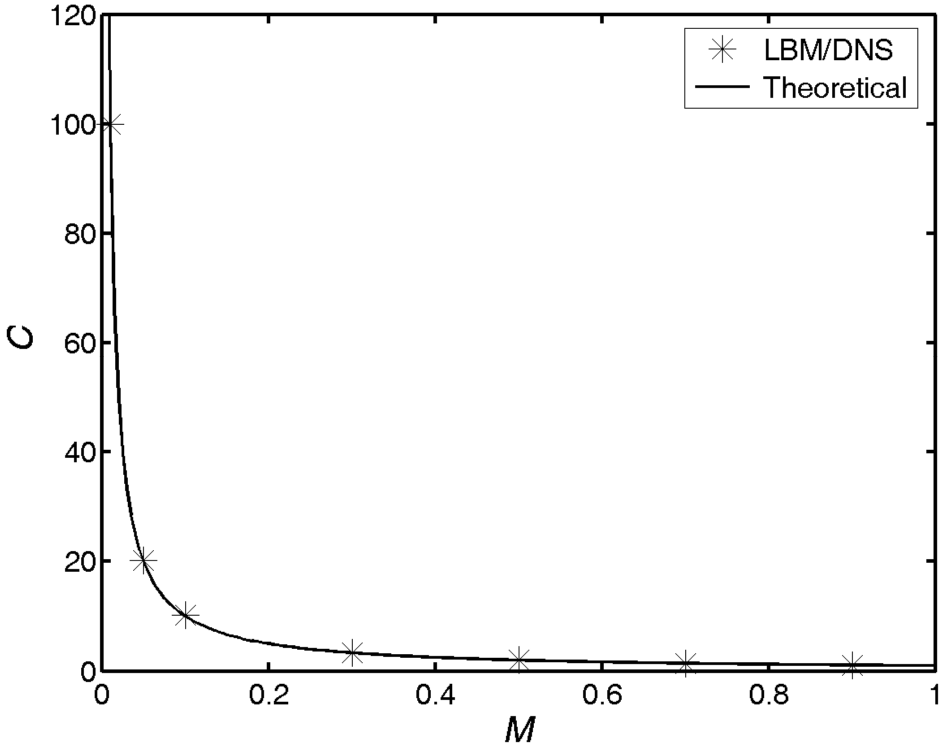

Figure 5.15 A plot of the propagation speed of the wave C versus Mach number M and its comparison with the theoretical value.

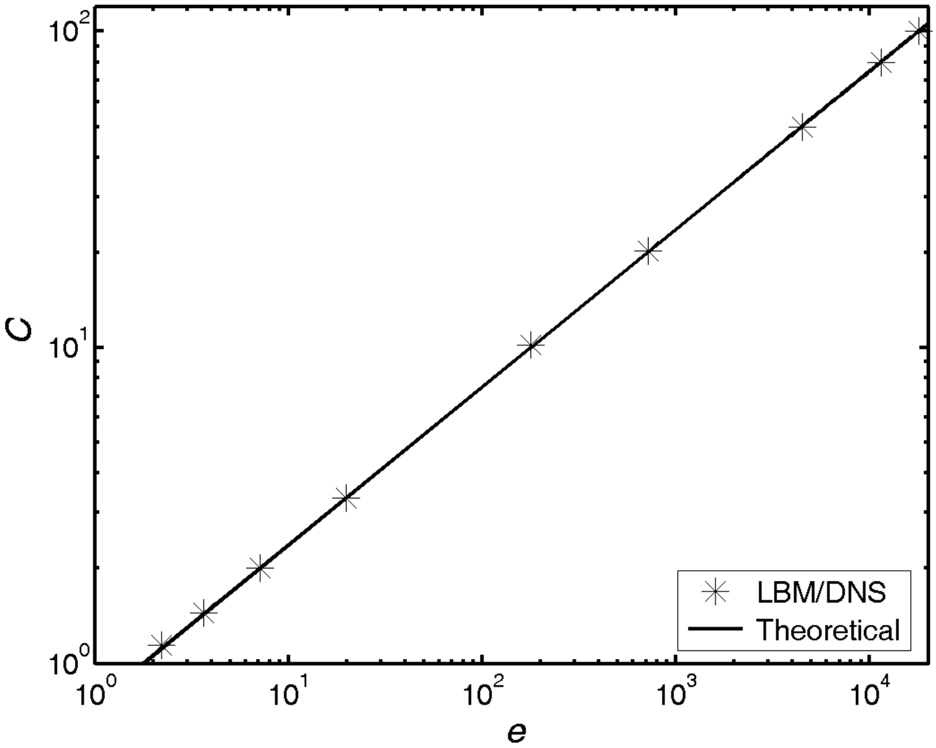

Figure 5.16 A plot of the internal energy *e* versus the propagation speed of sound C and its comparison with the theoretical value.

6 On the Calculation of Acoustic Directivity Using LBM

The LBM developed in Chapter 4 has been validated against the propagation of plane pressure pluses, circular pressure pulses, acoustic, entropy and acoustic pulses. In addition, the ability of the LBM to replicate isotropy property has also been validated against plane sinusoidal wave propagation in quiescent fluid. If the LBM is truly applicable for one-step aeroacoustic simulation, its ability to replicate acoustic directivity is necessary. Therefore, this chapter is devoted to an examination of the LBM and its ability to replicate acoustic directivity. The vehicle used is the scattering of plane sound waves by a zero circulation vortex. As before, two one-step aeroacoustic computational techniques; namely, DNS and LBM, are employed. Thus, the one-step LBM simulation can be validated against the DNS results, which have been shown to agree with the linear approximation results if the *M/Re* parameter is less or equal to 10^{-5} (Colonius et al. 1994). As mentioned in previous chapters, linear analysis of the Euler equations provides three basic aeroacoustic pulses in the flow; these are the entropy pulse, the vorticity pulse and the acoustic pulse. In the low Mach number regime, the flow is close to incompressible. Under this incompressible condition, only the vorticity pulse could exist. Therefore, the vorticity structures would dominate the whole flow. The scattering problem allows a direct investigation of the interaction between the acoustic field and the vortex, and could be used to explain the acoustic wave interaction with shear flows. If LBM can simulate this problem correctly, then it can deal with some other complicated aeroacoustic problems. The first part of this chapter will introduce the theoretical basis of this scattering problem. Then the short incident wave case will be calculated and presented.

6.1 Theoretical Work on Sound Scattering by a Zero Circulation Vortex

Fig. 6.1 shows a schematic drawing of the flow configuration in the two-dimensional system. Continuous small amplitude, plane sound waves with wavelength λ propagate in the positive direction of the *x*-axis in a uniform, homogeneous fluid. The wave impinges on a line (or "point") vortex of zero circulation lying along the *z*-axis that is normal to the plane where the vortex lies. This specification allows the vortex to approximate a rigid body of very small size. Therefore, the physical picture of this scattering problem is: when sound waves impinge upon this vortex, the vortex will oscillate with flow associated with the continuous waves. From vortex sound theory, this would lead to sound radiation. This picture is qualitatively correct, at least for long wavelength incident waves, the whole vortex is oscillating with continuous waves. For short wavelength incident waves, systematic formulations should be derived. The flow is supposed to be of very low Mach number, and the incident waves are supposed to be weak enough not to perturb the vortex (i.e., the vortex remains a rigid body).

Since the problem can be solved using a linear formulation, the dynamical quantities can be split into two parts (in vector form of primitive variables):

$$\mathrm{V} = \mathrm{V}_0 + \mathrm{V}_s \quad , \tag{6.1}$$

where subscript *0* refers to the background flow (in the absence of incoming sound), and *s* refers to the small correction due to the incoming sound. Similar to Lighthill's acoustic analogy, the resulting equation governing the scattering field can be derived, up to first order Mach number, it can be written as (Lund 2002, Fabrikant 1981):

$$\nabla p_s^2 - \frac{\partial^2 \rho_s}{\partial t^2} = S_1 = -2\rho_0 \frac{\partial^2 \left(u_j v_{si}\right)}{\partial x_i \partial x_j} \quad . \tag{6.2}$$

Eq. (6.2) can be analyzed using Fourier transform, which would explore the solutions in the frequency domain. In this two-dimensional system, taking the Fourier transform for the density and velocity gives

$$\rho(\mathbf{x}) = \frac{1}{(2\pi)^2} \int \tilde{\rho}(\mathbf{k}) e^{-i\mathbf{k}\cdot\mathbf{x}} d^2\mathbf{k} \quad , \tag{6.3a}$$

$$v_{si}(\mathbf{x}) = \frac{1}{(2\pi)^2} \int \tilde{v}_{si}(\mathbf{k}) e^{-i\mathbf{k}\cdot\mathbf{x}} d^2\mathbf{k} \quad , \tag{6.3b}$$

The solution for the scattering density can be obtained from Eq. (6.2) as

$$\tilde{\rho}_s(\mathbf{k}) = \frac{2\rho_0 k_i k_j}{(2\pi)^2 \left(\omega^2 - c^2 \mathbf{k}^2\right)} \int \tilde{u}_j(\mathbf{k} - \mathbf{k}') \tilde{v}_{si}(\mathbf{k}') d^2\mathbf{k}' \quad . \tag{6.4}$$

For the plane incident waves, velocity v_{si} and density fluctuations ρ_{si} can be approximated by using the incident wave characters, frequency ω, wave vector $\mathbf{k}_0$, velocity amplitude v_{si}^a and density amplitude ρ_{si}^a, thus

$$v_{si}(\mathbf{x}, t) = v_{si}^a \exp(i\omega t - i\mathbf{k}_0 \cdot \mathbf{x}) \quad , \tag{6.5a}$$

$$\rho_{si}(\mathbf{x}, t) = \rho_{si}^a \exp(i\omega t - i\mathbf{k}_0 \cdot \mathbf{x}) \quad , \tag{6.5b}$$

where $v_{si}^a = \frac{k_{0i} c^2}{\omega \rho_0} \rho_{si}^a$. Replacing these values in Eq. (6.4), the scattering density in a polar coordinate system ($x = r\cos\theta,\ y = r\sin\theta$) can be finally written as,

$$\frac{\rho_s(\mathbf{x}, t)}{\rho_{si}^a} = f(\theta) r^{-1/2} \exp(i\omega r / c) \quad , \tag{6.6}$$

where $f(\theta) = \frac{\sin\theta\cos\theta}{\cos\theta - 1}\tilde{\Omega}(\mathbf{k} - \mathbf{k}_0)$ is the directivity function and is independent of frequency, $\tilde{\Omega}$ is the Fourier transform of the voriticity distribution. If this vorticity Fourier transform is expanded and only keeping the highest order, the directivity function can be expressed as (Fabrikant 1983)

$$f(\theta) = \frac{\sin\theta\cos\theta}{\cos\theta - 1}\left[\tilde{\Omega}_y(\cos\theta + 1) - \tilde{\Omega}_x \sin\theta\right] \quad . \tag{6.7}$$

where $\tilde{\Omega} = \int \mathrm{r}\omega(\mathrm{r})d\mathrm{r}$. Once the vorticity distribution is known, Ω can be integrated and then the directivity of the acoustic scattering can be calculated.

6.2 Computations of Sound Scattering by a Zero Circulation Vortex

This problem can be normalized by the mean fluid quantities such as density ρ_0, speed of sound c_0 and temperature T_0. The characteristic length is defined by the size L_0 of the vortex. With this normalization, two constants will result; one is the Reynolds number defined as $Re = \rho_0 c_0 L_0 / \mu_0$ while another is the Mach number defined as $M = u_m / c_0$. Here, u_m is the maximum angular velocity of the vortex.

The strength of the scattering field is very weak; mostly it is 2 orders less than the incoming waves, which are already of acoustic strength. Thus the scattering field is always submerged inside the background of the continuous waves. A better way to study this problem is to show the difference between these two cases. The first case is to calculate the single vortex pulse plus continuous waves. The second case only introduces continuous waves in the same computational domain. Then the difference between these two cases can be viewed as the effect due to the vortex pulse. On the other hand, the initial vortex would also create some waves propagating outwards; the effect of this part should also be considered in the scattering field.

The numerical simulations are very difficult because of great disparities in scales in this problem. Firstly, the incident acoustic waves are at least three-orders less than the mean flow quantities, and the scattered wave amplitude is usually two orders smaller than the incident sound wave amplitude. Non-reflecting numerical boundaries are needed in both DNS and LBM simulations. For DNS, the boundary method follows the arrangement given in §3.4, where an absorbing buffer zone is invoked for the left hand side and the right hand side open boundaries, and NSCBC method is applied to the upper and lower open boundaries. For LBM, a buffer technique is also invoked for the left hand side and right hand side but in the manner of absorbing the fluctuations of *f*. For the upper and lower boundaries, a simple continuity for the gradient of *f*, i.e., $\partial f / \partial n$ is used. The solution proves that this simple method works well for this problem and there are no conspicuous errors found from these boundaries. Thus, altogether three cases are calculated before the scattering field can be valued: (i) only continuous waves, (ii) only vortex pulse, (iii) continuous waves plus vortex pulse.

To achieve a correct solution for the scattering, the LBM should calculate these three cases correctly. The solutions of case 1 to case 3 would be compared with DNS respectively.

6.2.1 Only Continuous Waves

These plane sound waves would be excited in the -*x* region. The sound waves are excited at $x = x_e$ (Fig. 6.2) and the calculations are following the excitations Eq. (3.5) (§ 3.4) and Eq. (5.5) (§ 5.3) for DNS and LBM, respectively. In §5.3, plane sinusoidal wave propagation in quiescent fluid has already been studied and compared with DNS solutions. Good agreement achieved between LBM and DNS, so this comparison would not be repeated here.

6.2.2 Only Vortex Pulse

Vorticity distribution plays an important role in this scattering problem. In the theoretical derivation, it was found that the scattering field was related to the Fourier transform of the vorticity distribution. Thus, correct representation of a single vortex pulse by LBM is very important. In this case, a single vortex pulse is calculated by LBM and DNS. In the previous derivations, it is noted that the integration of vorticity on the whole volume should vanish so the Green's function can be used to integrate the integral to yield a solution. In this two-dimensional case, this is essentially the consequence of a zero circulation vortex. The definition for a zero circulation vortex or Taylor vortex (Berthet et al. 2000) is given by

$$\omega(\mathrm{r}) = \omega_0\left[2-(r/L_0)^2\right]\exp\left[\frac{1-(r/L_0)^2}{2}\right] \quad , \tag{6.8}$$

where ω_0 is the characteristic vorticity strength that would dominate the corresponding Mach number, L_0 is the characteristic length for this vortex. This is the vortex considered in the problem and used throughout the computations. So in the computations, the initial vortex is given by:

$$\rho = 1\,,\ u = u_m\, y \exp\left\{\frac{1-r^2}{2}\right\},\ v = -u_m\, x \exp\left\{\frac{1-r^2}{2}\right\},\ p = 1/\gamma \quad . \tag{6.9}$$

Fig. 6.3a and Fig. 6.3b show the contours of "u" and "v" respectively by using LBM when time equal to 5. Fig. 6.4a and Fig. 6.4b show the same plots by using DNS. Fig. 6.5 shows the "u" distribution along a 45^o line which is cross the center of the vortex, the solid line is the reference (DNS), the stars are for LBM. All these plots show that good agreement achieved between LBM and DNS. Thus LBM and DNS give the same result for this single vortex.

6.2.3 Continuous Waves Plus Vortex Pulse

In this case, the waves were excited once previous Taylor vortex is initialized in the center of the domain. Because the scattering field is very small compare to the incoming waves, mostly 2 orders less than the strength of the continuous waves. The effect of this scattering could be obtained by subtracting two solutions, that is, $\rho_s = \rho_{v+w} - \rho_w$, where the subscript $(v+w)$ indicates the condition of vortex plus sound waves, and w indicates sound waves only (Case 1).

Fig. 6.6a and Fig. 6.6b are the scattering fields (density contours) for the $\lambda = 2$ condition. Both DNS and LBM solutions show similar directivity for the scattering field. That is, for the $\lambda = 2$ condition, most of the scattering energy is inside a short angle between *x*-axis, and no clear backward scattering (propagating to –*x* direction) is found.

Since the directivity function has been derived for Eq. (6.7), it can be seen that the scattering energy along certain direction should be also distributed according to this angular function. Thus, for each point, the root-mean-square of the scattering density should be proportional to this function, which can be written as:

$$\rho_s^{rms}(\mathrm{x},t) \propto \left| f(\theta) \right| \quad . \tag{6.10}$$

Therefore, the directivity feature of sound scattering by a zero circulation vortex can be compared with this theoretical result. The root-mean-square scattering density is calculated by recording 20 equal time interval solutions in one cycle of the excitation waves, for each point, the computational root-mean-square value is calculated from:

$$\rho_s^{rms} = \sqrt{\frac{\sum_i \rho_{si}^2}{20}}, \; (i=1, \ldots, 20) \quad . \tag{6.11}$$

This root-mean square value is plotted in Fig. 6.7 for the $\lambda = 2$ case versus scattering angle. The solid line is the theoretical solution derived from Eq. (6.7) with a known vorticity distribution given by

$$\omega(\mathrm{r}) = \omega_0 \left[2 - (r / L_0)^2\right] \exp\left[\frac{1 - (r / L_0)^2}{2}\right] \quad . \tag{6.12}$$

Both DNS and LBM solutions are approaching the theoretical values. A good agreement is found between numerical simulations and theoretical distributions. The major difference is near the angle of $-\pi/10$, where the DNS solution is close to 6.578e-8, but LBM gives 5.849e-8 at the same angle. The maximum error is close to 11% for the scattering field. Even this error shows LBM hasn't achieved a good result as DNS did, but in the sense of 8 orders less than the mean quantities, LBM has already gives a good result for scattering case. The future improvement of LBM model maybe can fix this problem. It means that the current LBM scheme can simulate sound and vortex interactions correctly, so it can handle other aeroacoustic problems besides those discussed in Chapter 5 as well.

6.3 Summary

In this chapter, sound scattering by a zero circulation vortex was investigated. The first part of this chapter reviewed theoretical work for this problem, especially for the two-dimensional zero circulation vortex condition. The final expression of the scattering solution indicated a directivity term that would distribute the scattering energy in certain directions. Since most of the scattering waves are much weaker than the incoming sound waves, the directivity feature of this problem presents a challenge for the ability of the one-step CAA schemes. Correct computations should reveal the scattering field whose strength is two or three orders of magnitude less than the incoming waves. Furthermore, the solutions should have the same directivity distributions so the interaction between sound and vortex is correctly reproduced. All the one-step numerical solutions reported in the second part of this chapter show that the present LBM scheme could simulate the interaction problems correctly much the same as those given by the DNS scheme.

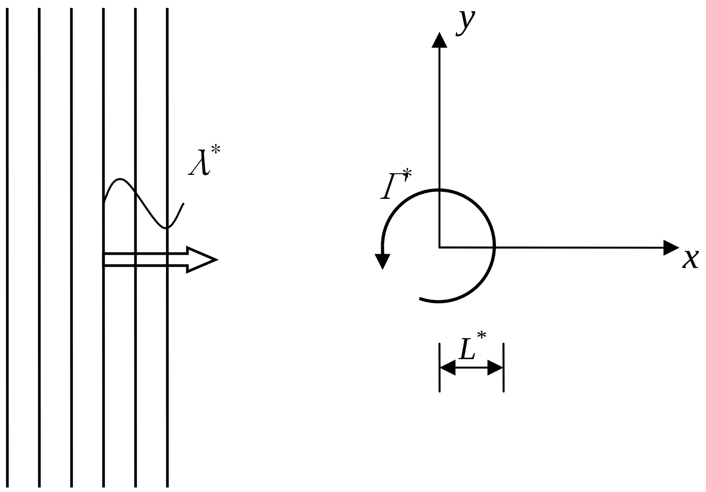

Figure 6.1 Schematic diagram of flow configuration.

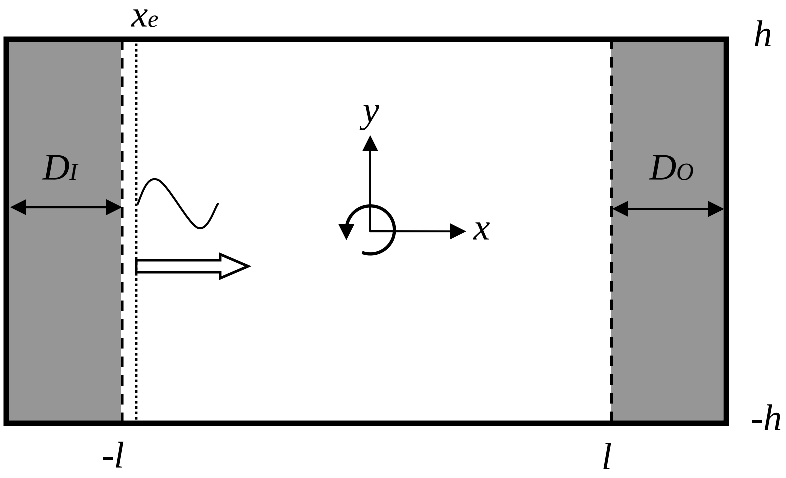

Figure 6.2 Specification of computations for sound scattering by vortex.

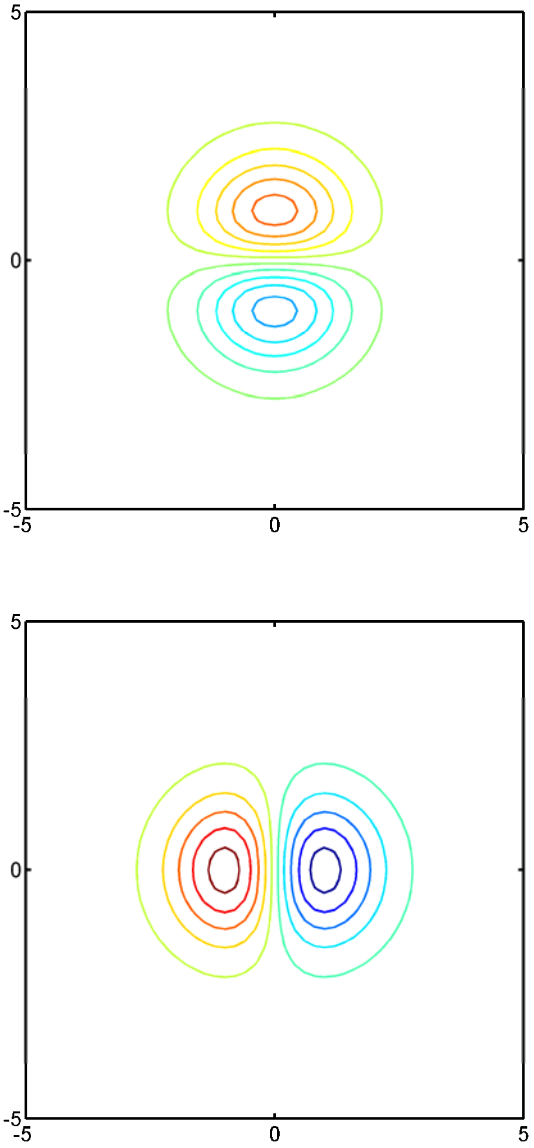

Figure 6.3 Velocity contours of single vortex pulse by LBM computation: (a) “u”; (b) “v”.

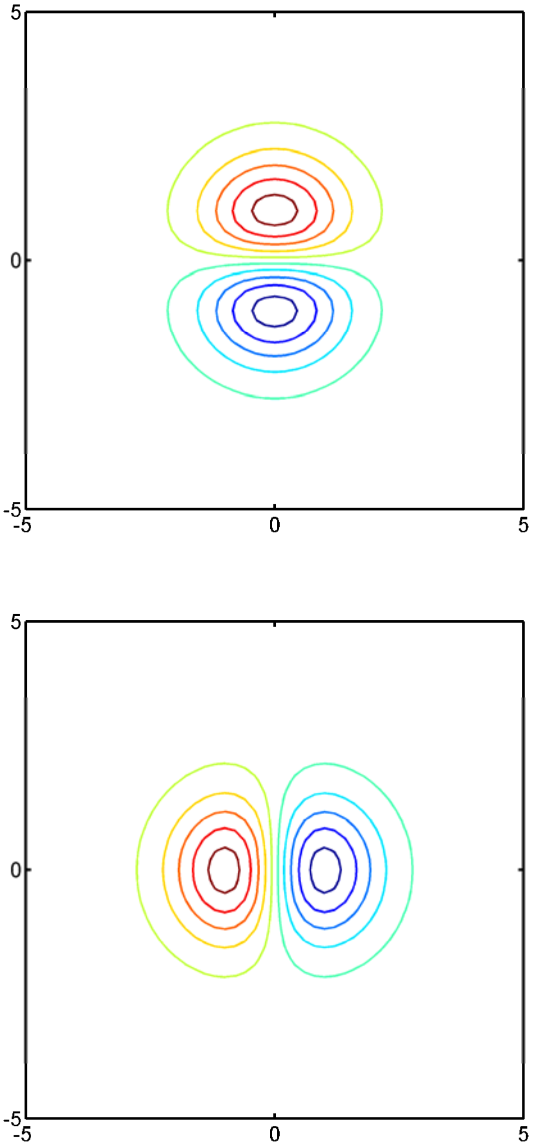

Figure 6.4 Velocity contours of single vortex pulse by DNS computation: (a) “u”; (b) “v”.

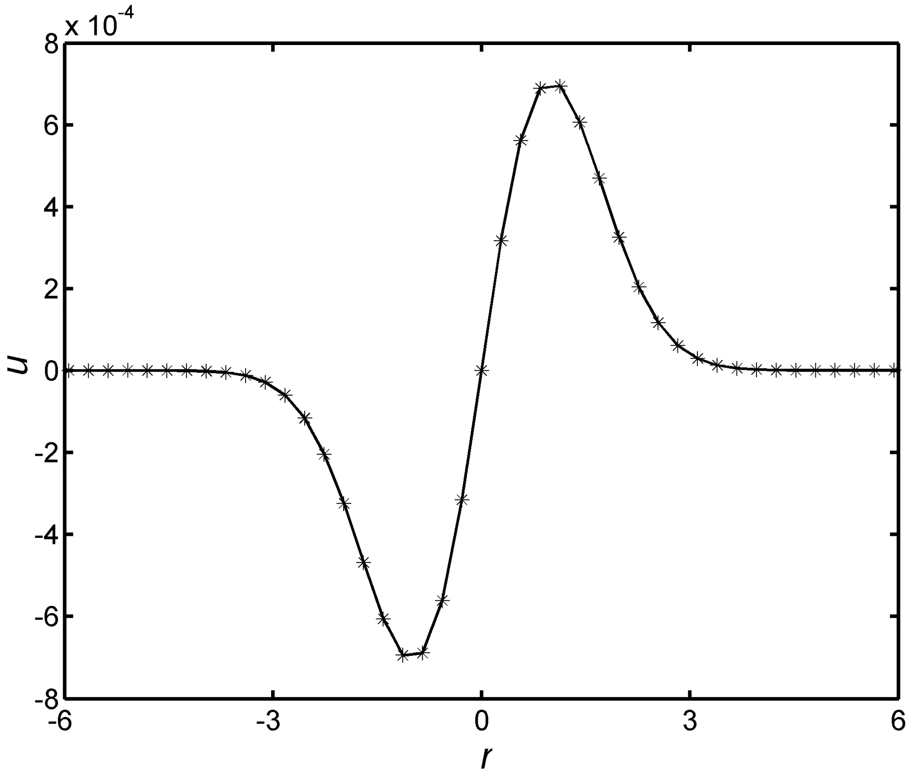

Figure 6.5 Distribution of “u” along a 45^o line which is cross the center of vortex: stars for LBM, solid line for DNS.

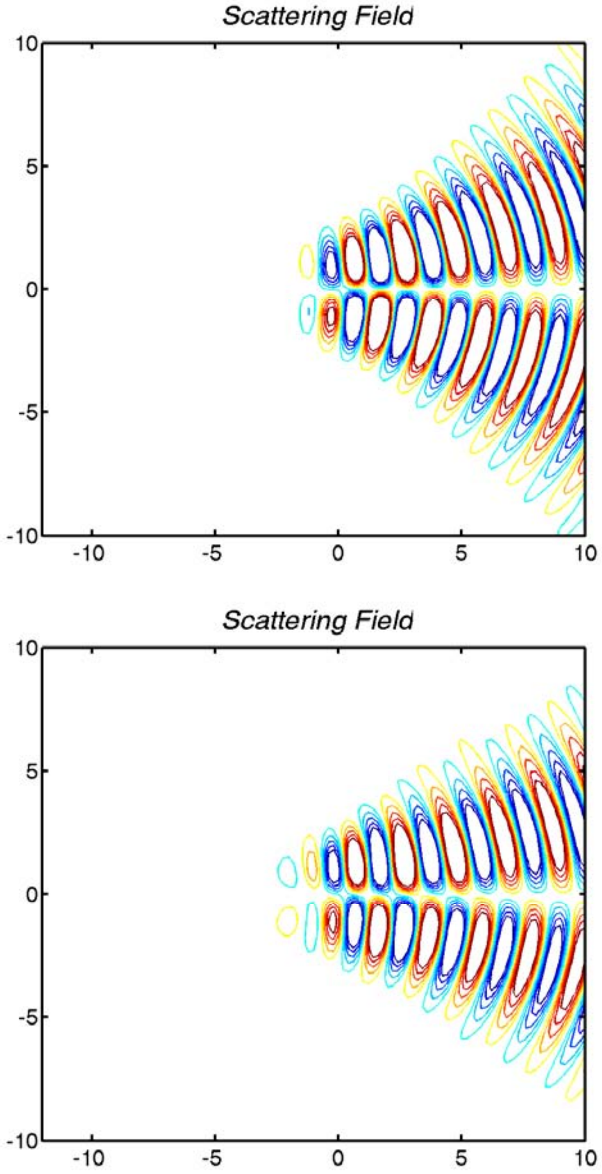

Figure 6.6 Scattering field (density contours) for short wave length $\lambda = 2$ (a) DNS; (b) LBM.

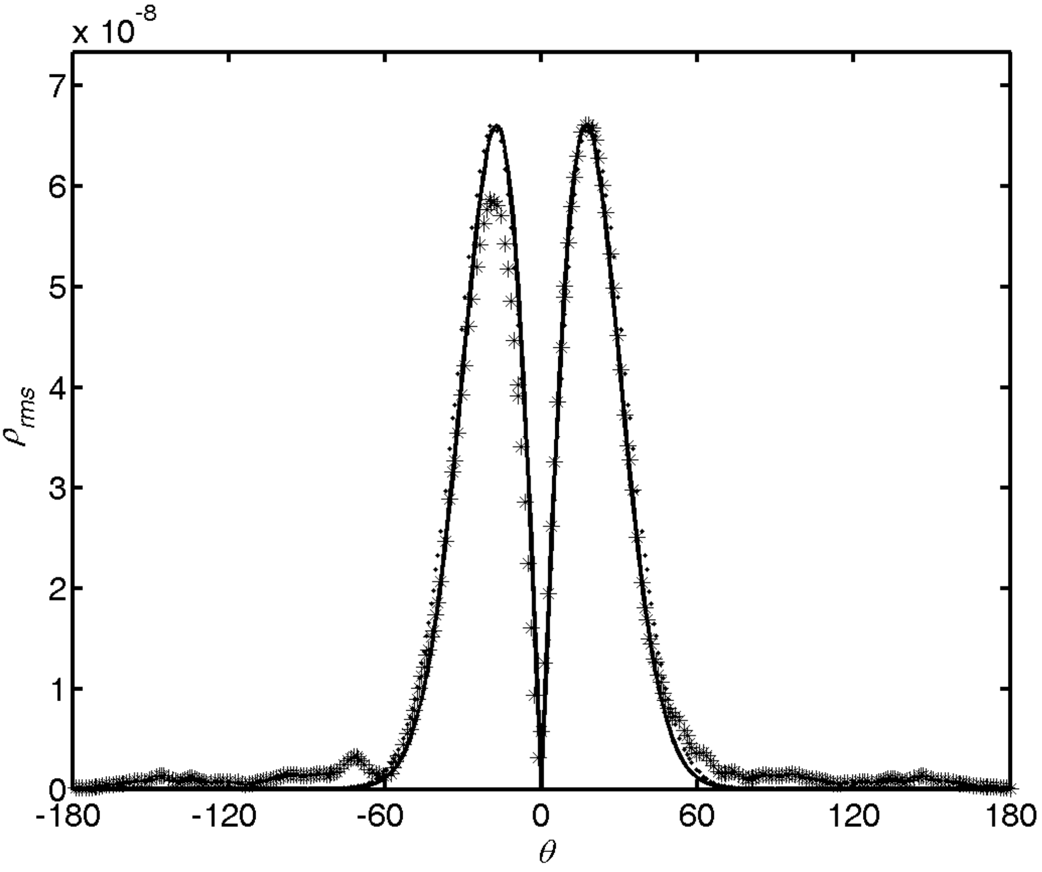

Figure 6.7 Directivity of the scattering for short wave length condition $\lambda = 2$, ● for DNS; * for LBM, solid line is the theoretical distribution.

7 Conclusions

In this thesis, a new one-step CAA scheme is derived based on an improved modeled Boltzmann equation solved using the lattice Boltzmann method and validated against various benchmark aeroacoustic problems. In order to validate the improved LBM scheme, an established one-step CAA scheme based on the direct numerical simulation (DNS) of the unsteady compressible Navier-Stokes equations (DNS) is introduced and validated against some basic aeroacoustic pulses. Then the improved BE solved is shown to recover the fully unsteady compressible Navier-Stokes equations, including the correct recovery of the fluid first coefficient of viscosity and the specific heat ratio for diatomic gases. Assuming the benchmark solutions derived from DNS to be reliable and correct, the LBM computations are compared with these solutions and theoretical results whenever available.

The work of this thesis is divided into two parts. The first part is to recover the fully unsteady compressible Navier-Stokes equation from the improved BE and numerically validate the resulting formulation against benchmark aeroacoustic problems. This is not simply to repeat previous work on the study of the Boltzmann equation. The approach taken is to invoke a two-relaxation time model for the collision term and using the second relaxation time to correctly recover the first coefficient of viscosity by requiring the derived relation between viscosity and temperature to replicate the Sutherland law. In addition, the gas equation of state and the specific heat ratio is recovered correctly by taking into consideration the effect of rotational energy for diatomic gases. It should be emphasized that these assumptions and derivations have strong physical background. This part is essentially theoretical and is able to demonstrate that the improved BE can be used to calculate gas flow where the viscosity, specific heat ratio and speed of sound are recovered correctly; thus the resulting equation could be used to carry out direct computations of one-step aeroacoustic problems.

The second part of this thesis focuses on the numerical validation of the improved LBM. The DNS computations give benchmark solutions for the LBM validation. A series of basic aeroacoustic pulses are calculated using DNS and LBM, and the results are compared with each other and with theoretical solutions whenever available. These include single pressure pulses (1-D and 2-D), continuous pulses, three different (pressure, vorticity and entropy) pulses in a mean flow and recovery of the speed of sound in different Mach number flows. The results show that improved LBM can calculate these pulses correctly. In order to demonstrate that the improved LBM can also replicate the calculation of sound directivity correctly in an aeroacoustic problem much like the DNS does, a final validation is carried out for a sound-vortex scattering problem. This case is used to test the ability of the improved LBM to replicate the interaction between acoustics and aerodynamics. In all these comparisons, the improved LBM results show good agreement with conventional DNS simulations. Therefore, the viability of the improved LBM scheme as an alternative to the DNS scheme for one-step CAA is established.

Furthermore, due to the simple form of the improved BE, the proposed one-step LBM CAA scheme has certain advantages compared to the DNS method. A major advantage is the simplicity of the LBM code. In DNS, the governing equations are the fully unsteady compressible Navier-Stokes equations. These equations consider the continuity of mass, momentum and energy of the medium under the continuum assumption. However, with only the continuum assumption, the viscous stress and heat transfer terms in these equations could not be evaluated.

Only after invoking the Stokes stress hypothesis and the Fourier law, which are derived from particle collision theory, these higher-order transport terms can be related to viscosity and thermal conductivity, respectively. At the same time, the computer codes used to solve these governing equations become complicated because the transport terms are related to second-order spatial derivatives, and parallel computation could not be easily and fully made used of. Therefore, computational time is an important consideration in one-step CAA using the DNS method. Using the improved LBM scheme, the governing equation only involves first-order spatial derivatives and a simply model for the collision term. For a simple rectangular computational domain, a DNS code needs about 1350 lines (in Fortran language) whereas the improved LBM code only needs about 420 lines. Besides, the simple structure of the LBM code is readily amenable to parallel computation which means a reduction in computation time is possible. These advantages mean that the LBM code could be easily put together and could be extended to cover irregular domains (e.g., cavity, backward-facing step or other discontinuity inside tubes).

A second advantage is that the improved LBM has a high-order numerical boundary. This advantage could be a consequence of the highly-conservative particles in the Boltzmann equation. It should be noted that, in DNS computations, the spurious waves are mostly coming from the numerical boundaries. When approaching the numerical boundaries, a different formulation has to be used to calculate the spatial derivatives; conventionally a 6th-order compact scheme is used for inner points away from the boundaries while a 4th-order upwind scheme is usually assumed for the boundary points. In a DNS scheme where the Navier-Stokes equations are solved, the conservative variables are strongly depending on these spatial derivatives. If the computational values for these derivatives are not correct, spurious waves could develop at the boundaries. From the numerical point of view, the conservation of mass, energy and energy flux are incorrectly estimated at the boundaries. This puts a great burden on the boundary method in DNS simulations. In particular, this is true for purely non-reflecting boundaries; some complex techniques (NSCBC, PML and absorbing BC) have been introduced but they are not easy to implement into the computer code. In a LBM formulation, the original Boltzmann equation already has a high-conservation feature for the particles built in; therefore, conservation of primitive variables is quite independent of spatial derivatives. Thus, even if the same set of compact scheme is used to solve the improved BE and errors for the spatial derivatives result, conservation laws for the particles are still in compliance. This means that non-reflecting boundary conditions could be very simple for any LBM scheme. Even a relatively simple first-order continuity of the particle distribution function could give good non-reflecting property at the computational boundary. This would lead to a reduction of computational time since a smaller domain can be used in improved LBM.

On the other hand, there are certain disadvantages in the improved LBM compared to the DNS. Firstly, the computational time-step is too small, especially for high Reynolds number flows. In DNS scheme, the time-step is governed by the CFL condition which can be expressed as $\Delta t \le \left(\Delta x, \Delta y\right)_{\min} / 3c$, where $\left(\Delta x, \Delta y\right)_{\min}$ is the minimum value of the grid sizes, c is the speed of sound. This formulation is independent of the viscosity. For LBM, the time-step should be smaller than half of the relaxation time. The relaxation time is related to the viscosity and hence the Reynolds number, so the time-step for LBM is affected by the Reynolds number of the flow. For high Reynolds number flows, the time-step has to be very small. Secondly, other transport coefficients of the gases are still not recovered correctly.

An example is the Prandtl number. A theoretical derivation is needed to recover the correct Prandtl number for air. Once all these features for air are recovered correctly, the LBM could be used to simulate more complicated aeroacoustic problems.

This one-step CAA scheme using the improved LBM is new. Unlike the DNS scheme where the equation of state and the speed of sound have to be specified, these two properties are part of the solutions in the LBM formulation. Existing LBM schemes in the literature fail to reproduce these two properties correctly and are not suitable for aeroacoustic problems. The improved LBM scheme proposed in this thesis is the first step towards deriving a true one-step CAA based on the improved BE.

REFERENCES

Abarbanel S. and Gottlieb D., 1997, “A Mathematical Analysis of the PML Method,” *Journal of Computational Physics*, **134**, 357-363.

Abarbanel S., Gottlieb D. and Hasthaven J. S., 1999, “Well-posed Perfectly Matched Layers for Advective Acoustics,” *Journal of Computational Physics*, **154**, 266-283.

Agarwal A., Morris P.J. and Mani R., 2004, “Calculation of Sound Propagation in Nonuniform Flows: Suppression of Instability Waves,” *AIAA Journal*, **24**, No. 1, January.

Aidun C.K., Lu Y-N, 1995, “Lattice Boltzmann Simulation of Solid Particles Suspended in Fluid,” *Journal of Statistical Physics*, **81**, 49-61.

Armaly B.F., Durst F., Pereira J.C.F. and Schönung B., 1983, “Experimental and Theoretical Investigation of Backward-Facing Step Flow,” *Journal of Fluid Mechanics*, **127**, 473-496.

Atvars J., Schubert L.K., Ribner H.S., 1965, “Refraction of Sound from a Point Source Placed in an Air Jet,” *J. Acoust. Soc. Am.*, **37**, 168.

Behrend O., 1995, “Solid-fluid Boundaries in Particle Suspension Simulations via the Lattice Boltzmann Method,” *Physical Review E*, **52**, 1164-1175.

Berenger J.P., 1994, “A Perfectly Matched Layer for the Absorption of Electromagnetic Waves,” *Journal of Computational Physics*, **114**, No. 2, 185-200.

Berthet R., Astruc D., Estivalezes J.L., 2000, “Assessment of Numerical Boundary Conditions for Simulation of Sound Scattering by Vorticity,” AIAA-2000-2005.

Betchelor G.K., 1970, *An Introduction to Fluid Dynamics*, Cambridge, University Press, New York.

Bhatnagar P., Gross E.P. and Krook M.K., 1954, “A Model for Collision Processes in Gases, I. Small Amplitude Processes in Charged and Neutral One-Component Systems,” *Physical Review*, **94**, No. 3, 515–525.

Bogey C. and Bailly C., 2004, “A Family of Low Dispersive and Low Dissipative Explicit Schemes for Flow and Noise Computations,” *Journal of Computational Physics*, **194**, 194-214.

Bruggeman J.C., Hirschberg A., Van Dongen M.E.H., Wijnands A.P.J., and Gorter J., 1991, “Self-sustained Aeroacoustic Pulsations in Gas Transport Systems: Experimental Study of the Influence of Closed Side Branches,” *Journal of Sound and Vibration*, **150**, No. 3, 371-393.

Casper J., 1996, “Using High-Order Accurate Essentially Nonoscillatory Schemes for Aeroacoustic Application,” *AIAA Journal*, **34**, No. 2, 244-250.

Cercignani C., 1975, *Theory and Application of the Boltzmann Equation*. Scottish Academic Press.

Chapman S. and Cowling T. G., 1970, *The Mathematical Theory of Non-Uniform Gases*, Cambridge University Press.

Chen H., Chen S. and Matthaeus W.H., 1992, “Recovery of the Navier-Stokes Equations Using a Lattice-Gas Boltzmann Method,” *Physical Review A*, **45**, 1992, 5339–5342.

Chen S., Dawson S.P., Doolen G.D., Janecky D.R., Lawniczak A., 1995, “Lattice Methods and their Applications to Reacting Systems,” *Computational Chemistry Engineering*, **19**, 617-646.

Chen S. and Doolen G.D., 1998, “Lattice Boltzmann Method for Fluid Flows,” *Annual Review of Fluid Mechanics*, **30**, 329–364.

Chiang, T. P., Sheu, T. W. H. and Fang, C. C., 1999, "Numerical Investigation of Vertical Evolution in a Backward-Facing Step Expansion Flow", *Applied Mathematical Modelling*, **23**, 915-932.

Chung T.J., 2002, *Computational Fluid Dynamics*, Cambridge, Cambridge University Press, New York.

Colonius T. and Lele S.K., 2004, "Computational Aeroacousitcs: Progress on Nonlinear Problems of Sound Generation," *Progress in Aerospace Sciences*, **40**, 345-416.

Colonius T., Lele S.K. and Moin P., 1993, "Boundary Conditions for Direct Computation of Aerodynamic Sound Generation," *AIAA Journal*, **31**, No. 9, 1574-1582.

Colonius T., Lele S.K. and Moin P., 1994, "The Scattering of Sound Waves by a Vortex: Numerical Simulations and analytical solutions," *J. Fluid Mech.*, **260**, 271-298.

Davies P.O.A.L., 1988, "Practical Flow Duct Acoustic," *Journal of Sound and Vibration*, **124**, 91-115.

Dawson S.P., Chen S., Doolen G.D., 1993, "Lattice Boltzmann Computations for Reaction-diffusion Equations," *Journal of Chemistry Physics*, **98**, 1514-1523.

Enquist B. and Majda A., 1977, "Absorbing Boundary Conditions for the Numerical Simulation of Waves," *Mathematics of computation*, **31**, No. 139, 625-651.

Fabrikant A.L., 1983, "Sound Scattering by Vortex Flows," Sov. Phys. Acoust., **29**, 2.

Ferziger J.H. and Kaper H.G., 1975, *Mathematical Theory of Transport Processes in Gases*, North-Holland.

Ferziger J.H. and Peric M., 1999, *Computational Methods for Fluid Dynamics*, Berlin, Hong Kong, Springer, Chapter 5.

Ffowcs-Williams J.E. and Hawkings D.L., 1969, “Sound Generation by Turbulence and Surfaces in Arbitrary Motion,” *Philosophical Transactions of the Royal Society of London, Series A, Mathematical and Physical Sciences*, **264**, No. 1151, 321-342.

Filippova O. and Hänel D., 2000, “A Novel Lattice BGK Approach for Low Mach Number Combustion,” *Journal of Computational Physics*, **158**, 139-160.

Freund J.B., 1997, “Proposed Inflow/Outflow Boundary Condition for Direct Computation of Aerodynamic Sound,” *AIAA Journal*. **35**, No. 4, 740–742.

Freund J.B., 2000, “A Simple Method for Computing Far-Field Sound in Aeroacoustic Computations,” *Journal of Computational Physics*, **157**, 796-800.

Frisch U., d’Humières D., Hasslacher B., Lallemand P., Pomeau Y., Rivet J.–P. and Pomeau Y., 1987, “Lattice Gas Hydrodynamics in Two and Three Dimensions,” *Complex Systems*, **1**, 649–707.

Frisch U., Hasslacher B. and Pomeau Y., 1986, “Lattice-Gas Automata for the Navier-Stokes Equation,” *Physical Review Letters*, **56**, 1505–1508.

Gaitonde D.V. and Visbal M.R., 1999, “Further Development of a Navier-Stokes Solution Procedure Based on Higher-Order Formulas,” *AIAA paper*, 99-0557.

Giles M.B., 1990, “Nonreflecting Boundary Conditions for Euler Equation Calculations,” *AIAA Journal*, **28**, No. 12, 2050-2058.

Gloerfelt, X., Bailly, C. and Juvé, D., 2003, “Direct Computation of the Noise Radiated by a Subsonic Cavity Flow and Application of Integral Methods,” *Journal of Sound and Vibration*, **266**, 119–146.

Goldstein M.E., 1976, *Aeroacoustics*, McGraw-Hill Inc., New York.

Grande E., 1965, “Refraction of Injected Sound by a very cold Nitrogen Jet”, *J. Acoust. Soc. Am.*, **38**, 1063.

Grinstein F.F., 1994, “Open Boundary Conditions in the Simulation of Subsonic Turbulent Shear Flows,” *Journal of Computational Physics*, **115**, 43-55.

Grunau D., Chen S., Eggert K., 1993, “A Lattice Boltzmann Model for Multiphase Fluid Flows,” *Physical Fluids A*, **5**, 2557-2562.

Gunstensen A.K., Rothman D.H., 1993, “Lattice Boltzmann Studies of Immiscrible Two Phase Flow through Porous Media,” Journal of Geophysical Research, **98**, 6431-6441.

Guo A., Shi B. and Wang N., 2000, “Lattice BGK Model for Incompressible Navier-Stokes Equation,” *Journal of Computational Physic*, **165**, 288-306.

Guo, Z.L., Zhao T.S., 2002, “Lattice Boltzmann Model for Incompressible Flows through Porous Media,” *Physical Review E*, **66**, No. 036304.

Hall D.E., 1987, *Basic Acoustics*, Harper & Row, New York.

Harris S., 1999, *An Introduction to the Theory of the Boltzmann Equation*, Dover Publications, Inc.

Hassall J.R. and Zaveri K., 1979, *Acoustic Noise Measurements*, Brüel & Kjær, Naerum, Denmark.

He X. and Doolen D., 1997, “Lattice Boltzmann Method on Curvilinear Coordinates System: Flow around a Circular Cylinder,” *Journal of Computational Physics*, **134**, 306-315.

He X. and Luo L.–S., 1997, “Theory of the Lattice Boltzmann Method: From the Boltzmann Equation to Lattice Boltzmann Equation,” *Physical Review E*, **56**, No. 6, 6811–6817.

Hesthaven J.S., 1998, “On the Analysis and Construction of Perfectly Matched Layers for the Linearized Euler Equations,” *Journal of Computational Physics*, **142**, 129-147.

Hirschberg A. and Schram C., 2002, "A Primitive Approach to Aeroacoustics," *Sound-flow interactions*, Berlin, New York, pp 1-30.

Hirschfelder J.O., Curtiss C.F. and Bird R.B., 1964, *Molecular Theory of Gases and Liquids*, Wiley.

Holberg O., 1987, "Computational Aspects of the Choice of Operator and Sampling Interval for Numerical Differentiation in Large-Scale Simulation of Wave Phenomena," *Geophysics Prospect*, **35**, 629.

Howe M.S., 1999, "On the Scattering of Sound by a Rectilinear Vortex", *Journal of Sound and Vibration*, **227**(5), 1003-1017.

Howe M.S., 2002, "Lectures on the Theory of Vortex-Sound," *Sound-flow interactions*, Berlin, New York, pp 31-111.

Hu F.Q., 1996, "On Absorbing Boundary Conditionws for Linearized Euler Equations by a Perfectly Matched Layer," *Journal of Computational Physics*, **129**, 201-219.

Hu F.Q., 2001, "A Stable, Perfectly Matched Layer for Linearized Euler Equations in Unsplit Physical Variables," *Journal of Computational Physics*, **173**, 455-480.

Hu, F.Q., Hussaini, M.Y. and Manthey, J.L., 1996, "Low-Dissipation and Low-Dispersion Runge-Kutta Schemes for Computational Acoustics," *Journal of Computational Physics*, **124**, pp. 177-191.

Huteau, F., Lee, T. and Mateescu, D., 2000, "Flow Past a 2-D Backward-facing Step with an Oscillating Wall," *Journal of Fluids and Structures*, **14**, 691-696.

Kang H.-K., Tsutahara M., Ro K.-D. and Lee Y.-H., 2002, "Numerical Simulation of Shock Wave Propagation using the Finite Difference Lattice Boltzmann Method," *KSME International Journal*, **16**, No. 10, 1327-1335.

Kang H. –K., Ro K. –D., Tsutahara M. and Lee Y. –H., 2003, “Numerical Prediction of Acoustic Sounds Occurring by the Flow around a Circular Cylinder,” *KSME International Journal*, **17**, No. 8, 1219–1225.

Kim J.W. and Lee D.J., 2000, “Generalized Characteristic Boundary Conditions for Computational Aeroacoustics,” *AIAA Journal*, **38**, No. 11, pp. 2040-2049.

Krishnamurty, K., 1956, *Sound Radiation from Surface Cutouts in High Speed Flow*, Ph.D thesis, California Institute of Technology.

Ladd A.J.C., 1993, “Short-time Motion of Colloidal Particles: Numerical Simulation via a Fluctuating Lattice-Boltzmann Equation,” *Physical Review Letter*, **70**, 1339-1342.

Ladd A.J.C., 1997, “Sedimentation of Homogeneous Suspensions of Non-Brownian Spheres,” *Physical Fluids*, **9**, 491-499.

Lallemand P. and Luo L.–S., 2003, “Theory of the Lattice Boltzmann Method: Acoustic and Thermal Properties in Two and Three Dimensions,” *Physical Review E*, **68**, Paper No. 036706.

Larsson J., Davidson L., Olsson M. and Eriksson L.-E., 2004, “Aeroacoustic Investigation of an Open Cavity at Low Mach Number,” *AIAA Journal*, **42**, No. 12, 2462-2473.

Lele S.K., 1992, “Compact finite difference schemes with spectral-like resolution”, *Journal of Computational Physics*, **103**, 16–42.

Leung R.C.K. and So R.M.C, 2001, “Noise Generation of Blade-Vortex Resonance,” *Journal of Sound and Vibration*, 245, No. 2, 217-237.

Leung R.C.K., Li X.M. and So R.M.C., 2006, “Comparative Study of Non-Reflecting Boundary Condition for One-Step Numerical Simulation of Duct Aero-Acoustics,” *AIAA Journal*, Vol. **46**, No. 3, 664-667.

Lighthill M.J., 1952, “On Sound Generated Aerodynamically I. General theory”, *Proceedings of the Royal Society of London. Series A, Mathematical and Physical Sciences*, **211**, No. 1107, Mar. 20, 564-587.

Lilley G.M, 1974, “On the Noise from Jets”, *Noise Mechanisms*, AGARD-CP-131, pp. 13.1-13.12.

Lund F., 2002, “Sound-Vortex Interaction in Infinite Media,” *Sound-Flow Interactions*, Berlin, New York: Springer.

Michael C.S., Dani O., 2003, “Invasion Percolation of Single Component, Multiphase Fluids with Lattice Boltzmann Models,” *Physica B*, **338**, 298-303.

Morfey, C. L., 2000, *Dictionary of Acoustics*, Redwood Books Ltd, Trowbridge, UK.

Palmer B.J. and Rector D.R., 2000, “Lattice Boltzmann Algorithm for Simulating Thermal Flow in Compressible Fluids,” *Journal of Computational Physics*, 161, 1-20.

Pierce A.D., 1989, *Acoustics: An Introduction to its Physical Principles and Applications*, Woodbury, NY, Acoustical Society of America.

Premnath K.N. and Abraham J., 2004, “Discrete Lattice BGK Boltzmann Equation Computations of Transient Incompressible Turbulent Jets,” *International Journal of Modern Physics C*, **15**, No. 5, 699-719.

Poinsot, T.J. and Lele, S.K., 1992, “Boundary Conditions for Direct Simulations of Compressible Viscous Flows,” *Journal of Computational Physics*, **101**, 104–129.

Powell, A., 1964, “Theory of Vortex sound”, *Journal of the Acoustical Society of America*, 36, 177-195.

Qian Y.H., d’Humières, D. and Lallemand P., 1992, “Lattice BGK Models for Navier-Stokes Equation,” *Europhysics Letters*, **17**, 479–484.

Ricot D., Maillard V. and Bailly C., 2002, “Numerical Simulation of Unsteady Cavity Flow using Lattice Boltzmann Method,” *AIAA Paper* No. 2002-2532.

Roe P.L., 1986, “Characteristic-Based Schemes for the Euler Equations,” *Annual Review of Fluid Mechanics*, **18**, 337–365.

Rowley C.W. and Colonius T., 2000, “Discretely Nonreflecting Boundary Conditions fro Linear hyperbolice Systems,” *Journal of Computational Physics*, **157**, 500-538.

Rowley, C. W., Colonius, T., and Murray, R. M., 2000, “Pod Based Models of Self-Sustained Oscillations in the Flow Past an Open Cavity,” AIAA paper 2000-1969.

Rudy D.H. and Strikwerda J.C., 1980, “A Nonreflecting Outflow Boundary Condition for Subsonic Navier-Stokes Calculations,” *Journal of Computational Physics*, **36**, 55-70.

Succi S., 2001, The Lattice Boltzmann Equation for Fluid Dynamics and Beyond, Oxford University Press, 2001.

Sun C., 1998, “Lattice-Boltzmann Models for High Speed Flow,” *Physical Review E*, **58**, No. 6, 7283–7287.

Ta’asan S. and Nark D.M., 1995, “An Absorbing Buffer Zone Technique for Acoustic Wave Propagation,” *AIAA paper*, 95-0146.

Tam C.K.W. and Webb J.C., 1993, “Dispersion-Relation-Preserving Finite Difference Schemes for Computational Acoustics,” *Journal of computational Physics*, **107**, 262-281.

Tam C.K.W., 1995, “Computational Aeroacoustics: Issues and Methods,” *AIAA Journal*, **33**, No. 10, 1788-1796.

Tam C.K.W., Auriault L. and Cambuli F., 1998, “Perfectly Matched Layer as an Absorbing Boundary Condition for the Linearized Euler Equations in Open and Ducted Domains,” *Journal of Computational Physics*, **144**, 213-234.

Thompson K.W., 1987, "Time Dependent Boundary Conditions for Hyperbolic Systems," *Journal of Computational Physics*, **68**, 1-24.

Tsutahara M., Kataoka T., Takada N., Kang H.K. and Kurita M., 2002, "Simulations of Compressible Flows by Using the Lattice Boltzmann and the Finite Difference Lattice Boltzmann Methods," *Computational Fluid Dynamics Journal*, **11**, No. 1, 486-493.

Turkel E. and Yefet A., 1998, "Absorbing PML Boundary Layers for Wave-Like Equations," *Applied Numerical Mathematics*, **27**, 533-557.

Visbal M. and Gaitonde D.V., 2001, "Very High-order Spatially Implicit Schemes for Computational Acoustics on Curvilinear Meshes", *Journal of Computational Acoustics*, **9**, No. 4, 1259-1286.

Wang M. and Moin P., 2000, "Computation of Trailing-Edge Flow and Noise Using Large-Eddy Simulation," *AIAA Journal*, **38**, No. 12, 2201-2209.

Wells V.L. and Renaut R.A., 1997, "Computing Aerodynamically Generated Noise," *Annual Review of Fluid Mechanics*, **29**, 161-199.

White, F. M., 1991, *Viscous Fluid Flow*, New York, McGraw-Hill.

Williams J.E.F. and Hawkings D.L., 1969, "Sound Generation by Turbulence and Surfaces in Arbitrary Motion", *Philosophical Transactions of the Royal Society of London, Series A, Mathematical and Physical Sciences*, **264**, No. 1151, May 8, 321-342.

Wolf-Gladrow D.A., 2000, *Lattice-Gas Cellular Automata and Lattice Boltzmann Models. An Introduction*, Springer Verlag.

Yee H.C., Beam R.M. and Warming R.F., 1982, "Boundary Approximations for Implicit Schemes for One-Dimensional Inviscid Equations of Gasdynamics," *AIAA Journal*, **20**, No. 9, 1203-1211.